UNIVERSITÀ DEGLI STUDI ROMA TRE

Dipartimento di Matematica e Fisica
Doctoral program in Physics – XXXIV cycle

A dissertation submitted in partial fulfillment of
the requirements for the degree of
Doctor of Philosophy in Physics

Virtual QCD corrections via a transverse momentum expansion for gluon-initiated ZH and ZZ production

Author
Marco Vitti

Supervisor
Prof. Giuseppe Degrassi

January 2022

Se la verità è soltanto un passo verso la verità,
il valore della scienza consisterà piuttosto nel camminare
che nel fermarsi ad un termine provvisoriamente raggiunto.
— Federigo Enriques

Abstract

The study of the properties of the Higgs boson at the LHC is closely related to the study of gluon-initiated processes, which in turn requires the calculation of precise theoretical predictions in the SM. In this thesis we compute the virtual NLO corrections in QCD to the processes $gg \to ZH$ and $gg \to ZZ$, with a focus on the contribution from loops of top quarks. The two-loop box diagrams involving massive internal lines are approximated analytically using an expansion of the amplitude in terms of a small transverse momentum of the final-state particles. This method allows to obtain a reliable approximation of the virtual corrections for partonic center-of-mass energies lower than ~ 700 GeV. Furthermore, in the case of $gg \to ZH$ we show how this limit can be overcome by merging our results with those obtained from a complementary approach used in the literature, which is based on the expansion of the amplitude in the limit of high energies. When the results of both expansions are improved using Padé approximants, their combination provides analytical results that are accurate over the whole phase space.

Contents

Chapter 1

Introduction

In the never-ending journey towards the comprehension of the fundamental laws of Nature, the discovery of the Higgs boson at the Large Hadron Collider (LHC) has marked a turning point. The observation by the ATLAS and CMS experiments of the scalar resonance with a mass around 125 GeV [1, 2] has been a crucial confirmation of the Standard Model (SM) [3–6] of particle physics. Notably, the observation established the mechanism of spontaneous Electro-Weak Symmetry Breaking (EWSB) [7–12] as the theoretical tool for understanding the origin of the masses of the SM particles. The *Higgs sector* of the SM consists of one scalar field acquiring a nonzero vacuum expectation value (vev) which spontaneously breaks the $SU(2) \times U(1)$ EW symmetry. The interactions of the Higgs field with the weak gauge bosons and with the fermions can account for their masses in a way that is consistent with the fundamental principle of gauge symmetry. Furthermore, the scalar potential for the Higgs field includes trilinear and quadrilinear self-interactions. The measurement of the Higgs mass from the LHC experiments, together with the knowledge of the vev from the muon decay, allows to make unambiguous predictions in the SM.

The Higgs Boson at the LHC After the first observation of the Higgs boson in 2012, the study of its properties has become one of the primary tasks of the LHC program. The SM predicts that the cross sections for Higgs production processes and the Higgs decay rates are sensitive to the couplings of the boson to the other known particles. Therefore, a precise determination of these processes allows to characterize the Higgs and to assess whether it really behaves as the SM dictates. Testing the properties of the Higgs boson to high precision is important also to unveil potential signals of physics beyond the SM. Indeed, according to the lack of direct evidence for new physics in collider experiments, deviations from the SM predictions are expected to be observed as subtle effects. These signals could be precious hints to interpret phenomena that currently are not understood within the SM, such as dark matter, neutrino masses or the asymmetry between matter and antimatter in the Universe.

Currently, the Higgs sector of the SM has not been fully explored from an experimental point of view. In fact, while it is not clear whether the trilinear Higgs self-coupling will be measured at the LHC, the quadrilinear self-coupling is considered to be out of reach. Furthermore, a precise determination of the Higgs couplings with the lightest fermions is a very ambitious task. These challenges will be addressed by the future generation of particle colliders (see e.g. [13]).

On the other hand, if we consider what we do know about the Higgs from experiments, the improvement reached in the determination of many of its properties is remarkable. The

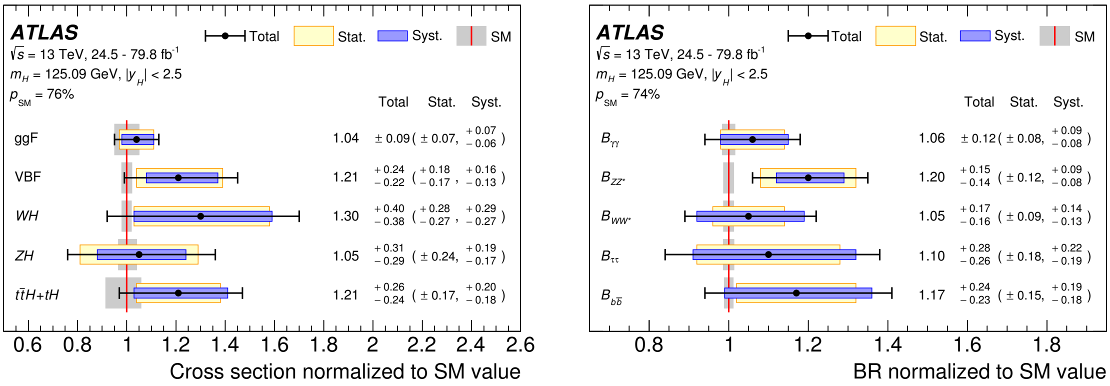

(a) (b)

Figure 1.1: ATLAS measurements of (a) the cross sections for the main Higgs production channels and of (b) the branching ratios for the main Higgs decay modes, normalized to the respective SM predictions. The black error bars, blue boxes and yellow boxes show the total, systematic, and statistical uncertainties in the measurements, respectively. The gray bands indicate the theory uncertainties in the predictions. The cross section measurements assume SM branching ratios and vice versa. Taken from [17].

Higgs mass is now measured with a permille accuracy [14] and its spin and parity are well understood [15]. The progress in the experimental efforts to determine the properties of the Higgs boson within the last ten years can be also appreciated from fig. 1.1. Figures 1.1(a) and 1.1(b) show respectively the measurements of the main production and decay modes of the Higgs boson at the LHC, normalized to their SM predictions. In basically every channel the deviations from theory expectations are at the level of 20% or below, and the total uncertainties are in the range of 10 to 30%, demonstrating a full compatibility with the SM predictions.

The situation in fig. 1.1 is expected to improve significantly with the forthcoming Run3 and especially with the High-Luminosity phase of the LHC. In particular, the most conservative estimates for the High-Luminosity phase [16] indicate that a reduction of the total uncertainties down to $\sim 5\%$ for all the channels shown in fig. 1.1 will be achieved. This level of precision will allow for a more stringent test of the SM.

In order to match the anticipated progress on experimental measurements, an adequate improvement on the theory side is mandatory. All the sources of theoretical uncertainties related to the predictions for Higgs processes at the LHC must be addressed to allow for a meaningful comparison with the experimental results. The present thesis aims to provide a contribution to this challenging task.

Theoretical Predictions for Collider Observables The possibility of calculating predictions for processes at hadron colliders must not be taken for granted, as it rests on three fundamental principles: the validity of the parton model, the property of factorization in hadronic cross sections [18] and the asymptotic freedom of Quantum Chromodynamics (QCD) [19, 20].

The parton model allows to interpret high-energy collisions between hadrons in terms of the *hard* scattering of their fundamental constituents, namely quarks and gluons. The idea behind factorization in hadron collisions is that the long-distance effects due to low-energy QCD and the short-distance effects related to the hard scattering of the partons can be treated independently, to a very good degree of approximation. Considering a case relevant for this thesis, if we denote the cross section for a given hadronic process in proton collisions as σ, the latter can be written as (see e.g. [21])

$$\sigma = \sum_{ij} \int dx_1 dx_2 \; f_i(x_1, \mu_F) f_j(x_2, \mu_F) \; \hat{\sigma}_{ij}(x_1, x_2, Q, \mu_F) + \mathcal{O}\left(\Lambda_{QCD}/Q\right) \tag{1.1}$$

where the cross section for a specific partonic process initiated by the partons i and j is defined as $\hat{\sigma}_{ij}$ and it is convoluted in eq.(1.1) with the parton density functions (PDF) f_i, f_j, associated to the probabilities that the partons i and j carry respectively a fraction x_1 and x_2 of the momenta of the incoming protons. The energy scale Q in eq.(1.1) is related to the characteristic energy of the partonic process, while $\Lambda_{\text{QCD}} \ll Q$ is the typical scale of nonperturbative QCD, with $\Lambda_{\text{QCD}} \sim 1$ GeV. The arbitrary factorization scale μ_F separates the long-distance and short-distance QCD effects. The former are encoded in the universal PDFs, the latter in the partonic cross section $\hat{\sigma}_{ij}$. Since asymptotic freedom of QCD implies that the strong coupling α_S is smaller than 1 when $Q \gg \Lambda_{\text{QCD}}$, we can obtain reliable predictions for the partonic cross section using perturbative Quantum Field Theory. In particular, we can express the partonic cross section as a perturbative series[1]

$$\hat{\sigma}_{ij}(\mu_F, \mu_R) = \alpha_S^k(\mu_R) \sum_{m=0}^{n} \hat{\sigma}_{ij}^{(m)}(\mu_F, \mu_R) \alpha_S^m(\mu_R) \tag{1.2}$$

where k is the leading power in α_S, and the dependence of the strong coupling and of the series coefficients $\hat{\sigma}_{ij}^{(m)}$ on the renormalization scale μ_R has been made explicit. The $\hat{\sigma}_{ij}^{(m)}$ are computed with the technique of Feynman diagrams: usually (although not in the case of this thesis) the leading-order (LO) coefficient $\hat{\sigma}_{ij}^{(0)}$ is associated to tree-level diagrams, whereas in order to evaluate higher-order effects one must compute loop diagrams as well as diagrams with additional particles in the final state.

When the perturbative series is computed up to a certain order, eqs.(1.1, 1.2) can be combined to obtain a fixed-order prediction for the hadronic cross section. However, as one is forced to truncate the series in eq.(1.2), the ignorance on the higher-order contributions constitutes an important systematic uncertainty[2]. The theoretical uncertainties associated to a fixed-order computation are conventionally estimated by studying how the result is affected by the variation of μ_F and μ_R within a certain range, typically centered around the hard scale Q. Nevertheless, this procedure is not guaranteed to be reliable, and the only way to genuinely estimate the size of the missing higher-order coefficients in eq.(1.2) is to actually compute them. The focus of this thesis will be on the calculation of higher-order terms using multi-loop calculations, namely we will consider the perturbative corrections obtained by increasing the number of loops in the Feynman diagrams, at the same time keeping the number of particles in the final state fixed w.r.t. the LO contribution.

[1]For completeness, QCD corrections are not the only higher-order effects that need to be computed in predictions for hadronic colliders, as also EW corrections are important [22]. However, the latter will not be considered in this thesis.

[2]Other relevant sources of theoretical uncertainties, which won't be discussed in this thesis, are: the uncertainties on the input parameters in the predictions; the uncertainties on the determination of the PDFs and on the modeling of the hadronization taking place after the partonic process; the effects of large logarithms which may spoil the convergence of the series in eq.(1.2).

Multi-Loop Calculations The details of a given multi-loop calculation may vary significantly depending on the process, but the typical structure of the problem involves a few common stages which we list below:

1. Identification of the Feynman diagrams relevant to the amplitude for a specific perturbative order
2. General study of the Lorentz structure of the amplitude, with the aim of decomposing the latter as a linear combination of projectors multiplying scalar form factors. The form factors contain scalar loop integrals
3. Study of the scalar loop integrals in the form factor and decomposition of the latter as a linear combination of a subset of simpler integrals, known as *master integrals*
4. Evaluation of the master integrals

The first of the above stages has been efficiently automated in computer programs, which are an indispensable tool to deal with the complexity of modern problems. The second stage can be addressed with some generality [23, 24]. The decomposition in terms of master integrals can be carried out using several methods; the use of recurrence relations known as *integration-by-parts* (IBP) *relations* [25, 26] is one of the most common approaches (although not always the most efficient) and in this thesis we will use the algorithmic implementation of the IBP decomposition. Finally, the evaluation of the master integrals is a very nontrivial problem. Notably, the number of energy scales occurring in the integrals, like the partonic kinematical variables and the masses of the particles involved, is a major limiting factor in their analytical evaluation.

In this thesis, we will discuss the case of two-loop diagrams for $2 \to 2$ processes with *massive* internal lines. In particular, we will concentrate on loops of top quarks, which play a special role in Higgs-related processes due to the fact that the strength of the Higgs couplings to the fermions is proportional to their mass. Also, top-quark loops pose a technical challenge: in the special case of two-loop box diagrams, the associated integrals cannot be computed in exact top-mass dependence using the analytical methods currently available, due to the high number of energy scales involved. An exact evaluation has been achieved with the use of numerical methods, of which an important example is sector decomposition [27]. However, this strategy has the drawback of being particularly demanding in terms of computing resources and time, and not very flexible w.r.t. a change of the input parameters.

Analytical Approximations Although the availability of exact results is an important accomplishment, the need to implement theoretical predictions in fast and flexible Monte Carlo codes, used in the direct comparison with experimental measurements, has motivated a parallel effort to study analytical approximations, based on the analysis of the kinematical limits of the loop integrals. In particular, one can assume certain hierarchies among the various scales in the integrals and expand the latter according to those hierarchies. The expanded integrals will depend on fewer scales than the original ones, and they can be calculated analytically. The drawback of this strategy is that the results are typically limited in their validity to the kinematical range where the approximations are legitimate. Thus, one trades the possibility of obtaining analytical results with the restriction to specific regions of the phase space. Among the various approaches discussed in the literature, we list here the ones that will be mentioned throughout the thesis:

- Assuming the top mass m_t to be the largest scale in the problem, one can expand the integrals in the infinite top mass limit ($m_t \to \infty$) (see.g. [28, 29]) A refinement of this approach is the *large mass expansion* (LME), in which m_t is again associated to the largest scale but it is considered to be finite. The integrals are then expanded in ratios of all the other kinematical scales to m_t (e.g. [30–32])

- In the *high-energy* (HE) *expansion*, the partonic kinematical variables (e.g. the Mandelstam variables $\hat{s}$ and $\hat{t}$) are associated to the largest scale, and the external and internal masses are taken to be small in comparison. Additional hierarchies for the external and internal masses are usually considered (e.g. [33–36])

- In the *small-mass expansion* the integrals are expanded in the limit of small external masses compared to the other scales in the integrals (e.g. [37, 38])

The p_T Expansion A different kind of analytical approximations has been proposed for the first time in ref. [39], in the study of double-Higgs production in gluon fusion. This approach is based on the asymptotic expansion of the loop integrals in terms of a forward kinematics, corresponding to the limit in which the transverse momentum of the final state particles, p_T, is small compared to the $\hat{s}$ variable and to the scale set by the mass of the top quark.

The main goal of this thesis is to show that this novel approach, that will be denoted as *p_T expansion* in the following, can be used to compute the effects of top-quark loops to other $2 \to 2$ processes relevant for Higgs physics at the LHC. In particular, we study gluon-initiated processes, for which higher-order QCD corrections are very important, as they are expected to be comparable in magnitude w.r.t. the LO terms (see e.g. [40]).

In chap. 2 we apply the p_T expansion to study the virtual QCD corrections to gluon-initiated ZH production, $gg \to ZH$, at next-to-leading order (NLO). Loops of top quarks play a dominant role in this process, and they contribute substantially to the theoretical uncertainties in the current prediction for associated ZH production at the LHC. In chap. 2 we provide an introduction to the p_T expansion method, as well as to the technique of IBP reduction, in the context of its application to $gg \to ZH$, and we present the results published in ref. [41].

In chap. 3 we consider gluon-initiated Z pair production, $gg \to ZZ$, at NLO in QCD. This process is important for Higgs physics due to the interplay of its two sub-amplitudes, one related to resonant Higgs production via $gg \to H \to ZZ$ and one related to the non-resonant contribution $gg \to ZZ$. Loops of light quarks as well as the top are relevant in this process. However, at the two-loop level only the contribution from the former is known exactly in analytical form, and we use the p_T expansion to obtain an approximation of the two-loop diagrams involving top quarks.

Like the other analytical approximations, the p_T expansion cannot be trusted in all the regions of the phase space. In particular, the method becomes unreliable in regions where p_T is comparable or larger w.r.t. the scale set by the top mass. However in chap. 4 we discuss the possibility of merging the results of the p_T expansion with those available from a different approximation, namely the HE expansion. The latter can provide reliable predictions in a region of the phase space that is complementary in relation to the p_T expansion, and in chap. 4 we show how the two approaches can be combined to obtain a prediction over the full phase space. Finally, in chap. 5 we present our conclusions and we discuss the future implications of our findings.

Chapter 2

Virtual QCD Corrections to $gg \to ZH$

2.1 Introduction

Associated production $pp \to VH$ (also known as Higgs-Strahlung) is a process in which a single Higgs boson is emitted together with a weak vector boson ($V = Z, W$) in a proton-proton collision. It is one of the main Higgs production processes investigated at the LHC. For a SM Higgs with a mass around 125 GeV, the cross sections for the WH and ZH case are $\mathcal{O}(\text{pb})$ (see fig. 2.1(a)). Despite being not as frequent as other production mechanisms like gluon fusion or vector boson fusion, associated production provides a unique way to study the decay of the Higgs to a pair of bottom quarks, which is challenging to observe at an hadronic collider due to the many sources of QCD background. In the Higgs-Strahlung case, the leptonic decays of the weak bosons can be exploited to tag the associated Higgs, thus enhancing the signal-to-background ratio in experimental searches. The latter strategy and the employment of jet-substructure techniques [42] were crucial elements for the first observation of the $H \to b\bar{b}$ decay, made by ATLAS and CMS [43, 44] in 2018, establishing associated production as the most sensitive category to $H \to b\bar{b}$ [45].

The SM cross sections for both the WH and ZH channels receive the leading and next-to-leading contributions from a partonic process where a pair of quarks first produces a virtual weak boson V^* which then decays to the VH final state. The QCD corrections for this quark-initiated process (a.k.a. the Drell-Yan-like contribution) are known through next-to-next-to-next-to-leading order (N^{3}LO) [46–49], while the EW corrections are known through NLO [50, 51]. However, in the specific case of associated ZH production one has to consider an additional contribution coming from the partonic process $gg \to ZH$, which arises for the first time as a NNLO QCD correction to the total $pp \to ZH$ cross section. Despite being an $\mathcal{O}(\alpha_S^2)$ correction, the contribution from this subprocess to the hadronic cross section is non-negligible because of the large gluon luminosity at the LHC. It has been shown that the relevance of $gg \to ZH$ is even more enhanced in the boosted kinematic regime, to the point of being comparable to the quark-initiated contribution near the $t\bar{t}$ threshold [52].

Since currently only the LO prediction for $gg \to ZH$ is included in the Monte Carlo codes [53], the factorization- and renormalization-scale uncertainties related to the gluon-induced process can be as large as 25%. They affect significantly the theoretical uncertainty on the total $pp \to ZH$ cross section, compared to $pp \to WH$ (see fig. 2.1(b)). The knowledge of the NLO corrections to $gg \to ZH$ would reduce the scale uncertainties, facilitating precision

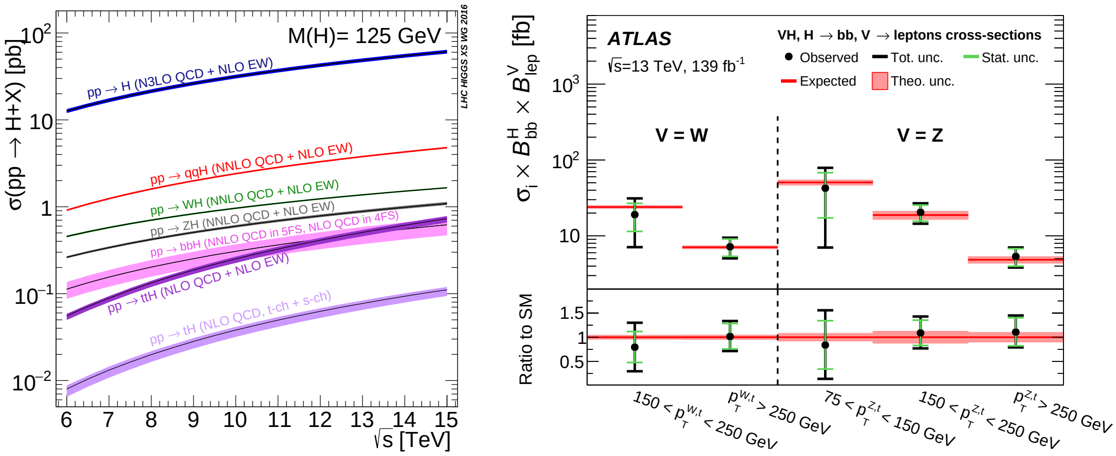

(a) (b)

Figure 2.1: (a) Theoretical SM predictions for the main Higgs production modes at the LHC, as a function of the c.o.m. energy $\sqrt{s}$, for $m_H = 125$ GeV. The bands around the solid lines represent the theoretical uncertainties, while the label over each line refers to the highest orders known in perturbative calculations (taken from [56]). (b) Cross section for the combination of associated production $pp \to VH$ followed by $H \to b\bar{b}$ and $V \to$leptons, measured by ATLAS. The theoretical uncertainties (pink bands) for the ZH case are larger than for WH due to the additional $gg \to ZH$ contribution (taken from [45]).

studies in the next runs of the LHC. The $gg \to ZH$ contribution is relevant also for New Physics (NP) studies, since it is sensitive to both sign and magnitude of the top Yukawa coupling, dipole operators [54] and can receive additional contributions from new particles [55]. An improved knowledge of the SM prediction for the gluon-induced contribution is therefore very important both for precision measurements[1] of ZH production and for testing NP in this channel. The present chapter is devoted to the study of this partonic process.

The LO contribution to the $gg \to ZH$ amplitude, given by one-loop diagrams, was computed exactly in refs. [57,58]. The virtual NLO QCD corrections are not fully known analytically, as they include two-loop integrals which depend on up to five scales. Specifically, the exact analytical results for the two-loop box diagrams are unavailable with the current multi-loop computational techniques. A first calculation of the NLO terms was obtained in ref. [28] using an asymptotic expansion in the limit $m_t \to \infty$ and $m_b = 0$, and pointed to corrections of about 100% with respect to the LO contribution. Soft gluon resummation has been performed in ref. [59] including next-to-leading logarithmic terms, and the result has been matched to the fixed NLO computation of ref. [28]. Finite top-quark-mass effects to $gg \to ZH$ have been investigated in ref. [60] using a combination of the LME and Padé approximants. In addition, a data-driven method to extract the non-Drell-Yan part of $pp \to ZH$, which is dominated by the gluon-induced contribution, has been proposed in ref. [61], exploiting the known relation between WH and ZH associated production when only the Drell-Yan component of the two processes is considered. A qualitative study focusing on patterns in the differential distribution has been conducted in ref. [62], where $2 \to 2$ and $2 \to 3$ LO matrix elements were merged and matched to improve the description of the kinematics. Recently,

[1]See also the *Precision Wish List* included in ref. [53].

a new analytic computation of the NLO virtual contribution based on the HE expansion of the amplitude, supported by Padé approximants, and on an improved LME, has been carried out [35]. The results are in agreement with an exact numerical study [63], in the energy regions where the expansions are legitimate. An improvement on the analytic calculation is still desirable, since the LME and the HE expansion do not cover well the invariant-mass region $350\,\text{GeV} \lesssim M_{ZH} \lesssim 750\,\text{GeV}$. It should be remarked that this region provides a significant contribution to the hadronic cross section at the LHC, about 68%.

In this chapter, based on the findings of ref. [41], we present an analytic calculation of the virtual NLO QCD corrections to the $gg \to ZH$ process. The two-loop box diagrams, and the associated multi-scale integrals, are computed in terms of a forward kinematics via an expansion in the Z (or Higgs) transverse momentum, p_T, following the approach of ref. [39]. The other contributions to the virtual corrections are computed exactly. This approximation allows to cover the region $M_{ZH} \lesssim 750\,\text{GeV}$, which contributes about 98% to the hadronic cross section at LHC energies. We point out here that after the publication of ref. [41] a new study of the NLO corrections to $gg \to ZH$ was presented [38]. The latter is based on the approximation of the two-loop box integrals using the small-mass expansion. In theory, this approach allows to cover nearly the totality of the phase space, and we are going to comment about this in chap. 5.

This chapter has the following structure: in the next section we introduce our notation for the $gg \to ZH$ amplitude and for the kinematics. In sec. 2.3 we give the details of our decomposition of the amplitude in terms of Lorentz projectors multiplying scalar form factors. In sec. 2.4 we present the method for expanding the amplitude in terms of the Z transverse momentum. Sec. 2.5 is an introduction to the method of integration-by-parts reduction used to reduce the number of scalar integrals to be computed, and to simplify their structure. In Sec. 2.6 we outline the steps in which our calculation has been organized at a given perturbative order using a `Mathematica` code. Sec. 2.7 is devoted to a discussion of the expected validity range of the approximation of the amplitude via the p_T expansion, by comparing the latter with the known exact result for the LO cross section. In sec. 2.8 we discuss the ingredients of the calculation of the NLO amplitude and present our results. Although both triangle and box topologies contribute to the LO and NLO amplitudes, the examples and figures presented in sec. 2.7 and 2.8 will be almost exclusively focused on the box diagrams, as the main original contribution from this thesis is the approximation of the related integrals using the p_T expansion.

2.2 General Properties of the $gg \to ZH$ Amplitude

We begin the study of gluon-initiated ZH production by analyzing the general properties of the process, at the same time introducing our notation. We will define the Feynman amplitude for the process $g_a^\mu(p_1) g_b^\nu(p_2) \to Z^\rho(p_3) H(p_4)$ as

$$\mathcal{A} = i\sqrt{2}\frac{m_Z G_F \alpha_S(\mu_R)}{\pi} \delta_{ab} \epsilon_\mu^a(p_1) \epsilon_\nu^b(p_2) \epsilon_\rho^*(p_3) \hat{\mathcal{A}}^{\mu\nu\rho}(p_1, p_2, p_3), \tag{2.1}$$

where G_F is the Fermi constant, $\alpha_S(\mu_R)$ is the strong coupling constant defined at a renormalization scale μ_R, and $\epsilon_\mu^a(p_1)\epsilon_\nu^b(p_2)$ and$\epsilon_\rho(p_3)$ are the polarization vectors of the gluons and the Z boson, respectively. The tensor $\hat{\mathcal{A}}^{\mu\nu\rho}$ encodes all the information about the Lorentz structure of the amplitude, and it will be discussed in detail in the next section.

In our calculation we will consider on-shell external particles, therefore

$$p_1^2 = p_2^2 = 0 \qquad p_3^2 = m_Z^2 \qquad p_4^2 = m_H^2, \tag{2.2}$$

where m_Z and m_H are the masses of the Z and Higgs bosons, respectively. In the following we will assume all external momenta to be incoming, so that four momentum conservation is expressed as

$$p_1 + p_2 + p_3 + p_4 = 0. \tag{2.3}$$

According to the latter convention, the partonic Mandelstam variables are defined as

$$\hat{s} = (p_1 + p_2)^2 \qquad \hat{t} = (p_1 + p_3)^2 \qquad \hat{u} = (p_2 + p_3)^2 \tag{2.4}$$

and they satisfy

$$\hat{s} + \hat{t} + \hat{u} = m_Z^2 + m_H^2. \tag{2.5}$$

We furthermore assume that the external vector bosons are transversely polarized with respect to their relative four-momentum

$$p_1 \cdot \epsilon^a(p_1) = 0 \qquad p_2 \cdot \epsilon^b(p_2) = 0 \qquad p_3 \cdot \epsilon(p_3) = 0 \tag{2.6}$$

and that gauge symmetry is respected

$$p_{1\mu} \hat{\mathcal{A}}^{\mu\nu\rho}(p_1, p_2, p_3) = 0 \qquad p_{2\nu} \hat{\mathcal{A}}^{\mu\nu\rho}(p_1, p_2, p_3) = 0. \tag{2.7}$$

The amplitude defined in eq.(2.1) must respect Bose symmetry for the interchange of the initial gluons $\{\mu \leftrightarrow \nu, p_1 \leftrightarrow p_2, a \leftrightarrow b\}$. In particular, this implies the following symmetry relation for the for the Lorentz tensor $\hat{\mathcal{A}}^{\mu\nu\rho}$

$$\hat{\mathcal{A}}^{\mu\nu\rho}(p_1, p_2, p_3) = \hat{\mathcal{A}}^{\nu\mu\rho}(p_2, p_1, p_3). \tag{2.8}$$

Another important feature of the $gg \to ZH$ amplitude concerns the nature of the couplings of the external particles. While the gluons have only a vector coupling with the quarks running in the loop, the Z boson has a vector and an axial coupling, which we denote as

$$-i \frac{g}{\cos\theta_W} \gamma^\mu (g_V - g_A \gamma^5), \tag{2.9}$$

where g is the weak coupling, θ_W is the Weinberg angle and

$$g_V = I_q - 2Q_q \sin^2\theta_W \qquad g_A = I_q, \tag{2.10}$$

with Q_q the electric charge and I_q the third component of the weak isospin for a given quark q. By considering the separate contribution from g_V and from g_A we can decompose the amplitude into a vector and and axial part. However, the diagrams proportional to g_V will contain fermion loops with three vector couplings, and Furry's theorem predicts that these diagrams must vanish, as a consequence of charge-conjugation invariance. Then, only the part of the amplitude proportional to g_A will give a nonzero contribution. This observation has three implications: first, only Lorentz structures involving a Levi-Civita tensor $\epsilon^{\mu\nu\rho\sigma}$ will be relevant for the Lorentz tensor $\hat{\mathcal{A}}^{\mu\nu\rho}$ defined in eq.(2.1); secondly, the amplitude will be proportional to the third component of the weak isospin $I_q = \pm 1/2$, leading the sum of the contributions from up- and down-type quarks in a given family to vanish in the case of equal masses. In this thesis we will assume all quarks but the top to be massless, so the only nonzero contribution to the amplitude will come from the third generation of quarks; finally, as in this thesis we will use Dimensional Regularization to regularize the loop integrals, the presence of the γ_5 matrix in the axial coupling requires a delicate treatment, and this problem will be discussed in sec. 2.8.4.

The kinematical quantity relevant for our expansion is the transverse momentum p_T of the Z boson. Assuming that the initial gluons travel along the z-axis, we define p_T as

$$p_T = \sqrt{p_{3x}^2 + p_{3y}^2}. \tag{2.11}$$

We can highlight this quantity by taking the four-momentum p_3^μ and isolating the part $r_\perp^\mu$ that is orthogonal to both p_1^μ and p_2^μ

$$p_3^\mu = a\; p_1^\mu + b\; p_2^\mu + r_\perp^\mu, \tag{2.12}$$

where a and b are generic coefficients and $r_\perp = (0, p_{3x}, p_{3y}, 0)$, in such a way that

$$r_\perp \cdot p_1 = 0 = r_\perp \cdot p_2. \tag{2.13}$$

We have then that $r_\perp^\mu$ is a space-like quantity, and we can obtain p_T via the relation

$$r_\perp^2 = -p_T^2. \tag{2.14}$$

By contracting eq.(2.12) with p_1^μ and p_2^μ it is easy to find the actual values of the a and b coefficients, and we get

$$p_3^\mu = \frac{\hat{t} - m_Z^2}{\hat{s}}\; p_1^\mu + \frac{\hat{u} - m_Z^2}{\hat{s}}\; p_2^\mu + r_\perp^\mu, \tag{2.15}$$

from which p_T can be expressed as

$$p_T^2 = \frac{\hat{t}\hat{u} - m_Z^2 m_H^2}{\hat{s}}. \tag{2.16}$$

The relation between the $\hat{t}$ variable and p_T can be obtained by solving the system of eq.(2.5) and eq.(2.16) with respect to $\hat{t}$ and $\hat{u}$. The two sets of solutions are related to the *forward* and *backward* kinematical regimes. In particular, in the forward regime we have

$$\begin{aligned} \hat{t} &= -\frac{1}{2}\left(\hat{s} - m_Z^2 - m_H^2 - \sqrt{\lambda(\hat{s}, m_Z^2, m_H^2) - 4\hat{s}p_T^2}\right) \\ \hat{u} &= -\frac{1}{2}\left(\hat{s} - m_Z^2 - m_H^2 + \sqrt{\lambda(\hat{s}, m_Z^2, m_H^2) - 4\hat{s}p_T^2}\right), \end{aligned} \tag{2.17}$$

where $\lambda(a,b,c) = a^2 + b^2 + c^2 - 2ab - 2ac - 2bc$ is the Källén function, while the backward regime is defined by eq.(2.17) but with $\hat{t}$ and $\hat{u}$ interchanged.

2.3 Construction of the Projectors

The Lorentz tensor $\hat{\mathcal{A}}^{\mu\nu\rho}$ introduced in eq.(2.1) can be decomposed along a basis of orthonormal projectors $\mathcal{P}_i^{\mu\nu\rho}$ which multiply scalar form factors $\mathcal{A}_i$

$$\hat{\mathcal{A}}^{\mu\nu\rho}(p_1, p_2, p_3) = \sum_i \mathcal{P}_i^{\mu\nu\rho} \mathcal{A}_i(\hat{s}, \hat{t}, \hat{u}, m_t, m_Z, m_H) \tag{2.18}$$

The form factors depend only on scalar quantities, namely the mass m_t of the top quark (i.e. the only massive quark running in the loops), the masses of the external particles and the partonic Mandelstam variables. In this section we are going to describe the method employed to obtain the Lorentz projectors, while the rest of the chapter will be devoted to the study of the form factors.

The projectors in eq.(2.18) are *orthonormal* in the sense that the squared modulus of the amplitude, summed over the external polarizations, is simply given by the sum over the squared moduli of the form factors

$$\begin{aligned}\sum_{\text{pol}} |\mathcal{A}|^2 &\propto \sum_{\text{pol}} \epsilon_\mu(p_1)\epsilon^*_\alpha(p_1)\ \epsilon_\nu(p_2)\epsilon^*_\beta(p_2)\ \epsilon^*_\rho(p_3)\epsilon_\gamma(p_3)\ \hat{\mathcal{A}}^{\mu\nu\rho}\hat{\mathcal{A}}^{\alpha\beta\gamma *} \\ &\propto (-g_{\mu\alpha})\,(-g_{\nu\beta})\left(-g_{\rho\gamma} + \frac{p_{3\rho}p_{3\gamma}}{m_Z^2}\right)\sum_i \mathcal{P}_i^{\mu\nu\rho}\mathcal{A}_i \sum_j \mathcal{P}_j^{\alpha\beta\gamma *}\mathcal{A}_j^* \\ &\propto \sum_i |\mathcal{A}_i|^2 \,.\end{aligned} \tag{2.19}$$

and the above relation is obtained by requiring that

$$(-g_{\mu\alpha})\,(-g_{\nu\beta})\left(-g_{\rho\gamma} + \frac{p_{3\rho}p_{3\gamma}}{m_Z^2}\right)\mathcal{P}_i^{\mu\nu\rho}\mathcal{P}_j^{\alpha\beta\gamma *} = \delta_{ij}. \tag{2.20}$$

The form of the Lorentz projectors $\mathcal{P}_i^{\mu\nu\rho}$ is dictated not only by gauge symmetry (eq.(2.7)) but also by the requirement for the form factors to be either symmetric or antisymmetric with respect to the interchange $\{\mu \leftrightarrow \nu, p_1 \leftrightarrow p_2\}$. The reason behind this requirement is related to the possibility of using only the forward component of the amplitude to compute the complete result, as will be discussed in sec. 2.4. To fulfill this requirement, the method for constructing the projectors is the following

1. Identify all the relevant Lorentz structures, i.e. those which give a nonzero contribution to the amplitude

2. Assemble the single Lorentz structures into linear combinations that are separately (anti)symmetric with respect to the interchange $\{\mu \leftrightarrow \nu, p_1 \leftrightarrow p_2\}$

3. Orthogonalize the linear combinations as in eq.(2.20) using the standard Gram-Schmidt procedure

The relevant Lorentz structures $S_i^{\mu\nu\rho}$ compatible with eqs.(2.6, 2.7) were identified in ref. [57]:

$$\begin{aligned}
&S_1^{\mu\nu\rho} = \epsilon^{\mu\nu\rho p_1} && S_2^{\mu\nu\rho} = \epsilon^{\mu\nu\rho p_2} && S_3^{\mu\nu\rho} = \epsilon^{\mu\nu\rho p_3} && S_4^{\mu\nu\rho} = g^{\mu\nu}\epsilon^{\rho p_1 p_2 p_3} && (2.21)\\
&S_5^{\mu\nu\rho} = p_1^\nu\epsilon^{\mu\rho p_1 p_2} && S_6^{\mu\nu\rho} = p_2^\mu\epsilon^{\nu\rho p_1 p_2} && S_7^{\mu\nu\rho} = p_1^\nu\epsilon^{\mu\rho p_2 p_3} && S_8^{\mu\nu\rho} = p_2^\mu\epsilon^{\nu\rho p_1 p_3} && (2.22)\\
&S_9^{\mu\nu\rho} = p_3^\nu\epsilon^{\mu\rho p_1 p_2} && S_{10}^{\mu\nu\rho} = p_3^\mu\epsilon^{\nu\rho p_1 p_2} && S_{11}^{\mu\nu\rho} = p_3^\nu\epsilon^{\mu\rho p_1 p_3} && S_{12}^{\mu\nu\rho} = p_3^\mu\epsilon^{\nu\rho p_2 p_3} && (2.23)\\
& && S_{13}^{\mu\nu\rho} = p_2^\mu\epsilon^{\nu\rho p_2 p_3} && S_{14}^{\mu\nu\rho} = p_1^\nu\epsilon^{\mu\rho p_1 p_3}\,, && && (2.24)
\end{aligned}$$

where the contraction of a Levi-Civita tensor with a generic four-momentum $\epsilon^{\mu\nu\rho\alpha}q_\alpha$ is written as $\epsilon^{\mu\nu\rho q}$. Apart from $S_4^{\mu\nu\rho}$ the above structures are not separately (anti)symmetric under

$\{\mu \leftrightarrow \nu, p_1 \leftrightarrow p_2\}$, but can be used to form (anti)symmetric linear combinations. In particular, we employed the following combinations

$$\begin{aligned}
\mathcal{T}_1^{\pm} &= \frac{t'}{s'}\left(s' S_2^{\mu\nu\rho} - S_6^{\mu\nu\rho}\right) \pm \frac{u'}{s'}\left(S_5^{\mu\nu\rho} - s' S_1^{\mu\nu\rho}\right), \\
\mathcal{T}_2^{\pm} &= \left(\frac{t'}{s'} S_6^{\mu\nu\rho} - S_{10}^{\mu\nu\rho}\right) \pm \left(S_9^{\mu\nu\rho} - \frac{u'}{s'} S_5^{\mu\nu\rho}\right), \\
\mathcal{T}_3^{\pm} &= \frac{s'}{u'}\left(S_{12}^{\mu\nu\rho} - \frac{t'}{s'} S_{13}^{\mu\nu\rho}\right) \pm \frac{s'}{t'}\left(S_{11}^{\mu\nu\rho} - \frac{u'}{s'} S_{14}^{\mu\nu\rho}\right), \\
\mathcal{T}_4 &= s' S_3^{\mu\nu\rho} + S_4^{\mu\nu\rho} + S_7^{\mu\nu\rho} - S_8^{\mu\nu\rho},
\end{aligned} \tag{2.25}$$

where the $\mathcal{T}_i^+$ are symmetric while the $\mathcal{T}_i^-$ and $\mathcal{T}_4$ are antisymmetric under $\{\mu \leftrightarrow \nu, p_1 \leftrightarrow p_2\}$. In eq.(2.25) we used the reduced Mandelstam variables defined in eq.(2.26). The Gram-Schmidt orthogonalization of the combinations in eq.(2.25) produces the projectors $\mathcal{P}_i^{\mu\nu\rho}$ which we present in app. A.1.

2.4 Description of the p_T Expansion

In this section we are going to present in detail the procedure for the expansion of the amplitude in terms of a small p_T. First, we show how to implement the p_T expansion as an expansion of the amplitude in the limit of a forward (or backward) kinematics, and we indicate the parameters that are relevant for such an expansion. Then we discuss how, with a suitable choice of the projectors, the results obtained only in the forward limit allow to have an approximation for the complete partonic cross section, so that an expansion in the backward limit can be avoided, simplifying the calculation.

Expansion in the forward limit For the discussion of the p_T expansion, it is convenient to introduce the reduced Mandelstam variables

$$s' = p_1 \cdot p_2 = \frac{\hat{s}}{2} \qquad t' = p_1 \cdot p_3 = \frac{\hat{t} - m_Z^2}{2} \qquad u' = p_2 \cdot p_3 = \frac{\hat{u} - m_Z^2}{2} \tag{2.26}$$

satisfying the analogous of eq.(2.5, 2.16)

$$s' + t' + u' = \frac{m_H^2 - m_Z^2}{2} = \Delta_m \tag{2.27}$$

$$p_T^2 = \frac{2t'u'}{s'} - m_Z^2. \tag{2.28}$$

Using the new variables, the four-momentum p_3^μ in eq.(2.15) is expressed as

$$\begin{aligned}
p_3^\mu &= \frac{u'}{s'} p_1^\mu + \frac{t'}{s'} p_2^\mu + r_\perp^\mu \\
&= -p_1^\mu - \frac{t'}{s'}(p_1 - p_2)^\mu + \frac{\Delta_m}{s'} p_1^\mu + r_\perp^\mu
\end{aligned} \tag{2.29}$$

and one can identify the *forward* limit with the relation $p_3^\mu \simeq -p_1^\mu$. By looking at eq.(2.29), this limit can be associated to the following conditions:

$$\frac{\Delta_m}{s'} \simeq 0 \qquad t' \simeq 0 \qquad r_\perp^\mu \simeq 0^\mu. \tag{2.30}$$

Now we notice that in the forward regime t' can be written as the analogous of eq.(2.17)

$$t' = -\frac{s'}{2}\left\{1 - \frac{\Delta_m}{s'} - \sqrt{\left(1 - \frac{\Delta_m}{s'}\right)^2 - 2\frac{p_T^2 + m_Z^2}{s'}}\right\} \tag{2.31}$$

and the condition $t' \simeq 0$ in (2.30) can be translated to the situation in which p_T^2, m_Z^2 and Δ_m are small compared to s' (notice also that in this case one has $u' \simeq -s'$). Then, the conditions in (2.30) are equivalent to

$$\frac{p_T^2}{s'} \simeq 0 \qquad \frac{m_Z^2}{s'} \simeq 0 \qquad \frac{\Delta_m}{s'} \simeq 0 \qquad r_\perp^\mu \simeq 0^\mu, \tag{2.32}$$

which we identify as the small parameters to be considered for the implementation of the p_T expansion. Then, we define the hierarchy of energy scales on which our approximation is based, and we will associate s' to a *large* scale and p_T^2, m_Z^2, Δ_m and $r_\perp^\mu$ to a *small* scale. It is easy to see that in the backward limit, $p_3^\mu \simeq -p_2^\mu$, the same considerations as above can be made, but with the roles of t' and u' exchanged.

In a practical calculation, one must replace p_3^μ everywhere in one of the form factors $\mathcal{A}_i$ defined in eq.(2.18), using eq.(2.29); then one must use eq.(2.31) in order to express $\mathcal{A}_i$ only in terms of the quantities in (2.32). At this point, the form factor can be Taylor-expanded in the small parameters. To perform the expansion, one can rewrite the parameters as multiplying a common scale x, then Taylor-expand the form factor near $x = 0$, and set $x = 1$ after the expansion. It is important to note here that since the parameters in (2.32) have different dimensionalities, they must scale with x in a consistent manner. In particular, the following scaling relations must be respected

$$r_\perp^\mu \to x\, r_\perp^\mu \qquad \{p_T^2, m_Z^2, \Delta_m\} \to x^2\{p_T^2, m_Z^2, \Delta_m\}. \tag{2.33}$$

We remark that in our approach one must treat p_T and $r_\perp^\mu$ as independent quantities when performing the Taylor expansion. Indeed, although by definition the scalar loop integrals in the form factors will ultimately depend only on $r_\perp^2 = -p_T^2$, the Taylor expansion in our method is performed *before* the loop integration, at the integrand-level. In this case, one cannot avoid the presence of scalar products between $r_\perp^\mu$ and the loop momenta in the integrands; using the relations in eq.(2.33) allows to deal with this issue in a consistent manner.

The assumption of the hierarchy for the quantities in eq.(2.32) is justified in the forward (or backward) regime. However, when the expansion method discussed above is used, one is implicitly assuming an hierarchy also with respect to the mass of the particle(s) running in the loops: in our case, the top mass m_t. The latter must be associated to another large scale, comparable to s', within our approach.

In fact, the scale set by m_t is the one which poses the strictest limitation in the validity of the approximation. In sec. 2.7 we will show that the convergence of the p_T expansion is guaranteed only for values of the transverse momentum satisfying the condition

$$\frac{p_T^2}{4m_t^2} \lesssim 1. \tag{2.34}$$

We will discuss the origin of this limit in chap. 4, where we consider the complementarity of the p_T expansion in relation to the HE expansion. Here we make the general observation that the scale set by the mass of the lightest particle running in the loop is the scale that restricts the range of validity of the p_T expansion. For this reason, the latter is particularly useful in the approximation of diagrams where only heavy particles are involved.

To summarize our discussion, we have identified the large scales in our problem with s' and m_t, while the small scales are those in eq.(2.33).

A LO example As stated before in this thesis, the main point of performing the p_T expansion is to simplify the structure of the integrals in the amplitude by reducing the number of their scales, and here we discuss this point explicitly with an example. Let us consider the following class of scalar one-loop integrals associated to the box diagrams at LO

$$\int d^D q_1 \, \frac{(q_1^2)^{n_1}(q_1 \cdot p_1)^{n_2}(q_1 \cdot p_2)^{n_3}(q_1 \cdot p_3)^{n_4}}{(q_1^2 - m_t^2)[(q_1+p_2)^2 - m_t^2][(q_1 - p_1 - p_3)^2 - m_t^2][(q_1 - p_1)^2 - m_t^2]} \tag{2.35}$$

where q_1 is the loop momentum, D is the number of space-time dimensions in Dimensional Regularization and scalar products raised to integer $n_i \geq 0$ can appear in the integrand numerator. The integral (2.35) will depend on five scales, given by all the scalar quantities that can be formed with the external momenta and the masses in the propagators: $s', t', m_H^2, m_Z^2, m_t^2$ (notice that we traded u' with m_H^2 by means of eq.(2.27)). The part of the integrand which is modified by the p_T expansion is the one where p_3 appears, namely

$$\frac{(q_1 \cdot p_3)^{n_4}}{[(q_1 - p_1 - p_3)^2 - m_t^2]}. \tag{2.36}$$

After using eqs.(2.29) and (2.31), the Taylor expansion of (2.36) generates scalar products like $q_1 \cdot p_1$, $q_1 \cdot p_2$ and $q_1 \cdot r_\perp$. Furthermore, the expansion produces higher powers of the denominator, which in turn assumes the form $(q_1^2 - m_t^2)$ in the forward limit $p_3 \simeq -p_1$. Notably, the $r_\perp^\mu$ vector does not appear in the denominator anymore. As a consequence, after the p_T expansion the class of integrals in (2.35) is replaced by integrals of the following form

$$\int d^D q_1 \, \frac{(q_1^2)^{n_1}(q_1 \cdot p_1)^{n_2'}(q_1 \cdot p_2)^{n_3'}(q_1 \cdot r_\perp)^{n_4'}}{(q_1^2 - m_t^2)^{l_1}[(q_1+p_2)^2 - m_t^2][(q_1 - p_1)^2 - m_t^2]} \tag{2.37}$$

where n_2', n_3', n_4' are new non-negative integers and l_1 is a strictly positive integer. We observe that the scales upon which these new loop integrals depend are now $\hat{s}, p_T^2, m_t^2$. We have thus reduced the number of scales involved in the problem with respect to the original class of integrals (2.35). We will see, however, that the dependence on p_T^2 can be ultimately dropped, as integrals like the ones in (2.37) can be rewritten solely in terms of integrals where $n_4' = 0$ using the integration-by-parts relations that will be discussed in the next section. This possibility is related to the fact that $r_\perp^\mu$ appears only in the $q_1 \cdot r_\perp$ scalar product, and only in the numerator.

Using only the forward expansion So far we have discussed the implementation of the expansion in the limit $t' \simeq 0$, namely the forward expansion. In fact, the cross section for a $2 \to 2$ process can be written as a sum of a forward and backward contributions

$$\sigma \propto \int_{t_i'}^{t_f'} dt' |\mathcal{A}_i(t', u')|^2 = \int_{t_i'}^{t_m'} dt' |\mathcal{A}_i(t', u')|^2 + \int_{t_m'}^{t_f'} dt' |\mathcal{A}_i(t', u')|^2 \tag{2.38}$$

where the extrema of integration are defined as

$$t_i' = \frac{\hat{t}^- - m_Z^2}{2} \qquad t_f' = \frac{\hat{t}^+ - m_Z^2}{2}, \tag{2.39}$$

with

$$\hat{t}^{\pm} = \frac{1}{2}\left(-\hat{s} + m_H^2 + m_Z^2 \pm \sqrt{\lambda(\hat{s}, m_H^2, m_Z^2)}\right), \tag{2.40}$$

and t'_m corresponds to to the value of maximum transverse momentum, such that $t' = u' = (-s' + \Delta_m)/2$. In principle an expansion in $t' \simeq 0$ would give an approximation of the form factor only in the region $[t'_i, t'_m]$, whereas an expansion in the backward limit ($u' \simeq 0$) is needed in the complementary part of the integration domain, so that the approximation of the exact cross section by the p_T expansion is given by

$$\int_{t'_i}^{t'_f} dt' |\mathcal{A}_i(t', u')|^2 \simeq \int_{t'_i}^{t'_m} dt' |\mathcal{A}_i(t' \sim 0, u' \sim -s')|^2 + \int_{t'_m}^{t'_f} dt' |\mathcal{A}_i(t' \sim -s', u' \sim 0)|^2. \tag{2.41}$$

However, as noticed in ref. [39], if the form factor in eq.(2.41) is symmetric under the exchange $t' \leftrightarrow u'$ (which is just a proxy for Bose symmetry) then one can write $\mathcal{A}_i(-s', 0) = \mathcal{A}_i(0, -s')$ and eq.(2.41) becomes

$$\int_{t'_i}^{t'_f} dt' |\mathcal{A}_i(t', u')|^2 \simeq \int_{t'_i}^{t'_m} dt' |\mathcal{A}_i(0, -s')|^2 + \int_{t'_m}^{t'_f} dt' |\mathcal{A}_i(0, -s')|^2 = \int_{t'_i}^{t'_f} dt' |\mathcal{A}_i(0, -s')|^2, \tag{2.42}$$

meaning that the expansion in the forward limit is sufficient to obtain an approximation of the complete partonic cross section. In the case of $gg \to ZH$, using the projectors defined in the previous section, the form factors can be either symmetric or antisymmetric[2] under $t' \leftrightarrow u'$. For the symmetric form factors, one can then expand only in the forward limit and use eq.(2.42). When dealing with the antisymmetric form factors, one can extract an overall antisymmetric factor using

$$\mathcal{A}_i^{\text{antisym}}(t', u') = (t' - u') \frac{\mathcal{A}_i^{\text{antisym}}(t', u')}{(t' - u')} = (t' - u') \mathcal{A}_i^{\text{sym}}(t', u') \tag{2.43}$$

and perform the forward expansion only on the symmetric part, $\mathcal{A}_i^{\text{sym}}(t', u')$. We verified that this procedure allows to obtain a correct result for the complete partonic cross section. Therefore, if the amplitude is decomposed in terms of either symmetric or antisymmetric Lorentz projectors, one can avoid to perform the p_T expansion in the backward limit.

2.5 IBP Reduction and `LiteRed`

After the form factors are expanded as described in the previous section, we have shown that the structure of the original loop integrals becomes simplified. Still, the number of integrals to be computed is usually large. In fact, the Taylor expansion of the form factors causes a proliferation of scalar integrals with respect to the original, non-expanded, ones, so there is a trade-off between the simplification in the structure of the integrals and the number of integrals to be dealt with in the calculation. However, the scalar integrals resulting from the p_T expansion are not all independent[3], and one can use recurrence relations known as *integration-by-parts* (IBP) *relations* [25, 26], to express each integral in terms of a small

[2] The (anti)symmetry of the form factors is clearly inherited from the one of the projectors, in accordance to the overall Bose symmetry.

[3] For the sake of clarity, neither the original scalar integrals in the non-expanded form factors are all independent, and they too admit a decomposition in terms of MIs via an IBP reduction.

subset of so-called *master integrals* (MIs). The Laporta algorithm [64] is the first automatic implementation of the IBP reduction and it has been employed in many codes. The reduction of the scalar integrals in this thesis has been performed via the `Mathematica` package `LiteRed` [65, 66], which performs the reduction heuristically by searching for replacement rules that allow for a symbolic decomposition of all the scalar integrals in terms of MIs. In the following we are going to give a brief general description of the procedure, and we refer the interested reader to [65–67].

The fundamental objects that need to be considered for the IBP reduction are D-dimensional L-loop integrals of the following form

$$J(n_1, \dots, n_N) = \int d^D q_1 \cdots d^D q_L \; j(n_1, \dots, n_N) = \int \frac{d^D q_1 \cdots d^D q_L}{D_1^{n_1} \cdots D_N^{n_N}} \tag{2.44}$$

where the quantities D_i are allowed to be

- denominators from virtual particle propagators, which can be raised to any integer $n_i \in \mathbb{Z}$
- scalar products between loop momenta and external momenta; in particular we require that the scalar products in the definition (2.44) cannot be expressed as linear combinations of denominators; in this case the exponents n_i are assumed to be nonpositive integers and the corresponding D_i are called *irreducible numerators*

A set of linearly independent D_i which fall into the two categories above is called a *basis* of denominators. Once a basis is fixed, one can use the property of scalar integrals in Dimensional Regularization

$$\int d^D q_1 \cdots d^D q_L \frac{\partial k_i^\mu}{\partial q_j^\mu} j(n_1, \dots, n_N) = 0, \tag{2.45}$$

where the k_i^μ can be both loop or external momenta, to find relations connecting integrands with different n_i. Specifically, after differentiation the scalar products $q_i \cdot k_j$ can be expressed as linear combinations of the D_i, so that the integrals resulting from eq.(2.45) can still be written as in the form of (2.44), but with different n_i. Then, the IBP relations assume the following general structure

$$\sum_i \alpha_i \; J(n_1 + c_{i,1}, \dots, n_N + c_{i,N}) = 0 \tag{2.46}$$

where $c_{i,k} \in \mathbb{Z}$ and α_i are coefficients depending on the scalar products between external momenta, on the masses in the propagators and on the number of space-time dimensions D. The relations in (2.46) can be used to express recursively a generic integral $J(n_1, \dots, n_N)$ as a linear combination of a minimal set of linearly independent integrals, which then constitute a basis of MIs. As a consequence of the recursive decomposition, usually the MIs will depend on n_i that are small integers: 0, 1 or 2. We also point out that it is always possible to find a basis with a finite number of MIs [68], although the basis is generally not unique.

In the case of the form factors for $gg \to ZH$, the scalar integrals obtained after the p_T expansion are not already in the form of eq.(2.44), as reducible scalar products usually appear in the numerators. Also, the denominators in some classes of integrals constitute an overdetermined basis and they have to be manipulated further (we will show an explicit example in eq.(2.52)). After the study of the relevant topologies of the Feynman diagrams, a certain number of denominator bases has to be identified, so that the reducible scalar products can be expressed as linear combinations of denominators, while the irreducible numerators are left unchanged. Once every integral in a form factor is expressed as in eq.(2.44), the chosen bases are analyzed with `LiteRed`, leading to the identification of the MIs and to the generation of the symbolic rules that will be used for the IBP reduction. Furthermore, the `LiteRed` command `AnalyzeSectors` allows to restrict the search for the MIs to integrals where the irreducible numerators are raised to 0. This allows for an additional simplification of the integrals obtained after the p_T expansion: with reference to the class of integrals in the example (2.37), integrals having $n_4 = 0$ will depend only on the ratio of the two remaining scales, namely on s'/m_t^2.

As a result of the p_T expansion followed by the IBP reduction, the scalar form factors will be expressed as a power series in terms of p_T^2, m_Z^2 and Δ_m, potentially multiplied by an overall rational function $\mathcal{N}$ of the latter quantities,

$$\mathcal{A}_i = \mathcal{N}(p_T^2, m_Z^2, \Delta_m) \sum_{N=0}^{\infty} \sum_{i+j+k=N} c_{i,j,k} \, (p_T^2)^i (m_Z^2)^j (\Delta_m)^k, \tag{2.47}$$

where the $c_{i,j,k}$ are linear combinations of the MIs, whose coefficients are rational functions of $\hat{s}$ and m_t^2 only . For convenience, throughout this thesis we will refer to a given order in the Taylor expansion as the $\mathcal{O}(p_T^{2n})$ term, when we actually include all the terms that scale as $(x/y)^n$, with $x = p_T^2, m_Z^2, \Delta_m$ and $y = s', m_t^2$.

We point out that, conceptually, the p_T expansion and the IBP reduction are independent operations, and one could think of inverting the order of the two in the calculation. However, performing the p_T expansion at the level of Feynman diagrams, as described in the previous section, not only brings an important simplification in the structure of the MIs, but allows also to deal with fewer MIs, and generally the intermediate expressions related to the IBP reduction are less complicated with respect to the case in which the reduction is performed on the original diagrams.

2.6 The Code

The computation of the $gg \to ZH$ amplitude with the method described above has been semi-automatized within a `Mathematica` notebook, which was used to produce all the results presented in this chapter employing both public packages and private routines written from scratch. The most important steps of the calculation at LO and at NLO are listed in the following

1. The diagrams are generated using `FeynArts` [69]

2. The handling of the fermion traces and the color-algebra is performed using `FeynCalc` [70, 71]

3. The amplitude is contracted with the Lorentz projectors of app. A.1 using `FeynCalc` in order to isolate a single form factor

4. The form factor is Taylor expanded with private routines as described in sec. 2.4 and each order of the expansion is treated separately from this point on

5. The minimal number of integral families is identified manually, and these are converted in a set of denominator bases for `LiteRed`

6. The overdetermined bases of denominators are automatically found and decomposed in terms of the independent ones

7. Every integral is rewritten in `LiteRed` notation (eq.(2.44)) by replacing every reducible scalar product with a linear combination of denominators

8. The lists of symbolic rules for the IBP reduction are produced using `LiteRed`

9. The above rules are applied to the scalar integrals appearing in the form factor, so that the result is a linear combination of the MIs found by `LiteRed`

2.7 The LO Contribution to $gg \to ZH$

In this and in the following sections we are going to present the results of the application of the method described in sec. 2.4 and in sec. 2.5 and implemented in the code of sec. 2.6. We are interested in computing the virtual QCD corrections to the process at NLO, therefore we will express the form factors $\mathcal{A}_i$ introduced in eq.(2.18) as a perturbative series in the strong coupling, defined as

$$\mathcal{A}_i = \mathcal{A}_i^{(0)} + \frac{\alpha_S}{\pi}\mathcal{A}_i^{(1)} + \mathcal{O}\left(\alpha_S^2\right), \tag{2.48}$$

where $\mathcal{A}_i^{(0)}$ and $\mathcal{A}_i^{(1)}$ are the LO and NLO contributions.

In this section we give the main details of the calculation at LO. We used `FeynCalc` to reproduce the exact analytical results first obtained in ref. [57] and compared them to the results of the p_T expansion in order to assess the reliability of the latter. After the generation using `FeynArts` we find 6 one-loop diagrams[4] belonging to triangle and box topologies (see fig.2.2). It is then convenient to split the LO form factors in terms of the contributions of triangles and boxes

$$\mathcal{A}_i^{(0)} = \mathcal{A}_i^{(0,\triangle)} + \mathcal{A}_i^{(0,\square)}. \tag{2.49}$$

Among the triangle diagrams there are loops of top and bottom quarks that connect to the final-state particles via an $\hat{s}$-channel virtual Z boson (fig.2.2 (b)) and loops of top quarks producing an intermediate neutral Goldstone boson G^0 (fig.2.2 (a)). The box topologies are represented by loops of top quarks, an example of which is given in fig.2.2 (c). As the box diagrams feature a Yukawa coupling, the contribution from the bottom quarks is zero in the massless approximation.

As observed in ref. [28], the calculation of the triangle diagrams can be simplified by setting it in the Landau gauge. In this gauge, the diagrams with a virtual Z boson propagator vanish because they can be related to the production of a massive particle via two massless particles, which is forbidden by the Landau-Yang theorem [72, 73]. Considering that the triangle diagrams form a gauge-invariant set, it is then sufficient to compute the diagrams with a Goldstone in Landau gauge. We checked this explicitly by calculating $\mathcal{A}_i^{(0,\triangle)}$ both in Feynman and Landau gauge, finding indeed the same result. We notice that the observation in ref. [28] holds at every order in the perturbative series, and we will use it to simplify the calculation of the triangle diagrams also at NLO. Concerning the box topologies, we computed the diagrams in Feynman gauge. The exact analytical results at LO have been obtained using

[4] To be precise, the diagrams produced by `FeynArts` are 17: five of these are diagrams with a virtual $\hat{s}$-channel gluon and they vanish due to color-charge conservation; the remaining 12 diagrams can be grouped in couples of diagrams that differ only by the direction of the fermions running in the loops.

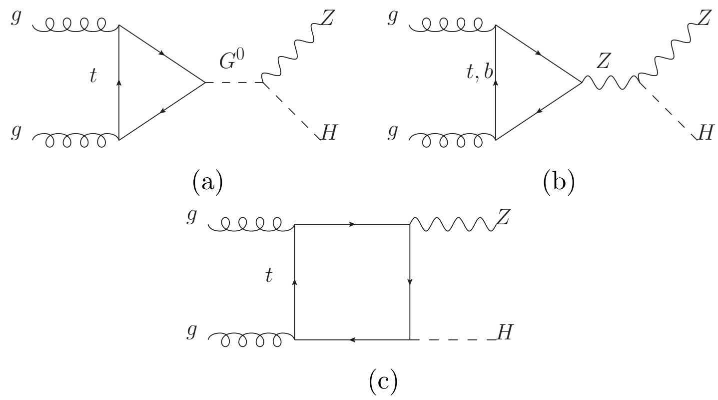

Figure 2.2: Representative Feynman diagrams contributing to the $gg \to ZH$ amplitude at LO. Triangle topologies with (a) a neutral Goldstone boson G^0 and (b) a Z boson in an $\hat{s}$-channel propagator are present together with (c) box diagrams.

the `FeynCalc` implementation of the Passarino-Veltman reduction algorithm [74], so that the final results can be expressed in terms of the known scalar functions, B_0, C_0 and D_0, which we evaluated numerically using `LoopTools` [75].

The loop integrals for both triangle and box diagrams at LO are generally UV-divergent, with the divergences showing up as $1/\varepsilon$ poles for $\varepsilon \to 0$ in Dimensional Regularization, assuming $D = 4 - 2\varepsilon$. However, due to the fact that there is no tree-level $ggZH$ vertex in the SM, the renormalizability of the theory implies that the LO result must be finite, so the UV divergences from the one-loop integrals cancel when considering the sum of all diagrams.[5].

2.7.1 p_T Expansion and IBP Reduction of the Box Integrals

In this subsection we are going to present the details of the calculation of the box form factors at LO using the p_T expansion. As stated in the introduction, we focus on the $\mathcal{A}_i^{(0,\Box)}$ because the key purpose of the p_T expansion is to provide an approximation of the two-loop box integrals[6] at NLO, and the main steps of the method can be illustrated at LO in a more concise way. After the amplitude generation with `FeynArts` and contraction with the projectors, we find that each form factor is written in terms of three classes of one-loop scalar integrals, each one associated to one of the three diagrams contributing to $\mathcal{A}_i^{(0,\Box)}$

$$
\begin{aligned}
\mathcal{I}_1 &= \int d^D q_1 \, \frac{(q_1^2)^{n_1}(q_1\cdot p_1)^{n_2}(q_1\cdot p_2)^{n_3}(q_1\cdot p_3)^{n_4}}{(q_1^2-m_t^2)[(q_1+p_2)^2-m_t^2][(q_1-p_1-p_3)^2-m_t^2][(q_1-p_1)^2-m_t^2]}\\
\mathcal{I}_2 &= \int d^D q_1 \, \frac{(q_1^2)^{n_1}(q_1\cdot p_1)^{n_2}(q_1\cdot p_2)^{n_3}(q_1\cdot p_3)^{n_4}}{(q_1^2-m_t^2)[(q_1+p_3)^2-m_t^2][(q_1+p_2+p_3)^2-m_t^2][(q_1-p_1)^2-m_t^2]}\\
\mathcal{I}_3 &= \int d^D q_1 \, \frac{(q_1^2)^{n_1}(q_1\cdot p_1)^{n_2}(q_1\cdot p_2)^{n_3}(q_1\cdot p_3)^{n_4}}{(q_1^2-m_t^2)[(q_1+p_2)^2-m_t^2][(q_1+p_2+p_3)^2-m_t^2][(q_1-p_1)^2-m_t^2]},
\end{aligned}
\tag{2.50}
$$

where the scalar products in the numerator can be raised to any integer $n_i \geq 0$. After substituting p_3 using the second line of eq.(2.29), the diagrams are expanded as discussed in sec. 2.4. The structure of the integrands in (2.50) is modified by the p_T expansion, and we

[5]In particular, the triangle and box contributions are separately UV and IR finite

[6]Exact analytical results will be obtained for the other classes of diagrams at NLO.

obtain the following new integrands

$$
\begin{aligned}
i_1(n_1,\dots,n_7) &= \frac{(q_1\cdot r_\perp)^{n_4}(q_1^2)^{n_5}(q_1\cdot p_1)^{n_6}(q_1\cdot p_2)^{n_7}}{(q_1^2-m_t^2)^{n_1}[(q_1+p_2)^2-m_t^2]^{n_2}[(q_1-p_1)^2-m_t^2]^{n_3}}\\
i_2(n_1,\dots,n_7) &= \frac{(q_1\cdot r_\perp)^{n_4}(q_1^2)^{n_5}(q_1\cdot p_1)^{n_6}(q_1\cdot p_2)^{n_7}}{(q_1^2-m_t^2)^{n_1}[(q_1-p_1)^2-m_t^2]^{n_2}[(q_1+p_2-p_1)^2-m_t^2]^{n_3}}\\
i_3(n_1,\dots,n_8) &= \frac{(q_1\cdot r_\perp)^{n_5}(q_1^2)^{n_6}(q_1\cdot p_1)^{n_7}(q_1\cdot p_2)^{n_8}}{(q_1^2-m_t^2)^{n_1}[(q_1+p_2)^2-m_t^2]^{n_2}[(q_1+p_2-p_1)^2-m_t^2]^{n_3}[(q_1-p_1)^2-m_t^2]^{n_4}}.
\end{aligned}
\tag{2.51}
$$

We now notice that, apart from the irreducible numerator $(q_1 \cdot r_\perp)$, all the other scalar products in the numerator of $i_1(n_1,\dots,n_7)$ and $i_2(n_1,\dots,n_7)$ can be expressed *unambiguously* as linear combinations of the denominators. This is not the case for $i_3(n_1,\dots,n_8)$. For example, $(q_1\cdot p_1)$ can be expressed in two ways:

$$
\begin{aligned}
q_1\cdot p_1 &= -\frac{1}{2}\{[(q_1-p_1)^2-m_t^2]-(q_1^2-m_t^2)\}\\
q_1\cdot p_1 &= -\frac{1}{2}\{[(q_1+p_2-p_1)^2-m_t^2]-[(q_1+p_2)^2-m_t^2]+2s'\}
\end{aligned}
$$

We conclude that the denominators in i_3 form an overdetermined basis. Notably, the integrands associated to i_3 can be written as a linear combination of those of i_1 and i_2. This can be understood by considering the special case $i_3(1,1,1,1,0,0,0,0)$ and noting that

$$
\begin{aligned}
&\frac{1}{(q_1^2-m_t^2)[(q_1+p_2)^2-m_t^2][(q_1+p_2-p_1)^2-m_t^2][(q_1-p_1)^2-m_t^2]} =\\
&-\frac{1}{2s'}\frac{1}{(q_1^2-m_t^2)[(q_1+p_2)^2-m_t^2][(q_1-p_1)^2-m_t^2]}\\
&+\frac{1}{2s'}\frac{1}{(q_1^2-m_t^2)[(q_1-p_1)^2-m_t^2][(q_1+p_2-p_1)^2-m_t^2]}\\
&+\frac{1}{2s'}\frac{1}{(q_1^2-m_t^2)[(q_1+p_2)^2-m_t^2][(q_1+p_2-p_1)^2-m_t^2]}\\
&-\frac{1}{2s'}\frac{1}{[(q_1-p_1)^2-m_t^2][(q_1+p_2)^2-m_t^2][(q_1+p_2-p_1)^2-m_t^2]}
\end{aligned}
\tag{2.52}
$$

where the first two terms on the r.h.s. correspond (apart from a $1/(2s')$ factor) to $i_1(1,1,1,0,0,0,0)$ and $i_2(1,1,1,0,0,0,0)$, and the second two can be mapped onto $i_2(1,1,1,0,0,0,0)$ and $i_1(1,1,1,0,0,0,0)$ with the rerouting $q_1 \to q_1+p_1-p_2$ followed by $q_1\to -q_1$. In the more general case in which any of the powers of the denominators of $i_3(n_1,\dots,n_8)$ is greater than 1, eq.(2.52) can be used iteratively to obtain a decomposition in terms of the same products of denominators appearing in the r.h.s. of eq.(2.52), with some denominators raised to powers greater than 1.

We have thus proved that, at LO, all the integrals appearing in each order of the p_T expansion can be associated to one of two families of integrals. We also showed that each family can be written as in eq.(2.44), and according to that definition we can then fix the following bases of denominators

	$J_1(n_1,\ldots,n_4)$	$J_2(n_1,\ldots,n_4)$
D_1	$q_1^2 - m_t^2$	$q_1^2 - m_t^2$
D_2	$(q_1+p_2)^2 - m_t^2$	$(q_1-p_1)^2 - m_t^2$
D_3	$(q_1-p_1)^2 - m_t^2$	$(q_1+p_2-p_1)^2 - m_t^2$
D_4	$q_1 \cdot r_\perp$	$q_1 \cdot r_\perp$

where we notice that the scalar product $q_1 \cdot r_\perp$ is an irreducible numerator. At this point, `LiteRed` can perform the search of the MIs, finding the following set of 5 MIs:

$$\{J_1(0,1,0,0);\ J_1(0,1,1,0);\ J_1(1,1,1,0);\ J_2(1,0,1,0);\ J_2(1,1,1,0)\}\,. \tag{2.53}$$

Note that all the MIs have $n_4 = 0$, meaning that they do not involve the irreducible numerator, and therefore do not depend on p_T. Also, the MIs have at most three denominators, and this is another simplification compared to the original structure of the box integrals (cfr. eq.(2.50)). Finally, the scalar integrals can be translated into the well-known Passarino-Veltman [74] scalar functions[7]. We find, modulo a rerouting and a normalization factor,

$$\begin{aligned}
J_1(0,1,0,0) &\to A_0(m_t^2)\\
J_1(1,0,1,0) &\to B_0(\hat{s}, m_t^2, m_t^2)\\
J_1(1,1,1,0) &\to C_0(0,0,\hat{s}, m_t^2, m_t^2, m_t^2)\\
J_2(0,1,1,0) &\to B_0(-\hat{s}, m_t^2, m_t^2)\\
J_2(1,1,1,0) &\to C_0(0,0,-\hat{s}, m_t^2, m_t^2, m_t^2)
\end{aligned} \tag{2.54}$$

and the scalar functions are defined as

$$A_0(m^2) = \frac{1}{i\pi^2}\int \frac{d^Dq}{\mu^{D-4}}\frac{1}{q^2-m^2} \tag{2.55}$$

$$B_0(p^2, m_1^2, m_2^2) = \frac{1}{i\pi^2}\int \frac{d^Dq}{\mu^{D-4}}\frac{1}{(q^2-m_1^2)((q+p)^2-m_2^2)} \tag{2.56}$$

$$C_0(p_a^2, p_b^2, (p_a+p_b)^2, m_1^2, m_2^2, m_3^2) = \frac{1}{i\pi^2}\int \frac{d^Dq}{\mu^{D-4}}\frac{1}{[q^2-m_1^2][(q+p_a)^2-m_2^2][(q-p_b)^2-m_3^2]} \tag{2.57}$$

with μ the 't Hooft mass.

2.7.2 LO Form Factors

In this subsection we present some of the results obtained with the method described in the previous sections. While still looking only at the contribution from box diagrams, we focus our discussion on the form factor $\mathcal{A}_1^{(0,\Box)}$, which is associated to largest contribution to the partonic cross section, as can be seen from fig. A.1 in app. A.4. An explicit analytical result for $\mathcal{A}_1^{(0,\Box)}$ up to and including $\mathcal{O}(p_T^4)$ terms is given as an example in app. A.2 , while here we discuss how accurately the exact result for $\mathcal{A}_1^{(0,\Box)}$ can be reproduced by the analytical

[7] In fact, the Passarino-Veltman reduction method can be considered as a special form of IBP reduction, in which the scalar functions constitute a universal basis of MIs that can be used for any one-loop problem.

approximation provided by the p_T expansion. The numerical results presented here were produced using the following input parameters

$$
\begin{aligned}
&m_Z = 91.1876 \text{ GeV}, \quad m_H = 125.1 \text{ GeV}, \quad m_t = 173.21 \text{ GeV}, \\
&m_b = 0, \quad G_F = 1.6637 \text{ GeV}^{-2}, \quad \alpha_S(\mu_R) = \alpha_S(m_Z) = 0.118.
\end{aligned}
$$

In fig. 2.3 and 2.4 we show the comparison of the first three orders of the p_T expansion to the exact results for $\mathcal{A}_1^{(0,\square)}$. The results are plotted for a fixed value of $\sqrt{\hat{s}}$, and the x-axis shows the range of p_T values allowed by the kinematics, specifically by the relation

$$
p_T \le \sqrt{\frac{\lambda(\hat{s}, m_Z^2, m_H^2)}{4\hat{s}}}. \tag{2.58}
$$

First, fig. 2.3(a,b) and fig. 2.4(a) show the situation for $\sqrt{\hat{s}} = 400$ GeV, a value of the c.o.m. energy that is slightly above the threshold for the production of a pair of top quarks $2m_t \simeq 350$ GeV. One can see that the convergence of the p_T expansion is fast for both the real and the imaginary[8] part of the form factor, and three orders are enough to reach a remarkable agreement with the exact result for every value of p_T, as can be noticed from the bottom part of fig. 2.4(a), showing the ratio of the various orders of the expansion to the exact result. For higher values of $\sqrt{\hat{s}}$, the p_T expansion still approximates the exact prediction very well, but only for a restricted range of p_T values, corresponding to $p_T \lesssim 300$ GeV. This range is the same independently from the value of $\sqrt{\hat{s}}$ (compare fig. 2.3 (c,d) - 2.4(b) and fig. 2.3 (e,f) - 2.4(c)); instead, for higher values of the transverse momentum, the accuracy of the p_T expansion decreases rapidly. The same behavior can be observed for all the other form factors in the plots shown in app. A.4, see fig. A.2. The limit of validity of the p_T expansion noticed above can be related to the hierarchy assumed in eq.(2.34) between the transverse momentum and the top quark mass, and a possible way to circumvent this limitation will be discussed in chap. 4.

2.7.3 LO Cross Section

We now discuss to what extent the approximation that we obtained for the p_T-expanded form factors affects the prediction for the partonic cross section at LO. Recalling the definition in eq.(2.1) and the property of the projectors in eq.(2.19), the squared modulus of the amplitude, summed over the external polarizations and averaged over the initial ones and over color, is given by

$$
< \sum_{\text{pol}} |\mathcal{A}|^2 > = \frac{1}{2}\frac{1}{2}\frac{1}{8}\frac{1}{8} 8 \frac{2 m_Z^2 G_F^2 \alpha_S^2(\mu_R)}{\pi^2} \sum_i |\mathcal{A}_i|^2 . \tag{2.59}
$$

The differential cross section $d\hat{\sigma}/d\hat{t}$ for a $2 \to 2$ process is

$$
\frac{d\hat{\sigma}}{d\hat{t}} = \frac{1}{16\pi \hat{s}^2} < \sum_{\text{pol}} |\mathcal{A}|^2 >, \tag{2.60}
$$

from which we obtain the LO partonic cross section $\hat{\sigma}^{(0)}$

$$
\hat{\sigma}^{(0)}(\hat{s}) = \frac{m_Z^2 G_F^2 \alpha_S^2(\mu_R)}{256\ \hat{s}^2 \pi^3} \int_{\hat{t}^-}^{\hat{t}^+} d\hat{t} \sum_i \left| \mathcal{A}_i^{(0)} \right|^2 \tag{2.61}
$$

[8]For values of $\sqrt{\hat{s}}$ below the top-pair production threshold the imaginary part is zero.

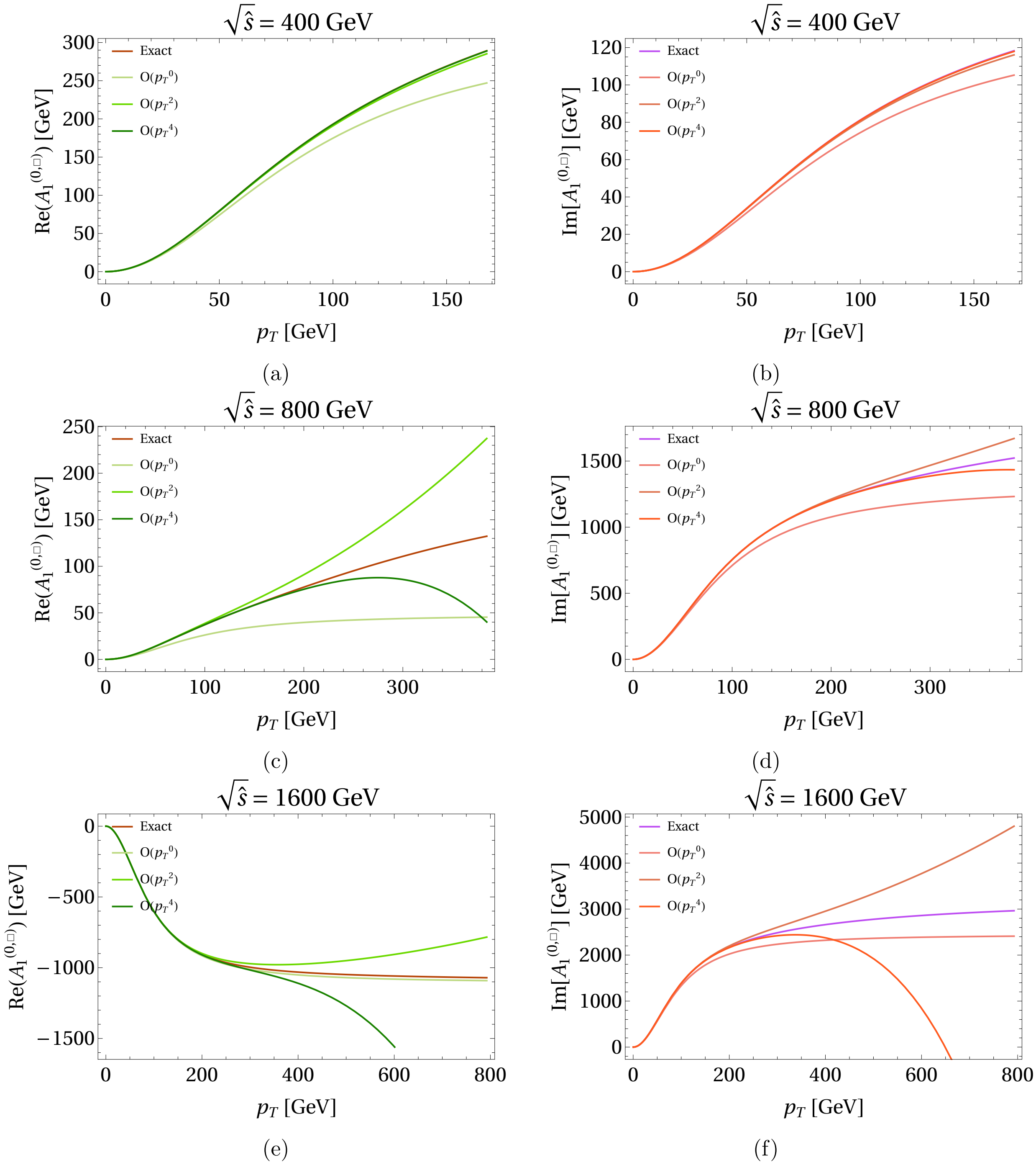

Figure 2.3: Results for the $\mathcal{A}_1^{(0,\square)}$ form factor. The first row shows the real (left) and imaginary (right) parts plotted against p_T for a c.o.m. energy of $\sqrt{\hat{s}} = 400$ GeV. The first three orders in the p_T expansion (green lines - left; red lines - right) are shown together with the exact result (brown line - left; purple line - right). The second and third rows show the same quantities as the first row, for higher values of $\sqrt{\hat{s}}$.

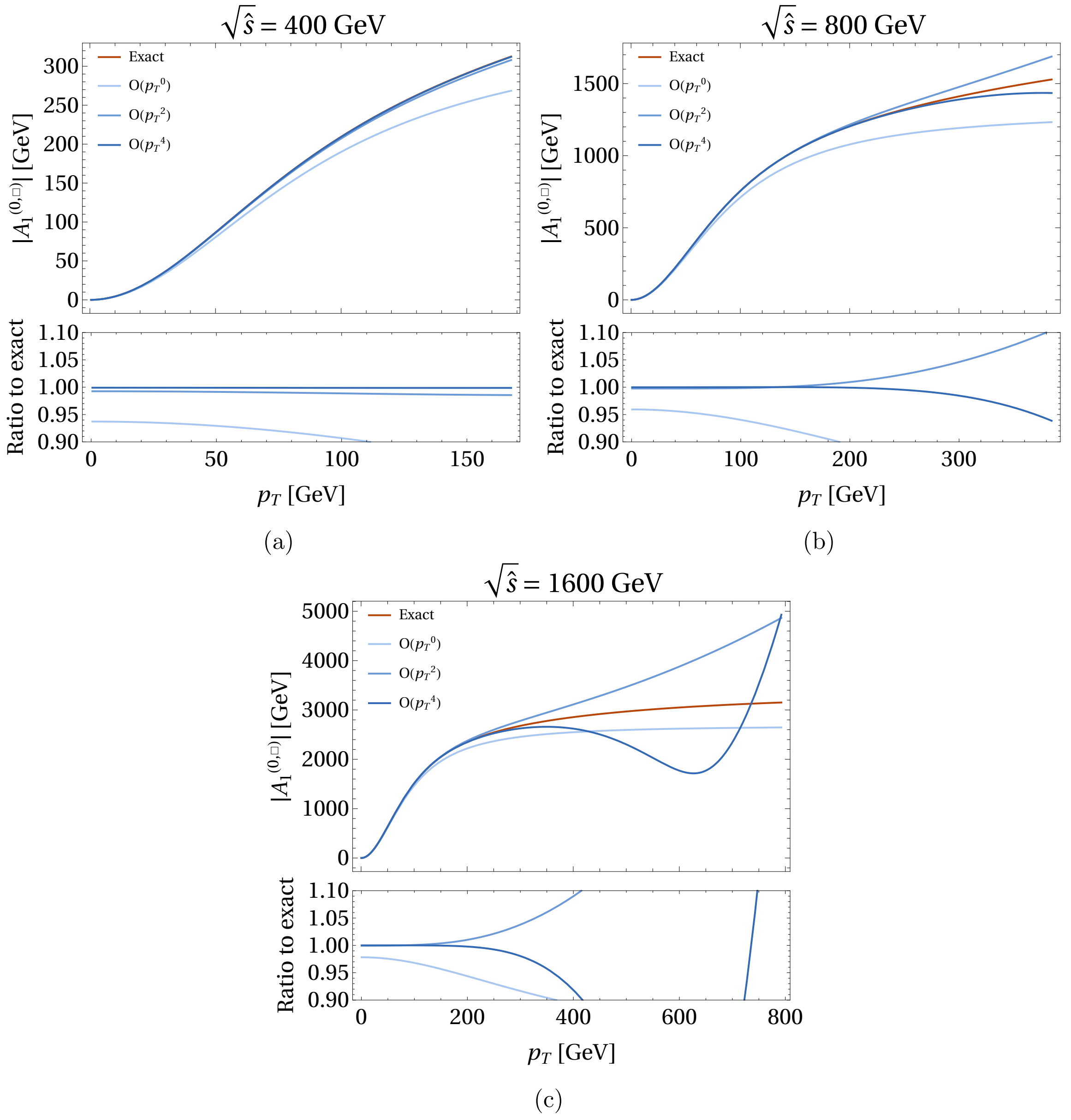

Figure 2.4: Absolute value of the $\mathcal{A}_1^{(0,\square)}$ form factor, for the same values of $\sqrt{\hat{s}}$ as in fig. 2.3: the blue lines represent the first three orders of the expansion, while the brown line stands for the exact result. The bottom part of each graph shows the ratio of the various orders of the p_T expansion to the exact result.

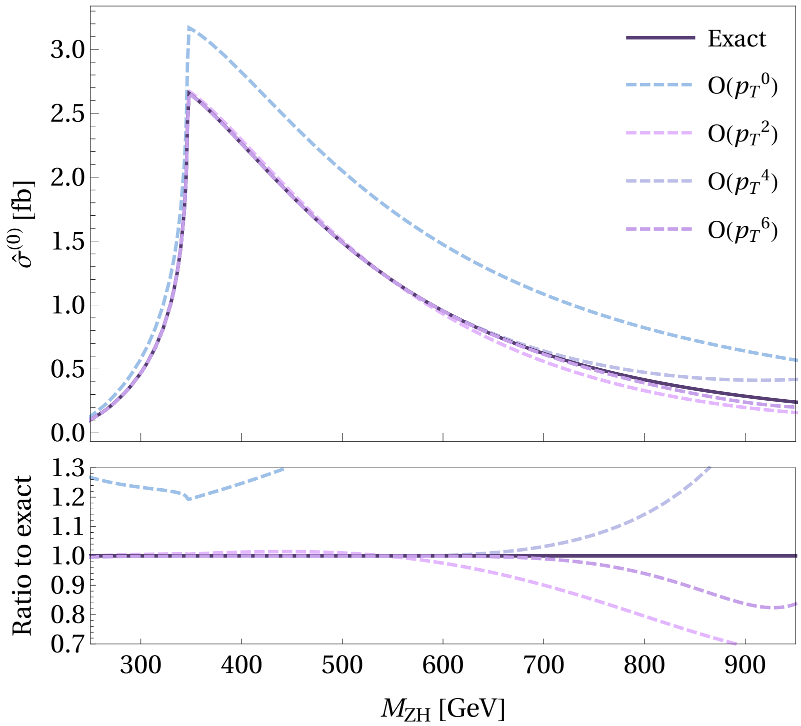

Figure 2.5: Partonic cross section at LO, as a function of the invariant mass M_{ZH}. The exact result is shown as a dark solid line, while different orders of the p_T expansion are shown as dashed lines. In the bottom part, the ratio of each order over the exact result is shown.

where $\hat{t}^{\pm}$ are the same quantities defined in eq.(2.40).

In fig. 2.5 we show $\hat{\sigma}^{(0)}$ as a function of the invariant mass of the ZH system, and we compare the results of the first four orders of the p_T expansion (dashed lines) against the exact result (dark solid line). While the first order in the expansion allows only to reproduce the qualitative behavior of the exact prediction, already the second order provides a good approximation of the cross section, as can be observed from the bottom part of fig. 2.5, showing the ratio of each order to the exact result. If two more orders are included, the accuracy of the p_T expansion is improved and the convergence is extended up to a value of $M_{ZH} \simeq 700$ GeV. Specifically, from the numerical results presented in tab. 2.1 one can see that the $\mathcal{O}(p_T^4)$ results can reproduce the exact prediction at the permille level for $M_{ZH} \lesssim 600$ GeV, while the same level of agreement is extended to $M_{ZH} \lesssim 700$ GeV when also $\mathcal{O}(p_T^6)$ terms are included. This limit can be related to the limit in p_T discussed in sec. 2.4. Indeed, eq.(2.58) implies that the condition $p_T \lesssim 2m_t$ required for the convergence of the expansion is always fulfilled for $\sqrt{\hat{s}} \lesssim 700$ GeV.

2.8 NLO Results of the p_T Expansion

Main features of the NLO amplitude In the previous section we showed that the p_T expansion can provide, in its range of validity, an accurate approximation of the LO cross section for $gg \to ZH$. In the study of the NLO contribution, the two-loop integrals involved can be treated conceptually on the same way from the point of view of the p_T expansion.

Table 2.1: Numerical results for the partonic cross section using the first four orders in the p_T expansion and the exact prediction.

M_{ZH} [GeV]	$\mathcal{O}(p_T^0)$	$\mathcal{O}(p_T^2)$	$\mathcal{O}(p_T^4)$	$\mathcal{O}(p_T^6)$	Exact
250	0.1256	0.0994	0.0991	0.0990	0.0990
300	0.5790	0.4717	0.4689	0.4686	0.4686
350	3.1596	2.6609	2.6434	2.6415	2.6413
400	2.8220	2.2921	2.2644	2.2617	2.2614
500	2.0490	1.5036	1.4871	1.4876	1.4879
600	1.4735	0.9300	0.9549	0.9528	0.9532
700	1.0851	0.5588	0.6403	0.6143	0.6203
800	0.8223	0.3300	0.4737	0.3903	0.4151
900	0.6400	0.1984	0.4128	0.2399	0.2865

Then, it is reasonable to assume that the p_T expansion can achieve a level of accuracy comparable to the one at LO. There are, however, several sources of complication that will be addressed in this subsection and in the following ones. First, the number of diagrams involved at NLO is clearly larger than at LO. Also, the number of scalar integrals appearing in the NLO form factors is drastically increased, so that the intermediate expressions arising in the IBP reduction can become quite large. Furthermore, the master integrals after the IBP reduction are two-loop integrals, and even with the simplified structure discussed in sec. 2.5 the task of evaluating these integrals is challenging. Finally, while we observed that the LO results are finite in $D = 4$ dimensions, the integrals appearing in the NLO results are both UV and IR divergent.

The relevant NLO diagrams generated with `FeynArts` are 86. Of these, 35 are two-loop triangles like in figs. 2.6(a,b) and 47 are two-loop boxes as figs. 2.6(d-h); these NLO diagrams are obtained by attaching extra gluons to the LO ones in all possible ways. Also, a new topology represented by a set of 4 double-triangle diagrams (fig. 2.6(c)) appears for the first time at NLO. We then separate the NLO form factors as a sum of the diagrams with different topologies. So, recalling eq.(2.48),

$$\mathcal{A}_i^{(1)} = \mathcal{A}_i^{(1,\triangle)} + \mathcal{A}_i^{(1,\Box)} + \mathcal{A}_i^{(1,\bowtie)}. \tag{2.62}$$

Following the same strategy discussed in sec. 2.7, we evaluated the two-loop triangles in the $\mathcal{A}_i^{(1,\triangle)}$ in Landau gauge, where only the diagrams with an $\hat{s}$-channel G^0 propagator are expected to give a nonzero contribution. The hardest part of these diagrams is clearly represented by the 1PI two-loop triangles, which can be associated to the production of a pseudoscalar boson via gluon fusion. In fact, the SM prediction for this process is known through NLO [76, 77] and we adapted the findings of ref. [77] to obtain exact analytical results for the $\mathcal{A}_i^{(1,\triangle)}$, which we present in app. A.2. Also the double-triangle diagrams in the $\mathcal{A}_i^{(1,\bowtie)}$ form factors can be computed exactly, as they are simply the product of two one-loop diagrams connected via a $\hat{t}$- or $\hat{u}$-channel gluon propagator. We present the results obtained using `FeynCalc` in terms of Passarino-Veltman scalar functions in app. A.2.

Box diagrams at NLO Concerning the box diagrams in the $\mathcal{A}_i^{(1,\Box)}$, the evaluation of the related two-loop integrals has proven to be the most difficult task in the whole computation,

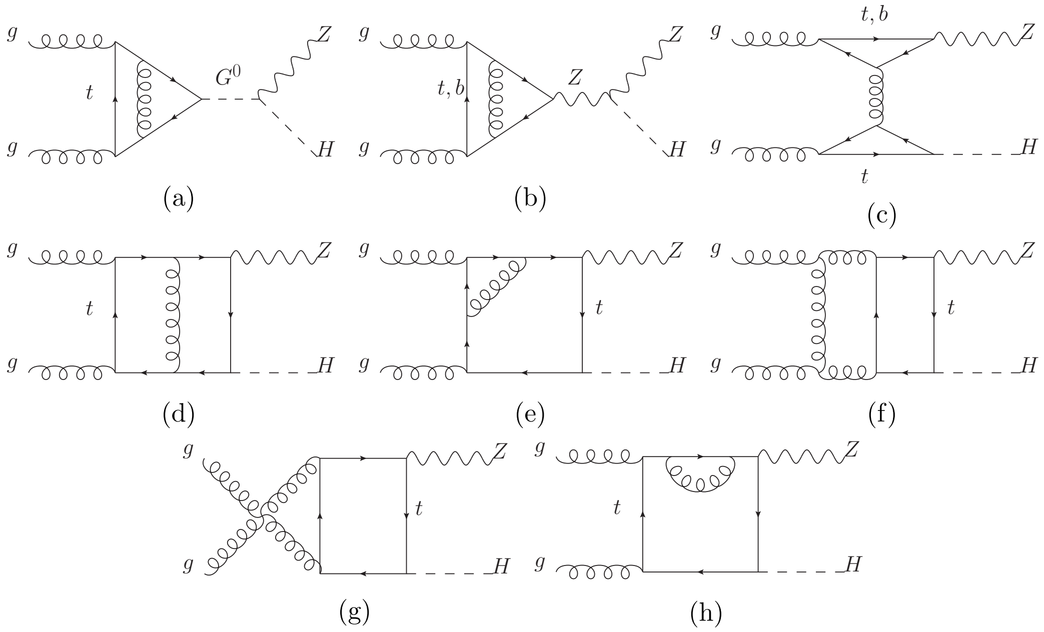

Figure 2.6: Representative Feynman diagrams contributing to the $gg \to ZH$ amplitude at NLO. The two-loop triangle (a, b) and box (d - h) topologies are supplemented with double-triangle diagrams as in (c).

and we are going to discuss some technical details before presenting the results. The contraction of the amplitude with the projectors produces expressions for the form factors that are already involved. Because of this, we could perform the p_T expansion only up to and including $\mathcal{O}(p_T^4)$ terms. However, from the comparison with the LO result in the previous section, we have seen that three orders in the p_T expansion could already approximate the exact result very well.

We find that the dimension of the files for the $\mathcal{O}(p_T^4)$ term reaches the order of 100 MB. When dealing with these kind of files within `Mathematica`, key factors are the choice of the functions for the symbolic manipulations (e.g. `Simplify`, `Collect` , `Factor`, `Together`) and the order in which these manipulations are performed in the code. After the p_T expansion, we find that all the scalar integrals in the box form factors can be assigned to one of nine families of two-loop integrals which, following the definition in eq.(2.44), depend on nine n_i indices

$$J_i(n_1, \ldots, n_9) = \int d^D q_1 d^D q_2 \, \frac{(q_1 \cdot r_\perp)^{n_8} (q_2 \cdot r_\perp)^{n_9}}{D_1^{n_1} \cdots D_7^{n_7}} \qquad i \in \{1, 2, \ldots, 9\} \tag{2.63}$$

where q_1 and q_2 are the loop-momenta, seven indices are related to the powers of the propagator denominators and two irreducible scalar products appear in the numerator. The families used for the IBP reduction are listed in tab. 2.2. The analysis of the nine families using `LiteRed` found 52 MIs. It is interesting to note that when these families are collectively analyzed with `LiteRed` it turns out that all the integrals belonging to the $J_9(n_1, \ldots, n_9)$ family can be decomposed in terms of integrals belonging to the other eight families (this is achieved using the command `FindSymmetries` in the analysis of the families in `LiteRed`).

The IBP reduction at NLO has been the most challenging step from a computational point of view. After every integral has been rewritten in the usual notation of eq.(2.63), the form

Table 2.2: Denominator bases for the two-loop scalar integrals associated to p_T-expanded box form factors.

	$J_1(n_1,\ldots,n_9)$	$J_2(n_1,\ldots,n_9)$	$J_3(n_1,\ldots,n_9)$
D_1	$(q_1+q_2-p_1)^2$	$(q_1+q_2-p_1)^2$	$(q_1+q_2-p_1)^2$
D_2	$(q_1-p_1)^2-m_t^2$	$(q_1-p_1)^2-m_t^2$	$(q_1-p_1)^2-m_t^2$
D_3	$(q_1-p_2)^2-m_t^2$	$q_1^2-m_t^2$	$q_1^2-m_t^2$
D_4	$q_1^2-m_t^2$	$(q_1+p_2)^2-m_t^2$	$(q_1+p_2)^2-m_t^2$
D_5	$(q_2-p_1)^2-m_t^2$	$(q_2-p_2)^2-m_t^2$	$(q_2-p_1)^2-m_t^2$
D_6	$(q_2-p_1+p_2)^2-m_t^2$	$(q_2-p_1-p_2)^2-m_t^2$	$(q_2-p_1-p_2)^2-m_t^2$
D_7	$q_2^2-m_t^2$	$q_2^2-m_t^2$	$q_2^2-m_t^2$
D_8	$q_1\cdot r_\perp$	$q_1\cdot r_\perp$	$q_1\cdot r_\perp$
D_9	$q_2\cdot r_\perp$	$q_2\cdot r_\perp$	$q_2\cdot r_\perp$
	$J_4(n_1,\ldots,n_9)$	$J_5(n_1,\ldots,n_9)$	$J_6(n_1,\ldots,n_9)$
D_1	q_2^2	$(q_1-p_1)^2$	$(q_1+q_2-p_1)^2$
D_2	$(q_2+p_2)^2$	q_1^2	$(q_1-p_1)^2-m_t^2$
D_3	$(q_1-p_1)^2-m_t^2$	$(q_1+p_2)^2$	$(q_1-p_2)^2-m_t^2$
D_4	$(q_1-p_2)^2-m_t^2$	$(q_2-p_1)^2-m_t^2$	$q_1^2-m_t^2$
D_5	$q_1^2-m_t^2$	$(q_1+q_2-p_1)^2-m_t^2$	$(q_2-p_1+p_2)^2-m_t^2$
D_6	$(q_1+q_2-p_1)^2-m_t^2$	$(q_1+q_2-p_1+p_2)^2-m_t^2$	$q_2^2-m_t^2$
D_7	$(q_1+q_2)^2-m_t^2$	$q_2^2-m_t^2$	$(q_2+p_2)^2-m_t^2$
D_8	$q_1\cdot r_\perp$	$q_1\cdot r_\perp$	$q_1\cdot r_\perp$
D_9	$q_2\cdot r_\perp$	$q_2\cdot r_\perp$	$q_2\cdot r_\perp$
	$J_7(n_1,\ldots,n_9)$	$J_8(n_1,\ldots,n_9)$	$J_9(n_1,\ldots,n_9)$
D_1	$(q_1-p_1)^2$	q_1^2	$(q_1-p_1)^2$
D_2	q_1^2	$(q_1+p_1)^2$	q_1^2
D_3	$(q_1+p_2)^2$	$q_2^2-m_t^2$	$(q_1+p_2)^2-m_t^2$
D_4	$(q_2-p_2)^2-m_t^2$	$(q_2+p_2)^2-m_t^2$	$(q_2-p_1)^2-m_t^2$
D_5	$(q_2-p_1-p_2)^2-m_t^2$	$(q_1+q_2)^2-m_t^2$	$(q_2-p_1-p_2)^2-m_t^2$
D_6	$(q_1+q_2-p_1)^2-m_t^2$	$(q_1+q_2+p_2)-m_t^2$	$(q_1+q_2-p_1)^2-m_t^2$
D_7	$q_2^2-m_t^2$	$(q_1+q_2+p_1+p_2)^2-m_t^2$	$q_2^2-m_t^2$
D_8	$q_1\cdot r_\perp$	$q_1\cdot r_\perp$	$q_1\cdot r_\perp$
D_9	$q_2\cdot r_\perp$	$q_2\cdot r_\perp$	$q_2\cdot r_\perp$

factors consist on average of $\mathcal{O}(200\,000)$ scalar integrals, and the symbolic rules for a single integral can be already very lengthy . In total, the files containing the symbolic rules for a single form factor[9] are around 500 MB in size. Once the rules are applied, a form factor is now written as a linear combination of MIs, but the coefficients of the latter are huge and must be simplified and expanded in the ε parameter of Dimensional Regularization. For the $\mathcal{O}(p_T^4)$ contribution to the form factors, this step could require several days to be completed. At the end of the calculation, each order of the p_T expansion for a given form factor occupies a few hundreds of kB[10]. The analytical expressions however are still too involved to be included in the thesis, and we present our results graphically in the following sections. The IBP reduction implemented in the procedure described above took about two weeks of computing time for the whole set of $\mathcal{A}_i^{(1,\square)}$. We remark, however, that all the operations described above have been performed on a simple desktop machine. The results have been obtained using a common processor, although at least 64GB of RAM would be recommended to safely handle the intermediate expressions in the IBP reduction.

2.8.1 Master Integrals

The MIs that form the basis found by `LiteRed` are the ultimate building blocks of the NLO form factors in the p_T expansion, and the last step before obtaining a complete result consists in the evaluation of these MIs. All of the 52 MIs (which are listed in app. A.3) have been already computed in the literature [77–82]. We remark that the same set of MIs was found in the analysis of the $gg \to HH$ process in ref. [39]. A large group made of 50 MIs can be expressed analytically in terms of a class of special functions known as *Goncharov Polylogarithms* (GPL) [83], which are defined recursively as [84]

$$
\begin{aligned}
G(a_1; z) &= \int_0^z \frac{dt}{t - a_1}, \quad G(z) = 1, \quad (a_1 \neq 0) \\
G(a_1, \ldots, a_n; z) &= \int_0^z \frac{dt}{t - a_1} G(a_2, \ldots, a_n; t).
\end{aligned}
\tag{2.64}
$$

In our computation, we evaluated these functions numerically using the code `handyG` [85].

The remaining two MIs are elliptic integrals evaluated in ref. [82]; in order to have a fast numerical evaluation we used the `Fortran` routine of ref. [86] which relies on a semi-analytical evaluation of the two integrals. The routine of [86] has been interfaced with `Mathematica` using the MathLink protocol.

2.8.2 Renormalization

The MIs obtained after the IBP reduction are UV and IR divergent. Specifically, when the MIs are expressed as an expansion in ε and combined with the respective coefficients, the NLO form factors exhibit poles up to $1/\varepsilon^4$. These poles are to be cancelled partly at the amplitude-level due to renormalization, and partly at the cross-section level with the inclusion

[9] We notice here that most of (though not all) the scalar integrals appearing in one form factor do appear also in the other ones. For the calculation described in this thesis, the IBP reduction has been performed separately by using a single processor core for each form factor. One could make this step more efficient by collecting the integrals in all the form factors and performing the IBP reduction only once. Still, the major bottleneck in computing time is the simplification of the form factors after the IBP reduction. Unfortunately, this step is form-factor-dependent.

[10] The inevitability of large intermediate expressions is a well-known problem in the IBP reduction business.

of the contribution from real radiation. Here we discuss the treatment of the first kind of divergences, while the problem of IR divergences is addressed in the following subsection.

The parameters in the SM Lagrangian that need to be renormalized in the calculation of the NLO diagrams are the external gluons wave-functions, the strong coupling constant α_S and the mass of the top quark m_t. We note here that the relevant Feynman diagrams at NLO were generated within the Background-Field formalism [87], using a custom `FeynArts` model file that has been used also in refs. [31,39]. In this approach, the poles in ε associated to the renormalization of the strong coupling and of the gluon wave-function, which are proportional to the one-loop $\beta-$function of the strong coupling, β_0, cancel exactly with part of the IR-divergent terms that must be subtracted in order to make the virtual result finite (see discussion in the following subsection). Therefore we omit these terms in our results.

The renormalization of the top mass has been performed in the on-shell (OS) scheme. Specifically, the UV divergent integrals that one needs to consider for the top mass renormalization come exclusively from diagrams in which a virtual gluon is emitted and reabsorbed in a single internal fermionic leg (an example for the box topologies is depicted in fig.2.6(h)). If we define the NLO form factors before the top-mass renormalization as $\mathcal{A}_i^{(1,\mathrm{UV})}$ then we have that the renormalized NLO result is given by

$$\mathcal{A}_i^{(1)} = \mathcal{A}_i^{(1,\mathrm{UV})} + \delta_{\mathrm{OS}}, \tag{2.65}$$

where

$$\delta_{\mathrm{OS}} = 2m_t^2 \left(\frac{\partial}{\partial m_t^2}\mathcal{A}_i^{(0)}\right)\left[-\frac{C_F}{4}\left(\frac{3}{\varepsilon} + 4 - 3\log\left(\frac{m_t^2}{\mu_R^2}\right)\right)\right] \tag{2.66}$$

with $C_F = 4/3$ the Casimir of the fundamental representation of $SU(3)$. The term in square brackets is connected to the mass counterterm derived from the calculation of the top quark self-energy at one-loop. We point out that in the calculation of the latter no $\mathcal{O}(\varepsilon)$ terms need to be taken into account, since the LO result $\mathcal{A}_i^{(0)}$ is UV finite.

2.8.3 Subtraction of Infra-Red Divergences

It is known that the cancellation of the UV poles due to the renormalization procedure does not eliminate all the sources of divergence in the Feynman integrals. There are also IR divergences related to the presence of massless particles in the relevant diagrams, i.e. gluons in our case. These divergences are of a different nature than the UV ones, and are connected to the degree of exclusiveness of the process considered here. Indeed, the Kinoshita-Lee-Nauenberg theorem [88,89] states that for sufficiently inclusive observables all the IR divergences have to be cancelled. In the specific case of $gg \to ZH$, the IR divergences are to be cancelled by the *real* corrections associated to diagrams where additional partons are emitted from the external particles. It has been shown [90] that IR divergences are universal at NLO, in the sense that the IR singular terms depend only on the kind and on the number of external partons involved in a given process. It is then possible to define a universal term that can be subtracted to obtain a result for the virtual contribution that is both UV and IR finite. If we define the UV-renormalized but still IR-divergent form factors as $\mathcal{A}_i^{(1,\mathrm{IR})}$, we obtain a UV- and IR-finite result via

$$\mathcal{A}_i^{(1)} = \mathcal{A}_i^{(1,\mathrm{IR})} + \delta_{gg,C_A} \tag{2.67}$$

where

$$\delta_{gg,C_A} = \frac{C_A}{2\varepsilon^2}\mathcal{A}_i^{(0)}\left(-\frac{\hat{s}}{\mu_R^2}\right)^{-\varepsilon}, \tag{2.68}$$

$C_A = 3$ is the Casimir of the adjoint representation of $SU(3)$, and terms up to $\mathcal{O}(\varepsilon^2)$ are understood to be included in the result for $\mathcal{A}_i^{(0)}$.

2.8.4 The Problem with γ^5

As stated in the previous sections, we used DR to regularize both UV and IR divergences associated to the loop integrals. Since the amplitude receives a contribution from the axial coupling of the Z boson to top quarks and from the pseudoscalar coupling of the neutral Goldstone boson to top quarks, using DR brings the issue of the treatment of the Dirac γ^5 matrix in D-dimensions. Indeed, the assumption that γ^5 anticommutes with all the other Dirac matrices is in conflict with the ciclicity property of the trace for $D \neq 4$ and this fact implies that the usual relation involving the traces of γ^5

$$\mathrm{Tr}\left(\gamma^\mu\gamma^\nu\gamma^\rho\gamma^\sigma\gamma^5\right) = 4i\epsilon^{\mu\nu\rho\sigma}$$

cannot be recovered in 4 dimensions from the result in $D \neq 4$. Among the various schemes proposed in the literature [6,91,92] to circumvent this issue, we used the Larin prescription [93] which is implemented in `FeynCalc` as follows

1. Whenever a trace of Dirac matrices involves an odd number of γ^5, these are all anti-commuted to the right of the trace.
2. The combination $\gamma^\mu\gamma^5$ inside the trace is replaced with the quantity $-i/(3!)\,\epsilon^{\mu\alpha\beta\delta}\,\gamma^\alpha\gamma^\beta\gamma^\delta$.
3. The contractions with the Levi-Civita tensor are performed as if the latter was a D-dimensional object[11]. Specifically, the full contraction of two Levi-Civita tensors is written as a linear combination of D-dimensional metric tensors.

The use of the Larin prescription allows to deal efficiently with the issue of γ^5 in practical calculations. However, a finite renormalization of the results is still needed in order to restore the Ward Identities for the axial current [93]. The required finite counterterm differs according to the coupling of the fermions being of pseudoscalar (as in the diagrams of fig. 2.6(a)) or axial (as in the box diagrams) type. In particular, if we define $\mathcal{A}_i^{(1,\Box,\mathrm{NDR})}$ and $\mathcal{A}_i^{(1,\triangle,\mathrm{NDR})}$ to be the form factors obtained with the Larin prescription implemented as above, then the correct renormalized form factors are computed as

$$\begin{aligned}\mathcal{A}_i^{(1,\Box)} &= \mathcal{A}_i^{(1,\Box,\mathrm{NDR})} - \frac{\alpha_S}{\pi}C_F\mathcal{A}_i^{(0,\Box)}\\ \mathcal{A}_i^{(1,\triangle)} &= \mathcal{A}_i^{(1,\triangle,\mathrm{NDR})} - 2\frac{\alpha_S}{\pi}C_F\mathcal{A}_i^{(0,\triangle)}.\end{aligned} \tag{2.69}$$

We point out that the finite renormalization of the $\mathcal{A}_i^{(1,\bowtie)}$ form factors is needed only from NNLO.

As a check of consistency, the results of the p_T expansion for $\mathcal{A}_i^{(1,\Box)}$ and $\mathcal{A}_i^{(1,\triangle)}$ were compared to an independent calculation in the LME, using a different regularization procedure, namely Pauli-Villars regularization, in which all the steps are always performed in 4 dimensions, where the γ^5 matrix is defined consistently.

[11] This approach corresponds to the so-called *Naive Dimensional Regularization* (NDR)

2.8.5 Finite NLO Form Factors

We have shown how to remove all the sources of divergence from the $\mathcal{A}_i^{(1)}$ and now we are left with a result for the NLO form factors that is finite in $D = 4$ dimensions. In fig. 2.7 we show the results for the $\mathcal{A}_1^{(1,\Box)}$ form factor, following the same style of fig. 2.3. An exact result at NLO is not available, so only the first three orders of the p_T expansion are showed in each plot of fig. 2.7. For these, we observe a similar behavior as for $\mathcal{A}_1^{(0,\Box)}$. When the maximum p_T value allowed by a fixed $\sqrt{\hat{s}}$ is smaller than about 300 GeV (as in fig.2.7 (a, b)) the p_T expansion shows a good convergence for the whole p_T range. When higher energies are considered (fig. 2.7(c-f)), the phase space allows values of p_T violating the condition (2.34); for these values, the p_T expansion shows a divergent behavior and cannot be trusted to reproduce the exact result. Additional plots for the NLO box form factors can be found in app. A.4, see fig. A.3.

2.8.6 Finite Part of the Virtual Corrections

We are now in the position to present the contribution to the NLO partonic cross section for $gg \to ZH$ that is associated only to the virtual QCD corrections, identified as $\Delta\hat{\sigma}_{virt}$. We find

$$\Delta\hat{\sigma}_{\text{virt}} = \int_{\hat{t}^-}^{\hat{t}^+} d\hat{t} \frac{1}{16\pi\hat{s}^2} \frac{\alpha_S}{\pi} \mathcal{V}_{\text{fin}} \tag{2.70}$$

where $\mathcal{V}_{\text{fin}}$ refers to the finite part of the virtual corrections and it is defined as in ref. [35]

$$\begin{aligned} \mathcal{V}_{\text{fin}} = \frac{G_F^2 m_Z^2}{16} \left(\frac{\alpha_S}{\pi}\right)^2 \Bigg\{ & \sum_i \left|\mathcal{A}_i^{(0)}\right|^2 \frac{C_A}{2} \left(\pi^2 - \log^2\left(\frac{\mu_R^2}{\hat{s}}\right)\right) \\ & + 2\sum_i Re\left[\mathcal{A}_i^{(0)} \mathcal{A}_i^{(1)*}\right] \Bigg\}. \end{aligned} \tag{2.71}$$

The first term in curly brackets is associated to the finite contribution of the IR counterterms[12], namely to the real corrections, while the second term is related to the interference of the LO and NLO amplitudes for the $2 \to 2$ process. We compared our findings for $\mathcal{V}_{\text{fin}}$ with the numerical results presented in ref. [63]. We were able to compare a few points and we found an agreement at the permille level. This provides another important check of our computation. In fig. 2.8 we present the results for $\Delta\hat{\sigma}_{\text{virt}}$ for the first three orders of the p_T expansion, shown as dashed lines. We note that these are in very good agreement with each other for $M_{ZH} \lesssim 500$ GeV. For comparison, we include the prediction of the same quantity obtained with other analytical approximations. The red solid line shows the result of ref. [28], which is based on an expansion of the NLO amplitude in the infinite-top-mass limit. We see that this approach can reproduce the qualitative behavior of the p_T-expanded prediction, although there are important quantitative differences for invariant masses above the threshold for top-pair production. The results of the LME including $\mathcal{O}(1/m_t^6)$ terms are also shown in fig. 2.8 as a black solid line. While the agreement with the p_T expansion is good slightly above the ZH production threshold, the prediction from the two approximations are visibly different from $M_{ZH} \gtrsim 300$ GeV. We see then that the p_T expansion provides an important

[12]The presence of the $\pi^2 - \log^2\left(\mu_R^2/\hat{s}\right)$ terms is related to the normalization used for the MIs, which is consistent with the one of ref. [39].

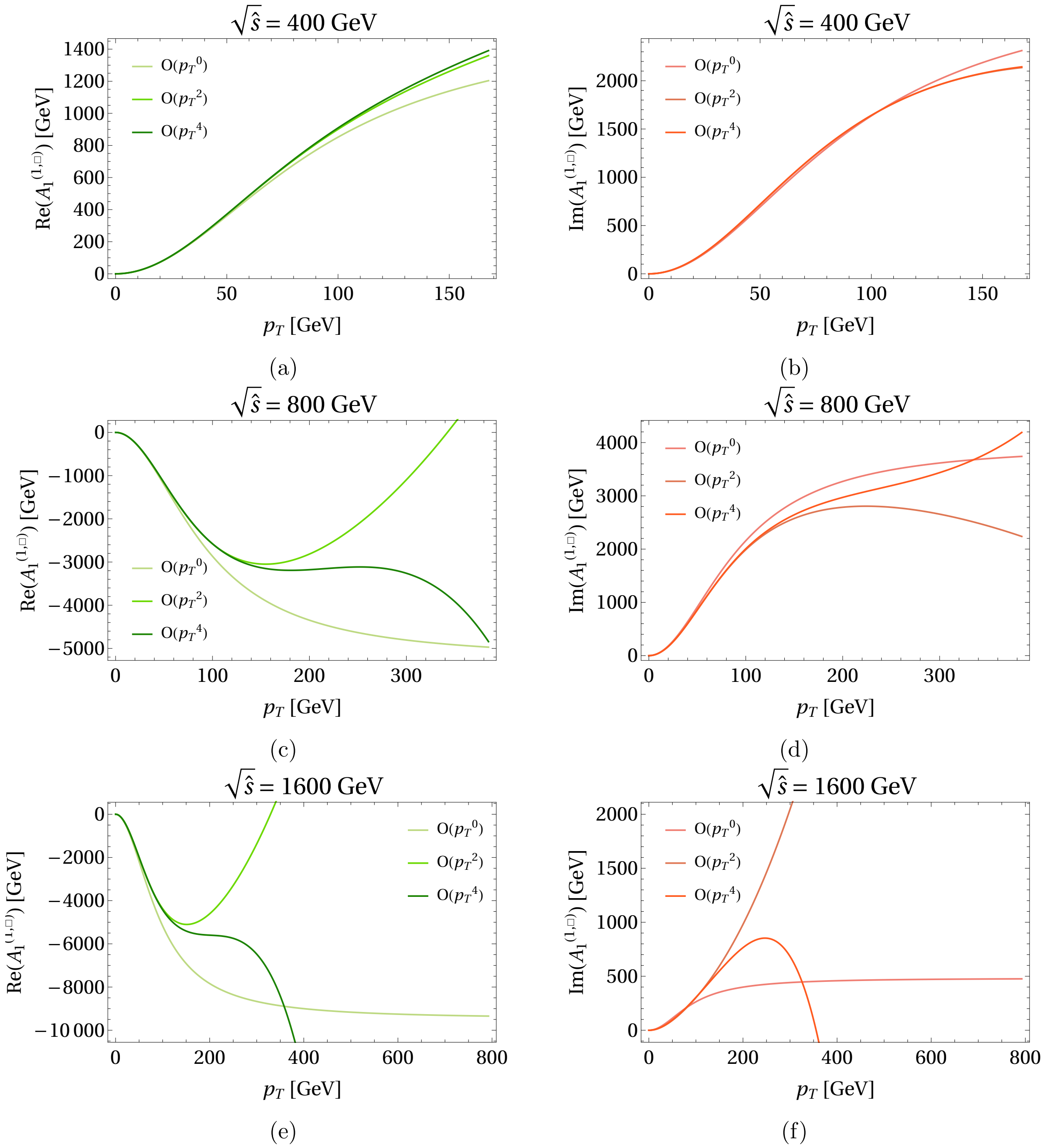

Figure 2.7: Results for the $\mathcal{A}_1^{(1,\square)}$ form factor. The first row shows the first three orders in the p_T expansion for the real (green lines - left) and imaginary (red lines - right) parts, plotted against p_T for a c.o.m. energy of $\sqrt{\hat{s}} = 400$ GeV. The second and third rows show the same quantities as the first row, for higher values of $\sqrt{\hat{s}}$.

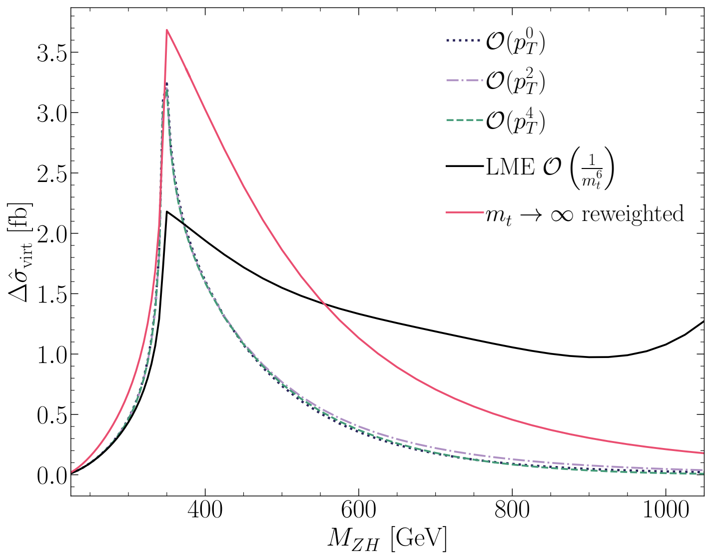

Figure 2.8: Prediction for $\Delta\hat{\sigma}_{\text{virt}}$ as defined in eq.(2.70), as a function of the invariant mass M_{ZH}. The dashed lines show the results obtained with the first three orders of the p_T expansion. The prediction from an independent LME calculation and from the reweighted $m_t \to \infty$ limit considered in ref. [28] are also shown as black and red solid lines, respectively. Taken from [41].

.

improvement in the approximation of the exact result, up to its range of validity $M_{ZH} \lesssim 700$ GeV.

We finally remark that the present calculation is complementary to the results of ref. [35], which cover the region of large transverse momentum of the Z. In chap. 4 we will consider a strategy for merging the two analyses, allowing for an analytic evaluation of the NLO virtual corrections in $gg \to ZH$ in the entire phase space.

Chapter 3

Top-Quark Effects in $gg \to ZZ$

3.1 Introduction

The production of a pair of Z bosons in proton collisions, $pp \to ZZ$, played a crucial role in the discovery of the Higgs boson, as the decay $H \to ZZ^{(*)} \to 4\ell$ was one of the *golden channels* allowing for the first observation of the Higgs at the LHC. Indeed, the leptonic decays of the Z bosons can provide a clean signal in experimental searches. The total cross section for ZZ production is $\mathcal{O}(10\text{ pb})$ for a c.o.m. energy of 13 TeV [94–96]. The importance of this process is still significant in the current investigation of the Higgs properties.

In the theoretical SM prediction of $pp \to ZZ$ production two partonic sub-processes have to be considered. The first is quark-antiquark annihilation, $q\bar{q} \to ZZ$, which gives the largest contribution to the hadronic cross section. The LO for this channel is related to purely EW tree-level diagrams [97], and corrections through NNLO in QCD [98–103] and through NLO in the EW theory [104–106] are available. The second contribution comes from the gluon-initiated channel, $gg \to ZZ$. The LO diagrams for this process are one-loop diagrams, which contribute as a sizable $\mathcal{O}(\alpha_S^2)$ correction to the hadronic cross section, about 10% for $\sqrt{s} = 13$ TeV [107]. The LO diagrams have been computed for the first time in refs. [108, 109]. The $gg \to ZZ$ contribution is particularly relevant for Higgs physics, as it includes the sub-process $gg \to H \to ZZ$. In this thesis we will focus on the gluon-initiated contribution.

The one-loop diagrams for $gg \to ZZ$ at LO feature two topologies: the triangles (see fig. 3.2(a)) are associated to Higgs production, while the box diagrams (fig. 3.2(b)) are related to the process of non-resonant (a.k.a. *continuum*) ZZ production, which constitutes an irreducible background in experimental Higgs searches. Continuum production plays also a relevant role in the indirect determination of the Higgs total decay width, Γ_H [110, 111]. Indeed, in refs. [112, 113] it has been suggested that upper limits on Γ_H can be obtained from the investigation of the invariant-mass distribution away from the resonant peak; if we consider searches in the four-lepton final state, this region corresponds to $m_{4\ell} > 2m_Z$. Additionally, even if Γ_H is about four orders of magnitude smaller compared to the Higgs mass, the invariant-mass distribution off-peak does not decrease very steeply [114]. As a consequence, in the region $m_{4\ell} > 2m_Z$ the interference of the *signal* and *background* amplitudes gives a relevant contribution. For the reasons mentioned above, the knowledge of the gluon-initiated channel beyond the LO contribution is highly desirable.

The NLO corrections to the Higgs-mediated diagrams are known exactly [77, 79, 115]. Concerning the continuum term, exact analytical results for the related two-loop box integrals have been obtained only in the case of loops of massless quarks [116, 117], which clearly is

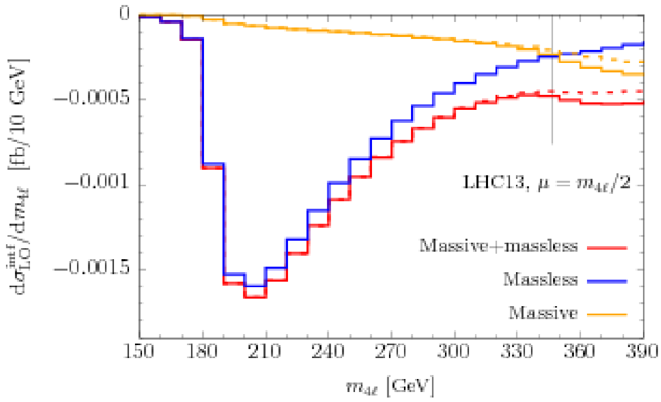

Figure 3.1: Interference of the Higgs-mediated and continuum amplitudes in $gg \to ZZ$ at LO, as a function of the invariant mass of the four-lepton final state. The contribution from massive quarks (orange lines) becomes more and more relevant compared to the one from massless quarks (solid blue line) starting from $m_{4\ell} > 2m_Z$. The dashed lines correspond to the approximation of the massive-quark terms in the LME. The vertical grey line represents the threshold for top-pair production. Taken from [118].

an excellent approximation for the first five quarks. It must be noted that, at variance with what observed in gluon-initiated ZH production, the contribution from light quarks to the $gg \to ZZ$ amplitude is the dominant one, and in fact it constitutes more than 50% of the $\mathcal{O}(\alpha_S^2)$ corrections to ZZ production [100, 107].

The top-quark contribution is not negligible, but it starts to become relevant for invariant masses in the range $m_{4\ell} > 2m_Z$ (see fig. 3.1) and it is expected to be substantial in the region $m_{4\ell} > 2m_t$ [119]. However, the contribution from top quarks is not known exactly, as the scale associated to the mass of the heavy quark complicates the calculation of the two-loop box integrals. Several analytical approximations have been discussed in the literature. The LME has been used in refs. [29, 32, 118] to obtain reliable predictions in the region $2m_Z < m_{4\ell} \lesssim 2m_t$. In ref. [32] an improvement of the LME results by means of conformal mapping and Padé approximants has also been studied. A further improvement of the LME via an expansion around the top threshold has been presented in ref. [119]. Recently, analytical predictions that are reliable for large invariant masses have been obtained using the High-Energy expansion [36]. Still, the latter approach is expected to fail in the region $m_{4\ell} \lesssim 750$ GeV, and also in ref. [36] Padé approximants were used in order to improve the expansion. Finally, results based on numerical approaches have been obtained in refs. [120, 121], showing good agreement with the HE expansion of ref. [36].

In the present chapter, we discuss the computation of the contribution from top-quark loops to $gg \to ZZ$ at NLO, using the p_T expansion presented for gluon-initiated ZH production in chap. 2. Our goal is to provide an accurate approximation of the virtual QCD corrections which can be valid in the invariant-mass region that so far has not been covered by any of the (analytical) approaches discussed above, namely the region $350 \lesssim m_{4\ell} \lesssim 750$ GeV.

In the following section we present the main features of the $gg \to ZZ$ amplitude and we set our notation. In sec. 3.3 we examine the Lorentz structure of the amplitude and its decomposition in terms of Lorentz projectors. In sec. 3.4 we discuss the application of the p_T expansion to $gg \to ZZ$ production, considering the similarities and differences w.r.t. the approach used in chap. 2. In sec. 3.5 we show how well the known LO amplitude can be reproduced by our approximation. We then consider the application of the p_T expansion at NLO and we present our original results in sec. 3.6.

3.2 General Properties of the $gg \to ZZ$ Amplitude

Let us consider the process $g_a^\mu(p_1) g_b^\nu(p_2) \to Z^\rho(p_3) Z^\sigma(p_4)$. The related Feynman amplitude can be written as

$$\mathcal{A} = \sqrt{2} m_Z^2 G_F \, \frac{\alpha_S(\mu_R)}{\pi} \delta_{ab} \; \epsilon_\mu^a(p_1) \epsilon_\nu^b(p_2) \epsilon_\rho^*(p_3) \epsilon_\sigma^*(p_4) \; \hat{\mathcal{A}}^{\mu\nu\rho\sigma}(p_1, p_2, p_3) \tag{3.1}$$

where the polarization vectors of the gluons and the Z bosons are $\epsilon_\mu^a(p_1), \epsilon_\nu^b(p_2)$ and $\epsilon_\rho(p_3), \epsilon_\sigma(p_4)$, respectively. Since all the external particles are gauge bosons the tensor $\hat{\mathcal{A}}^{\mu\nu\rho\sigma}(p_1, p_2, p_3)$, which is analyzed in the next section, will depend on four Lorentz indices.

In this chapter we will consider on-shell external particles

$$p_1^2 = p_2^2 = 0 \qquad p_3^2 = p_4^2 = m_Z^2. \tag{3.2}$$

Assuming all momenta to be incoming, the partonic Mandelstam variables are defined as

$$\hat{s} = (p_1 + p_2)^2, \quad \hat{t} = (p_1 + p_3)^2, \quad \hat{u} = (p_2 + p_3)^2 \tag{3.3}$$

and the relation

$$\hat{s} + \hat{t} + \hat{u} = 2 m_Z^2 \tag{3.4}$$

is satisfied.

By analogy with eqs.(2.16,2.17), it is easy to see that the transverse momentum of each one of the Z bosons is written as

$$p_T^2 = \frac{\hat{t}\hat{u} - m_Z^4}{\hat{s}}, \tag{3.5}$$

whereas in the forward kinematic region one has

$$\begin{aligned} \hat{t} &= -\frac{1}{2}\left(\hat{s} - 2m_Z^2 - \sqrt{\hat{s}^2 - 4\hat{s}m_Z^2 - 4\hat{s}p_T^2}\right) \\ \hat{u} &= -\frac{1}{2}\left(\hat{s} - 2m_Z^2 + \sqrt{\hat{s}^2 - 4\hat{s}m_Z^2 - 4\hat{s}p_T^2}\right). \end{aligned} \tag{3.6}$$

We further assume the transversality of all the external polarization vectors w.r.t the respective four-momentum

$$\epsilon(p_i) \cdot p_i = 0 \qquad i = 1, \ldots, 4, \tag{3.7}$$

and Bose symmetry under the exchange of the initial gluons and of the final Z bosons implies the following relations

$$\begin{aligned} \hat{\mathcal{A}}^{\mu\nu\rho\sigma}(p_1, p_2, p_3, p_4) &= \hat{\mathcal{A}}^{\nu\mu\rho\sigma}(p_2, p_1, p_3, p_4) \\ \hat{\mathcal{A}}^{\mu\nu\rho\sigma}(p_1, p_2, p_3, p_4) &= \hat{\mathcal{A}}^{\mu\nu\sigma\rho}(p_1, p_2, p_4, p_3). \end{aligned} \tag{3.8}$$

If we study the amplitude by looking at the couplings of the external particles to the internal lines in the Feynman diagrams, we notice some useful properties. The Higgs-mediated diagrams will necessarily depend on the metric tensor $g^{\rho\sigma}$ due to the HZZ coupling in the final state, whereas gluon-initiated Higgs production is proportional to the combination $(g^{\mu\nu} p_1 \cdot p_2 - p_1^\mu p_2^\nu)$ due to gauge invariance.

In the box diagrams related to continuum production, the presence of two Z bosons that couple to the internal fermion line requires a careful analysis. If we recall that the Z-top coupling in the SM is given by

$$- i \frac{g}{\cos\theta_W} \gamma^\mu (g_V - g_A \gamma^5), \tag{3.9}$$

with

$$g_V = \frac{1}{2} - \frac{4}{3} \sin\theta_W \qquad g_A = \frac{1}{2}, \tag{3.10}$$

we see that three separate contributions to the box amplitude can be identified: a vector-vector part, which will be proportional to g_V^2, an axial-axial part proportional to g_A^2 and a mixed part proportional to $g_V g_A$. However, the latter component must vanish because of Furry's theorem, as the external gluons provide two more vector couplings. Furthermore, when considering the contribution proportional to g_A^2, the two γ^5 matrices occurring in the Dirac traces can be safely anticommuted close to each other in $D = 4$ dimensions, where one can use the relation $\left(\gamma^5\right)^2 = 1$. As a consequence, Lorentz structures involving Levi-Civita tensors are not expected to contribute to the final result for the box amplitudes, allowing to use Naive Dimensional Regularization unambiguously in their calculation. The same reasoning does not apply to the double triangles in the NLO corrections (see fig. 3.5(c)), as in that case the two Z bosons couple to independent fermion lines. However, the double triangles contribute for the first time at NLO and, at the order we are considering, no finite renormalization is needed. We conclude that in the calculation of the amplitude at NLO the issue of the treatment of γ^5 in Dimensional Regularization can be circumvented.

3.3 Projectors

The structure of the Lorentz tensor $\hat{\mathcal{A}}^{\mu\nu\rho\sigma}$ is definitely more complicated compared to the case of ZH production, discussed in sec. 2.3. Due to the extra Lorentz index, the most general Lorentz decomposition involves 138 tensors. The number of independent tensors can be reduced by exploiting the transversality condition (3.7) and the properties of gauge invariance and Bose symmetry which the amplitude must respect. However, the choice of a specific polarization of the initial gluons, namely

$$\epsilon(p_1) \cdot p_2 = 0 \qquad \epsilon(p_2) \cdot p_1 = 0 \tag{3.11}$$

can drastically simplify the structure of $\hat{\mathcal{A}}^{\mu\nu\rho\sigma}$. This choice has been used in refs. [36,116,122] and we adopt it in our work in order to facilitate the comparison with previous results. In particular, we assume the following relations for the polarization sums of the external particles

$$\begin{aligned}
\sum_\lambda \epsilon_{\lambda,\mu}(p_1) \epsilon^*_{\lambda,\alpha}(p_1) &= -g_{\mu\alpha} + \frac{p_{1\mu} p_{2\alpha} + p_{2\mu} p_{1\alpha}}{p_1 \cdot p_2} \\
\sum_\lambda \epsilon_{\lambda,\nu}(p_2) \epsilon^*_{\lambda,\beta}(p_2) &= -g_{\nu\beta} + \frac{p_{2\nu} p_{1\beta} + p_{1\nu} p_{2\beta}}{p_1 \cdot p_2} \\
\sum_\lambda \epsilon_{\lambda,\rho}(p_3) \epsilon^*_{\lambda,\gamma}(p_3) &= -g_{\rho\gamma} + \frac{p_{3\rho} p_{3\gamma}}{m_Z^2} \\
\sum_\lambda \epsilon_{\lambda,\sigma}(p_4) \epsilon^*_{\lambda,\delta}(p_4) &= -g_{\sigma\delta} + \frac{p_{4\sigma} p_{4\delta}}{m_Z^2},
\end{aligned} \tag{3.12}$$

where we notice that the first two lines of eq.(3.12) correspond to fixing a gauge for the propagator of the initial gluons.

If we write the amplitude as a linear combination of the single Lorentz tensors $S_i^{\mu\nu\rho\sigma}$ which give a nonzero contribution when eqs.(3.12) are assumed, then the most general form for the amplitude is given by the linear combination of 20 tensors which multiply scalar form factors f_i

$$\hat{\mathcal{A}}^{\mu\nu\rho\sigma}(p_1,p_2,p_3) = \sum_{i=1}^{20} S_i^{\mu\nu\rho\sigma} f_i(\hat{s},\hat{t},\hat{u},m_t,m_Z) \tag{3.13}$$

where

$$\begin{array}{llll}
S_1^{\mu\nu\rho\sigma} = g^{\mu\nu}g^{\rho\sigma} & S_2^{\mu\nu\rho\sigma} = g^{\mu\rho}g^{\nu\sigma} & S_3^{\mu\nu\rho\sigma} = g^{\mu\sigma}g^{\nu\rho} & S_4^{\mu\nu\rho\sigma} = p_1^\rho p_3^\nu g^{\mu\sigma} \\
S_5^{\mu\nu\rho\sigma} = p_2^\rho p_3^\nu g^{\mu\sigma} & S_6^{\mu\nu\rho\sigma} = p_1^\rho p_3^\mu g^{\nu\sigma} & S_7^{\mu\nu\rho\sigma} = p_2^\rho p_3^\mu g^{\nu\sigma} & S_8^{\mu\nu\rho\sigma} = p_3^\mu p_3^\nu g^{\rho\sigma} \\
S_9^{\mu\nu\rho\sigma} = p_1^\rho p_1^\sigma g^{\mu\nu} & S_{10}^{\mu\nu\rho\sigma} = p_1^\rho p_2^\sigma g^{\mu\nu} & S_{11}^{\mu\nu\rho\sigma} = p_1^\sigma p_2^\rho g^{\mu\nu} & S_{12}^{\mu\nu\rho\sigma} = p_2^\rho p_2^\sigma g^{\mu\nu} \\
S_{13}^{\mu\nu\rho\sigma} = p_1^\sigma p_3^\nu g^{\mu\rho} & S_{14}^{\mu\nu\rho\sigma} = p_2^\sigma p_3^\nu g^{\mu\rho} & S_{15}^{\mu\nu\rho\sigma} = p_1^\sigma p_3^\mu g^{\nu\rho} & S_{16}^{\mu\nu\rho\sigma} = p_2^\sigma p_3^\mu g^{\nu\rho} \\
S_{17}^{\mu\nu\rho\sigma} = p_1^\rho p_1^\sigma p_3^\mu p_3^\nu & S_{18}^{\mu\nu\rho\sigma} = p_1^\rho p_2^\sigma p_3^\mu p_3^\nu & S_{19}^{\mu\nu\rho\sigma} = p_1^\sigma p_2^\rho p_3^\mu p_3^\nu & S_{20}^{\mu\nu\rho\sigma} = p_2^\rho p_2^\sigma p_3^\mu p_3^\nu
\end{array} \tag{3.14}$$

We take eqs.(3.13,3.14) as the starting point for the construction of the orthogonal projectors. We also notice that because of Bose symmetry not all the f_i are independent. Furthermore, to the purpose of the p_T expansion, we require the projectors to be linear combinations of the $S_i^{\mu\nu\rho\sigma}$ which must be either symmetric or antisymmetric under the exchange $\{\mu \leftrightarrow \nu\ ,\ p_1 \leftrightarrow p_2\}$. As discussed in sec. 2.4, the latter request allows to recover the correct complete result when the form factors are p_T-expanded only in the forward kinematical region.

The procedure for constructing the projectors follows the same steps discussed in sec. 2.3. We find that the amplitude can be expressed in terms of a set of 20 orthonormal projectors $\mathcal{P}_i^{\mu\nu\rho\sigma}$ as

$$\hat{\mathcal{A}}^{\mu\nu\rho\sigma}(p_1,p_2,p_3) = \sum_{i=1}^{20} \mathcal{P}_i^{\mu\nu\rho\sigma} \mathcal{A}_i(\hat{s},\hat{t},m_Z,m_t) \tag{3.15}$$

where the scalar form factors $\mathcal{A}_i$ depend on the top and Z boson masses and on the independent partonic Mandelstam variables $\hat{s}$ and $\hat{t}$. The projectors respect the analogous orthonormality property of eq.(2.20)

$$\left(-g_{\mu\alpha} + \frac{p_{1\mu}p_{2\alpha} + p_{2\mu}p_{1\alpha}}{p_1 \cdot p_2}\right)\left(-g_{\nu\beta} + \frac{p_{2\nu}p_{1\beta} + p_{1\nu}p_{2\beta}}{p_1 \cdot p_2}\right) \times \tag{3.16}$$

$$\times \left(-g_{\rho\gamma} + \frac{p_{3\rho}p_{3\gamma}}{m_Z^2}\right)\left(-g_{\sigma\delta} + \frac{p_{4\sigma}p_{4\delta}}{m_Z^2}\right) \mathcal{P}_i^{\mu\nu\rho\sigma}\mathcal{P}_j^{\alpha\beta\gamma\delta *} = \delta_{ij}. \tag{3.17}$$

Among the projectors in eq.(3.15), the $\mathcal{P}_i^{\mu\nu\rho\sigma}$ with $i = 1,\ldots,8$ and 20 are antisymmetric under $\{\mu \leftrightarrow \nu\ ,\ p_1 \leftrightarrow p_2\}$, while those with $i = 9,\ldots,19$ are symmetric. The analytical expressions for the projectors are presented in app. B.1. We notice here that the norm of the projectors $\mathcal{P}_{19}^{\mu\nu\rho\sigma}$ and $\mathcal{P}_{20}^{\mu\nu\rho\sigma}$ vanishes in $D = 4$ dimensions. Additionally, we find that the contraction of $\hat{\mathcal{A}}^{\mu\nu\rho\sigma}$ as written in eq.(3.15) with $\mathcal{P}_1^{\mu\nu\rho\sigma}$ and $\mathcal{P}_4^{\mu\nu\rho\sigma}$ vanishes identically when one uses the relations among the f_i in eq.(3.13) connected to Bose symmetry. To summarize, with our choice of projectors only 16 form factors are truly relevant for the calculation of the amplitude. Nonetheless, as a check of consistency we included the form factors $\mathcal{A}_1$, $\mathcal{A}_4$, $\mathcal{A}_{19}$ and $\mathcal{A}_{20}$ in our calculation and we verified that the final result for each of them is zero in

$D = 4$ dimensions. As in ch. 2, we will consider a perturbative expansion of the form factors in the strong coupling

$$\mathcal{A}_i = \mathcal{A}_i^{(0)} + \frac{\alpha_S}{\pi}\mathcal{A}_i^{(1)} + \mathcal{O}(\alpha_S^2) \tag{3.18}$$

where one- and two-loop diagrams contribute respectively at LO ($\mathcal{A}_i^{(0)}$) and NLO ($\mathcal{A}_i^{(1)}$). The form factor defined as in eq.(3.15) are dimensionless.

3.4 p_T Expansion and IBP Reduction for $gg \to ZZ$

The main features and steps of the p_T expansion have already been discussed in the case of ZH production in sec. 2.4. In this section we briefly adapt that same method to the $gg \to ZZ$ process. We therefore introduce the primed Mandelstam variables

$$s' = p_1 \cdot p_2 = \frac{\hat{s}}{2}, \quad t' = p_1 \cdot p_3 = \frac{\hat{t} - m_Z^2}{2}, \quad u' = p_2 \cdot p_3 = \frac{\hat{u} - m_Z^2}{2} \tag{3.19}$$

such that

$$s' + t' + u' = 0, \tag{3.20}$$

and the transverse momentum can be expressed as

$$p_T^2 = \frac{2t'u'}{s'} - m_Z^2. \tag{3.21}$$

By analogy with sec. 2.4, p_3^μ can be expressed as

$$p_3^\mu = -p_1^\mu - \frac{t'}{s'}(p_1 - p_2)^\mu + r_\perp^\mu \tag{3.22}$$

so that in the forward limit $p_3^\mu \simeq -p_1^\mu$ one must have

$$t' \simeq 0 \qquad r_\perp^\mu \simeq 0. \tag{3.23}$$

If we rewrite t' in terms of p_T^2, in the forward region we have

$$t' = -\frac{s'}{2}\left\{1 - \sqrt{1 - 2\frac{p_T^2 + m_Z^2}{s'}}\right\}, \tag{3.24}$$

from which we understand that the expansion parameters to be considered in the $gg \to ZZ$ case are the ratios

$$\frac{p_T^2}{s'} \simeq 0 \qquad \frac{m_Z^2}{s'} \simeq 0 \qquad r_\perp^\mu \simeq 0. \tag{3.25}$$

We notice that, compared to ZH production (cfr. eq.(2.32)), the number of small parameters is reduced by one: this is clearly related to the fact that we are considering external particles with equal masses in the final state of $gg \to ZZ$.

While the different kinematics requires an adaptation of the p_T expansion from the case discussed in sec. 2.4 to ZZ production, the IBP reduction in our calculation is implemented along the same lines of sec. 2.5. In particular, after the scalar form factors $\mathcal{A}_i$ are p_T-expanded in the small parameters of eq.(3.25) and IBP-reduced using `LiteRed`, they can be written as the following series

$$\mathcal{A}_i = \mathcal{N}(p_T^2, m_Z^2) \sum_{N=0}^{\infty} \sum_{i+j=N} c_{ij} (p_T^2)^i (m_Z^2)^j, \tag{3.26}$$

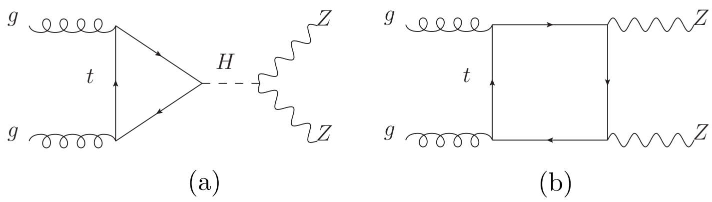

Figure 3.2: Representative Feynman diagrams contributing to the $gg \to ZZ$ amplitude at LO. Triangle topologies with a Higgs boson H (a) are present together with (b) box diagrams. Only the contribution from the top quark loops is shown.

where the c_{ij} coefficients are linear combinations of the MIs resulting from the IBP reduction, which in turn depend only on $\hat{s}$ and m_t^2, and $\mathcal{N}(p_T^2, m_Z^2)$ is an overall normalization factor which may depend on p_T^2 and m_Z^2.

3.5 LO Contribution

In this section we evaluate the LO contribution to the cross section for $gg \to ZZ$ using the p_T expansion, and we compare the results with the known exact expressions. Specifically, we are interested in the calculation of the $\mathcal{A}_i^{(0)}$ form factors. For the practical implementation of the calculation we used the same code presented in sec. 2.6. We note, however, that already at LO some modifications in the routines were required in order to handle the intermediate expressions, which turned out to be significantly more involved than for ZH production.

The diagrams generated using `FeynArts` are four: the diagram shown in fig. 3.2(a) corresponds to the Higgs-mediated contribution and features a triangle topology. The remaining three diagrams are associated to the box topology of fig. 3.2(b) and its crossings. We then split the LO form factors into a triangle and a box contribution

$$\mathcal{A}_i^{(0)} = \mathcal{A}_i^{(0,\triangle)} + \mathcal{A}_i^{(0,\square)}. \tag{3.27}$$

In our calculation we performed the p_T expansion on both contributions, but as in ch. 2 we are going to focus our discussion on the box form factors. We also evaluated the exact results for the $\mathcal{A}_i^{(0)}$ using `FeynCalc` and we checked our expressions with those of ref. [36]. In the comparison with the latter reference we used the relations between our $\mathcal{A}_i$ and the form factors of [36] included in app. B.1.

LO Form Factors After the scalar integrals in the form factors are p_T-expanded, we can identify the same integral families as in ZH production, and the IBP reduction yields a result in terms of the known Passarino-Veltman scalar functions. We now discuss in the detail the results for the $A_9^{(0,\square)}$ form factor[1]. We notice that $A_9^{(0,\square)}$ as well as some other box form factors feature $\mathcal{O}({p_T}^{-2})$ terms, although each form factor is regular in the limit $p_T \to 0$. In the following discussion, we conventionally include these terms in the $\mathcal{O}(p_T^0)$ results. The input parameters used for the numerical evaluation of the form factors are the same as in the previous chapter (see sec. 2.7.2).

In fig. 3.3 we present our results for the absolute value of $A_9^{(0,\square)}$ as a function of p_T, for increasing values of the partonic c.o.m. energy. We see that for values of $\sqrt{\hat{s}}$ that are not

[1]This form factor gives the dominant contribution to the cross section, see app. B.3.

too large (see fig. 3.3(a)) the first three orders of the p_T-expansion (blue lines) are capable of reproducing the exact result (brown line) for every value of p_T. One can notice some spikes in the bottom part of fig. 3.3(a), in correspondence of $p_T \simeq 90$ GeV: these are related to the fact that the form factor is zero[2] for that specific p_T, leading to numerical issues when the ratio p_T-expanded/exact is considered. Nonetheless, when the $\mathcal{O}(p_T^4)$ terms are included in the expanded result, the situation is under control and the deviation from the exact result is always below 1%. When $\sqrt{\hat{s}} = 800$ GeV (fig. 3.3(b)) we see that some deviations from the exact result arise in the region of high p_T. For the $\mathcal{O}(p_T^4)$ result the deviations are always below 5%. Going to higher c.o.m. energies (fig. 3.3(c)) the p_T-expanded results show a divergent behavior for $p_T \gtrsim 300$ GeV: as larger values of p_T are kinematically allowed, the exact form factor cannot be reproduced accurately by the p_T expansion anymore, although the low-p_T region is always well covered. This behavior can be observed for all the other form factors, shown in app. B.3. We recall that the same behavior was also observed in the case of ZH production.

LO Cross Section We now present our results for the partonic cross section at LO. Using the projectors defined in sec. 3.3, the squared modulus of the amplitude, summed over the external polarizations and averaged over the initial ones and over color, is given by

$$< \sum_{\text{pol}} |\mathcal{A}|^2 >= \frac{1}{2}\frac{1}{2}\frac{1}{8}\frac{1}{8} 8 \frac{2 m_Z^4 G_F^2 \alpha_S^2(\mu_R)}{\pi^2} \sum_{i=1}^{18} |\mathcal{A}_i|^2 \,. \tag{3.28}$$

Then, recalling eq.(2.60), the partonic cross section at LO is expressed as

$$\hat{\sigma}^{(0)}(\hat{s}) = \frac{1}{2}\frac{m_Z^4 G_F^2}{256\pi \hat{s}^2}\left(\frac{\alpha_S(\mu_R)}{\pi}\right)^2 \int_{\hat{t}^-}^{\hat{t}^+} d\hat{t} \sum_i \left|\mathcal{A}_i^{(0)}\right|^2 \tag{3.29}$$

where $\hat{t}^{\pm} = 1/2\left[-\hat{s} + 2m_Z^2 \pm \sqrt{\hat{s}^2 - \hat{s}\; 4m_Z^2}\right]$ and we included a 1/2 factor to account for the two identical particles in the final state. In fig. 3.4 we compare the exact result (solid line) with the p_T-expanded ones (dashed lines). We notice that already the $\mathcal{O}(p_T^0)$ result has a very good agreement with the exact result for low invariant masses, with deviations below 1% in the region $M_{ZZ} \lesssim 500$ GeV (see the bottom part of fig. 3.4). By including more orders in the expansion, the accuracy of the approximation is improved and the agreement is extended to higher invariant masses. However, one can see that even the most accurate approximation starts to deviate from the exact prediction near $M_{ZZ} = 700$ GeV, although a reasonable agreement can be kept through higher invariant masses. In particular, the $\mathcal{O}(p_T^6)$ result shows deviations below 1% w.r.t. the exact result for $M_{ZZ} \lesssim 900$ GeV. More generally, if we look at the expected invariant-mass range where the p_T expansion can be trusted, we observe a very similar situation to the case of ZH production (compare figs. 3.4 and 2.5).

3.6 NLO Contribution

Having shown that the p_T expansion can provide reliable results at LO, we proceeded to compute the NLO form factors. The relevant Feynman diagrams generated by `FeynArts` amount to 75. Among these, 12 diagrams feature two-loop irreducible triangles connecting to

[2] We observed the same feature in the $A_{11}^{(0,\Box)}$ form factor.

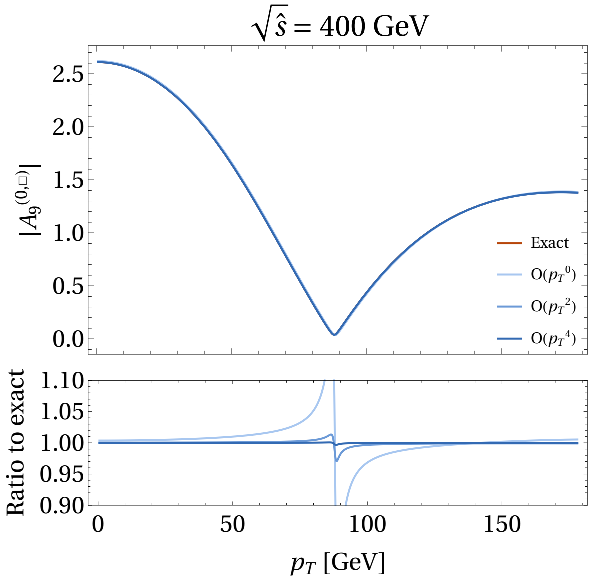

(a)

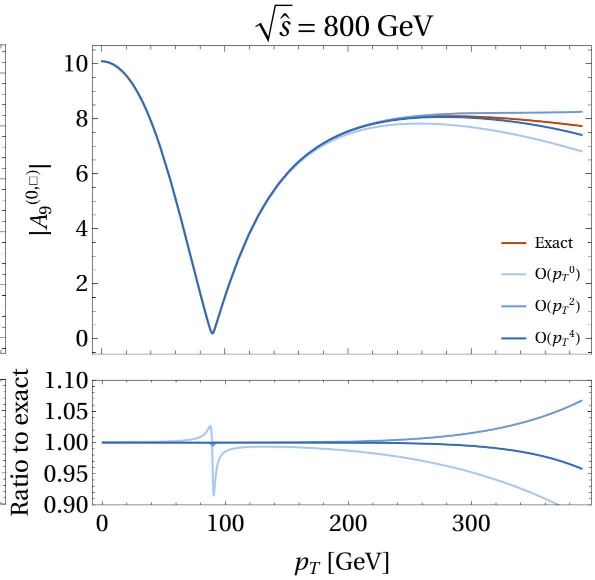

(b)

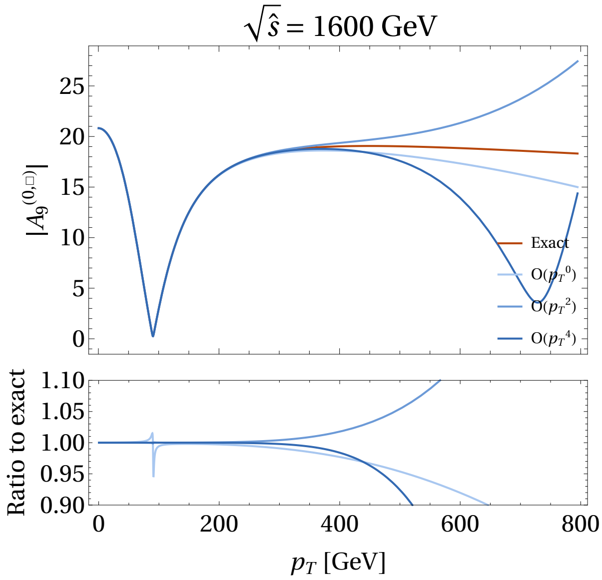

(c)

Figure 3.3: Absolute value of the $\mathcal{A}_9^{(0,\square)}$ form factor, for fixed values of $\sqrt{\hat{s}}$. The blue lines represent the first three orders of the expansion, while the brown line stands for the exact result. The bottom part of each graph shows the ratio of the various orders of the p_T expansion to the exact result.

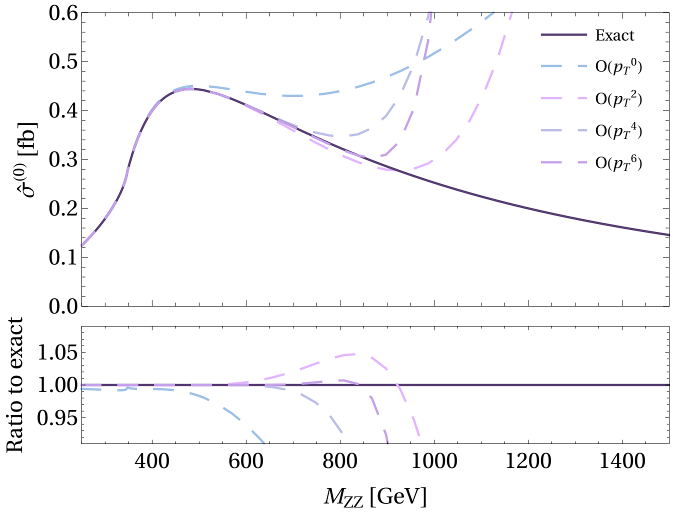

Figure 3.4: Partonic cross section at LO, as a function of the invariant mass M_{ZZ}. The exact result is shown as a dark solid line, while different orders of the p_T expansion are shown as dashed lines. In the bottom part, the ratio of each order over the exact result is shown.

the virtual Higgs boson (fig. 3.5(a,b)), 16 diagrams are double triangles involving independent loops of top and bottom quarks (fig. 3.5(c)) and 47 diagrams are two-loop boxes (fig. 3.5(d-h)). We are going to consider the separate contributions of each topology to the NLO form factors, therefore we express the latter as

$$\mathcal{A}_i^{(1)} = \mathcal{A}_i^{(1,\triangle)} + \mathcal{A}_i^{(1,\square)} + \mathcal{A}_i^{(1,\bowtie)}. \tag{3.30}$$

Triangles and Double Triangles We obtained exact analytical expressions for the $\mathcal{A}_i^{(1,\triangle)}$ form factors by adapting the results of ref. [77], and we present them in app. B.2. The calculation of the $\mathcal{A}_i^{(1,\bowtie)}$ was performed with `FeynCalc`, in our results we include the contributions from loops of bottom quarks.

Box diagrams at NLO The calculation of the $\mathcal{A}_i^{(1,\square)}$ form factors was performed along the same lines of the one for ZH production, discussed in sec. 2.8. In particular, we computed the first three terms in the p_T expansion of the form factors. The topologies analyzed were exactly the same as those related to ZH production, the only difference being the replacement of the external Higgs with a second Z boson. Therefore, we were able to rewrite all the scalar integrals in terms of the same families presented in tab. 2.2. However, we note that the technical difficulties encountered in the ZH case were aggravated by the average length of the intermediate expressions. Indeed, the increased number of Lorentz structures involved in the $gg \to ZZ$ amplitude, as well as the complexity of the projectors that can be appreciated from app. B.1, posed a serious challenge to the application of the p_T expansion approach. In general, most of the routines originally written for ZH production had to be improved to allow for the required manipulations in `Mathematica` within adequate times. To give an idea of the complexity, even with the improvements mentioned above, the very contraction of the amplitude with all 20 projectors took about one week on a desktop computer; the automatic rewriting of the scalar integrals in a form suitable for the IBP reduction within `LiteRed`

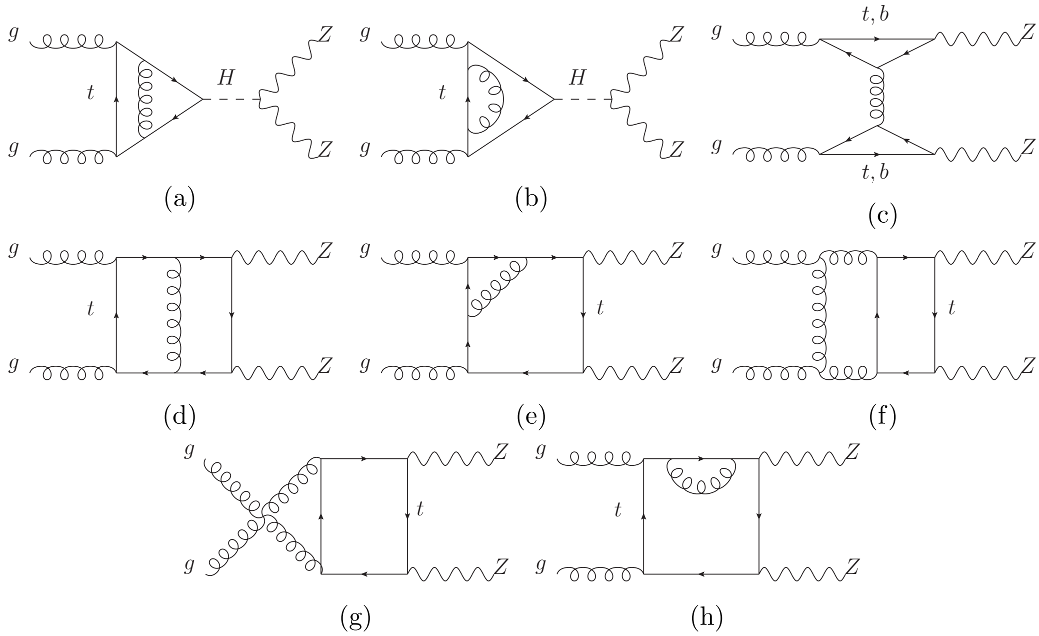

Figure 3.5: Representative Feynman diagrams contributing to the $gg \to ZZ$ amplitude at NLO. The two-loop triangle (a, b) and box (d - h) topologies are supplemented with double-triangle diagrams as in (c).

took about two weeks for all the form factors. After this step, the number of scalar integrals involved in a single form factor ranged from 250 000 to 750 000. The IBP reduction for the most complicated form factors could require more than a week to complete. Nonetheless, the size of the files for the final results turned out to be $\mathcal{O}$(100kB), which is comparable to the case of ZH production. Additionally, each form factor could ultimately be written as a linear combination of the same 52 MIs discussed in chap. 2 and presented in app. A.3.

Renormalization and IR subtraction The renormalization of the UV-divergent form factors follows the same lines of the method discussed in chap. 2. In particular, the renormalization of the top mass was performed in the OS-scheme. At the same time, the IR-divergent terms were subtracted as discussed in sec. 2.8. This procedure allows to have UV and IR finite expressions for the NLO form factors, which we discuss in the following.

3.6.1 NLO Results

In fig. 3.6 we show the results for $\mathcal{A}_9^{(1,\Box)}$ as a function of p_T, for the same c.o.m. energies as in fig. 3.3. We plot the separate contributions from the real (green lines) and imaginary (red lines) part. Although the exact result is not known, we can compare the relative behavior of the first three orders of the p_T expansion to assess its reliability at NLO. For $\sqrt{\hat{s}} = 400$ GeV (fig. 3.6(a,b)), the first three orders for both the real and imaginary parts are in very good agreement with each other for all the kinematically allowed values of p_T, and the corresponding lines are indistinguishable from each other. When higher c.o.m. energies are considered, the three lines in each plot are generally in agreement in the region $p_T \lesssim 300$ GeV, but one can see large deviations when higher values of the transverse momentum are allowed, see figs. 3.6(c-d). Therefore, the phase-space region that can be accurately covered by the p_T expansion becomes less and less important as the partonic c.o.m. energy increases. We observed this behavior for all the other p_T-expanded form factors. We note that this behavior corresponds to the one observed at LO, as well as in the case of ZH production. We are led to conclude that our expansion can accurately approximate the exact results for the $\mathcal{A}_i^{(1,\square)}$ when $p_T \lesssim 300$ GeV. Consequently, we expect that the approximation of the virtual NLO corrections will be reliable for invariant masses in the range $M_{ZZ} \lesssim 700$ GeV.

Finally, we recall that the top-quark loops discussed in this chapter are not the only contribution to $gg \to ZZ$, as also light quarks play an important role in the continuum amplitude. For this reason, in this thesis we do not to show the NLO virtual corrections to the partonic cross section from the top-quark loops, as done in chap. 2, and we defer a comprehensive study of the interplay of light and heavy quarks to future work.

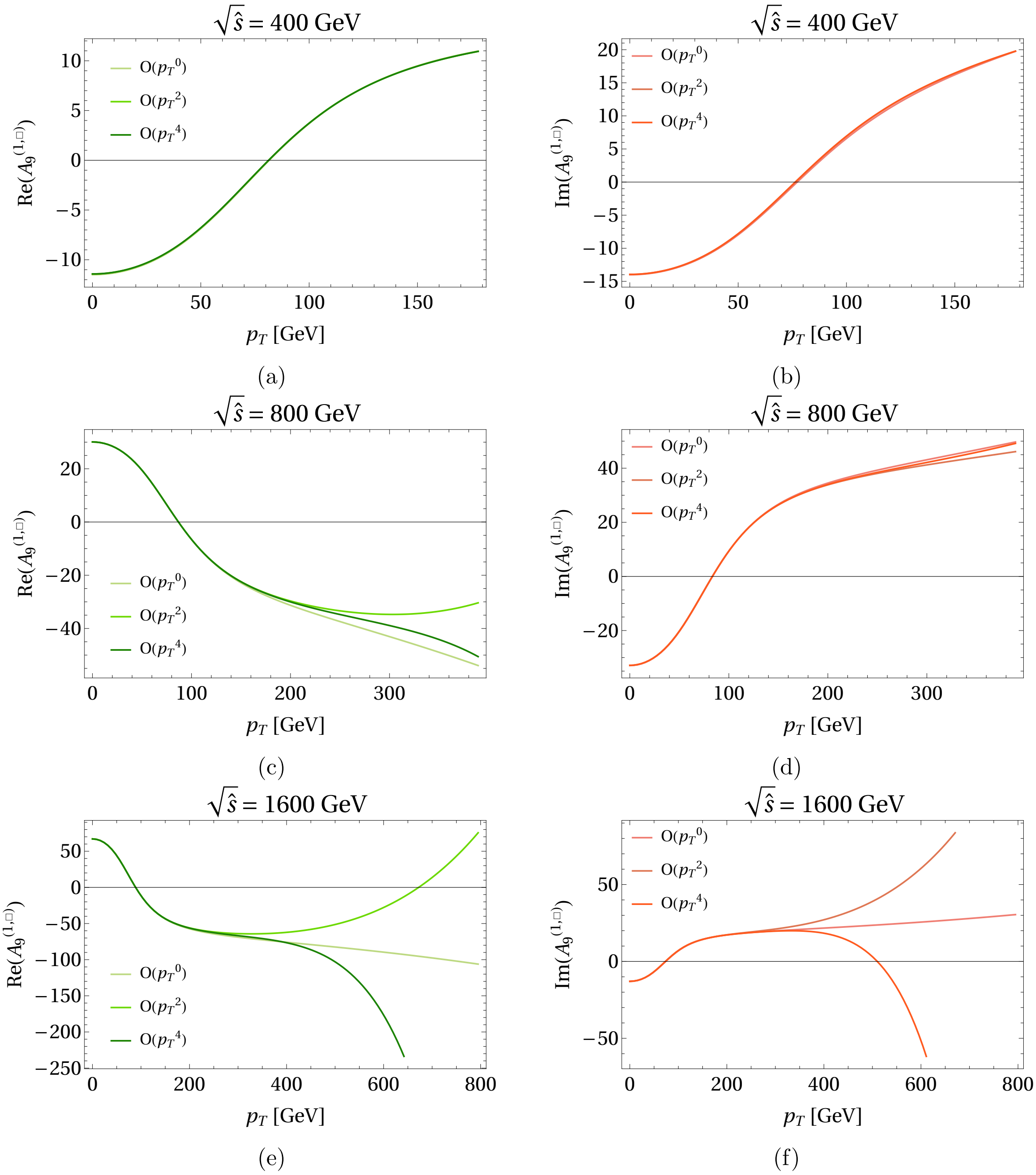

Figure 3.6: Results for the $\mathcal{A}_9^{(1,\square)}$ form factor. The first row shows the first three orders in the p_T expansion for the real (green lines - left) and imaginary (red lines - right) parts, plotted against p_T for a c.o.m. energy of $\sqrt{\hat{s}} = 400$ GeV. The second and third rows show the same quantities as the first row, for higher values of $\sqrt{\hat{s}}$.

Chapter 4

Merging the p_T and High-Energy Expansions

4.1 Introduction

In the previous chapters we presented the application of the p_T expansion to the study of gluon-initiated ZH and ZZ production. We saw that this method can provide very accurate results only in a limited region of the phase space. For $gg \to ZH$ at LHC energies, this constitutes a minor problem, since almost the totality of the hadronic cross sections comes from a region where the expansion works well. However, at future hadronic colliders the contribution to the hadronic cross section from higher invariant masses is expected to be substantial. Then, in the view of future phenomenological studies, it would be useful to investigate a way to extend the coverage of the phase space provided by the p_T expansion to regions which cannot be described by the latter. More generally, from the current development of multi-loop computational techniques, one could argue that analytical approximations like the p_T expansion may still be important in the calculation of higher-order corrections for scattering processes, and it may be convenient to use the information provided by this method in the best possible way.

An interesting possibility to improve the predictions of the p_T expansion would be to combine the latter with a different approximation, which is valid in a somewhat complementary region of the phase space. A good candidate is represented by the HE expansion. This method has been introduced for the first time in refs. [34, 123], in the calculation of top-quark effects in the two-loop corrections for double-Higgs production via gluon-fusion. Subsequently, the same approach has been used to study $gg \to ZZ$ [36] and $gg \to ZH$ [35]. In the HE expansion, the scalar integrals which constitute the form factors are expanded in the limit in which the kinematical variables $\hat{s}$ and $\hat{t}$ are large (in magnitude) compared to the masses of the particles involved.

The complementarity of the two analytical approximations will be discussed in sec. 4.4. Here, we simply illustrate the starting point of our discussion by considering the prediction of the LO partonic cross section for $gg \to ZH$, shown in fig. 4.1. The two shaded invariant-mass regions correspond to the regions where the p_T expansion (blue region) and the HE expansion (orange region) agree rather well with the exact prediction. The blue region spans the values from the kinematic ZH threshold to $M_{ZH} \lesssim 700$ GeV, while the orange region covers the range $M_{ZH} \gtrsim 800$ GeV. We also notice a relatively small blank region around $M_{ZH} = 750$

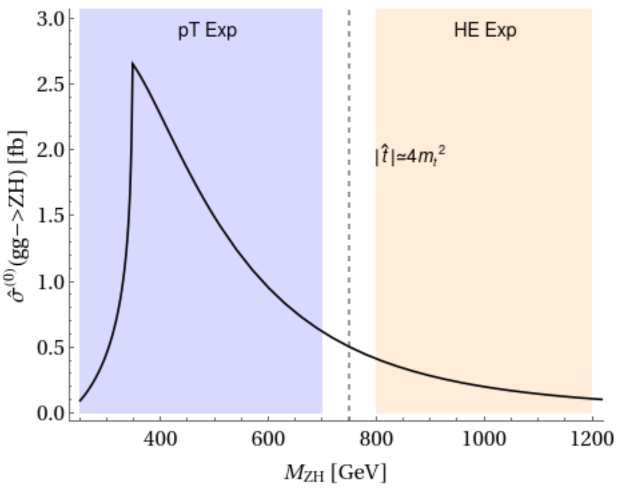

Figure 4.1: Partonic cross section for $gg \to ZH$ at LO, as a function of the invariant mass. The blue (orange) region represents the approximate range of validity of the p_T (HE) expansion. Both expansions become unreliable in the region left blank around $M_{ZH} = 750$ GeV (dashed line).

GeV (dashed line): in this region the results from both expansions are expected to diverge[1]. In the present chapter we analyze the complementarity illustrated in fig. 4.1 in greater detail, and we consider the combination of the p_T and HE expansions, with the aim of merging the two approximations into a single prediction that is accurate over the complete phase space. We will also show that the two expansions can be independently improved using the technique of Padé approximation[2]: this will be of help in finding an optimal merging procedure.

For the sake of brevity, we will give a detailed discussion only for the $gg \to ZH$ case, for which we have to study fewer form factors than for $gg \to ZZ$. Finally, we have seen that the form factors in $gg \to ZH$ depend on one additional scale w.r.t. $gg \to ZZ$, due to the different masses in the final states, so we will be able to present our merging procedure in a more general way.

In the next section we present the features of the HE expansion which are relevant for our study. In sec. 4.3 we introduce the method of Padé approximation and we discuss how it can be used to improve the convergence of both the p_T and HE expansions. Having introduced the main ingredients of our study, in sec. 4.4 we present the details of our merging procedure and we assess its reliability in reproducing the LO results. Then, in sec. 4.5 we proceed to apply the method to the approximation of the NLO virtual corrections for $gg \to ZH$.

4.2 The HE Expansion

In this section we provide the main details of the HE expansion that has been used for the study of $gg \to ZH$ in ref. [35], with the aim of making it understandable to the reader. We make clear that we did not produce the results of the HE expansion ourselves, but we used the expressions available in [124] for our study. We also get the chance to comment on the

[1] The reader can also compare fig. 2.5 in this thesis and fig. 2(a) in ref. [35].

[2] We clarify that the use of Padé approximants to improve the HE expansion has been already discussed in ref. [35].

similarities and differences between this expansion method and the p_T expansion.

With reference to the notation used in sec. 2.2, let us consider the form factor $\mathcal{A}_i$ obtained after the contraction of the full amplitude with the projector $\mathcal{P}_i^{\mu\nu\rho}$. We recall that the scalar integrals which constitute this form factor depend on five scales: $\hat{s}, \hat{t}, m_Z, m_H, m_t$. In the HE expansion, the structure of the scalar integrals is simplified in a different way compared to the p_T expansion:

1. As a first step of the method, the scalar integrals and their coefficients are Taylor-expanded in the limit of small external masses $m_Z \to 0$, $m_H \to 0$. As a consequence, m_Z and m_H don't appear in the new scalar integrals anymore, and this procedure reduces the scales upon which the integrals depend from five to three: $\hat{s}, \hat{t}$ and m_t.

2. After the Taylor expansion, the resulting integrals are decomposed along a basis of MIs by performing an IBP reduction using `FIRE` [125] and `LiteRed`. This step reduces the number of scalar integrals to be computed, but the latter still depend on $\hat{s}, \hat{t}$ and m_t.

3. Following the IBP reduction the authors of ref. [35] perform an additional step to simplify the MIs: the integrals are further expanded in the limit of a small top mass compared to the kinematical variables

$$\frac{4m_t^2}{\hat{s}} \ll 1 \qquad \frac{4m_t^2}{\hat{t}} \ll 1. \tag{4.1}$$

   This is achieved by assuming the following ansatz for the structure of the MIs in the high-energy limit

$$M(\hat{s}, \hat{t}, m_t, \varepsilon) = \sum_{ijk} B_{ijk}(\hat{s}, \hat{t}) \varepsilon^i (m_t)^j \log^k(m_t^2), \tag{4.2}$$

   where ε is the usual parameter of DR. The coefficients $B_{ijk}(\hat{s}, \hat{t})$ are reconstructed using the differential equations w.r.t. the kinematical quantities that the MIs must satisfy. The integrals resulting after this latter expansion depend only on $\hat{s}$ and $\hat{t}$, and they can be expressed in terms of Harmonic Polylogarithms (HPL)[3].

The final result of the HE expansion is then a form factor which can be written as a power series in m_t

$$\mathcal{A}_i = \sum_{n=0}^{\infty} m_t^n \; F^{(n)}(\hat{s}, \hat{t}, m_Z, m_H). \tag{4.3}$$

The $F^{(n)}(\hat{s}, \hat{t}, m_Z, m_H)$ coefficients in eq.(4.3) are themselves series in m_Z and m_H, as a consequence of the expansion in the limit of small external masses (step 1.)

$$F^{(n)} = \sum_{i=0}^{\infty} \sum_{j=0}^{\infty} m_Z^{2i} m_H^{2j} \; D_{ij}(\hat{s}, \hat{t}), \tag{4.4}$$

and the coefficients D_{ij} are linear combinations of HPLs, which may include $\log(m_t^2)$ terms. In the study of $gg \to ZH$, the authors of ref. [35] were able to obtain a result for eq.(4.3) up to and including $\mathcal{O}(m_t^{32})$ terms. They also showed that the HE expansion could reproduce the exact results both for the LO partonic cross section and for the virtual NLO corrections

[3]These special functions can be considered as a particular class of GPLs.

with good agreement for $\sqrt{\hat{s}} \gtrsim 750$ GeV, when the scattering angle is fixed to $\theta_{\text{c.o.m.}} = \pi/2$. We remark that this choice corresponds to the highest value allowed for p_T, for a given $\sqrt{\hat{s}}$.

We stress the fact that, as stated in step 2. of the method for the HE expansion, the MIs resulting from the IBP reduction depend on $\hat{s}, \hat{t}$ and m_t. This is at variance with what we observed for the p_T expansion in secs. 2.4 and 2.5; in the final result of the latter method, the MIs eventually depended only on $\hat{s}$ and m_t. The reason of the residual dependence on $\hat{t}$ (or equivalently on p_T) in the case of the HE expansion has to do with the structure of the integrals obtained after the Taylor expansion in the external masses: after the expansion, the external momentum p_3^μ appears in the denominators of the integral families found in ref. [35], therefore the MIs obtained in the IBP reduction will still depend on p_3^μ, and in particular on the scalar product $p_1 \cdot p_3 = t'$. These integrals are still hard to compute, and this complication requires the additional step of the expansion of the MIs in the high-energy limit.

We conclude this section with a comment on the validity range of the HE expansion method. Considering the assumptions in (4.1), we see that there are two conditions under which the HE expansion fails: when $\hat{s} \lesssim 4m_t^2$ and when $|\hat{t}| \lesssim 4m_t^2$. However, if we start from very high c.o.m energies and go down to the ZH production threshold, we can see that the limit in $\hat{t}$ is the first one to bring convergence issues. Indeed, if it is true that at high $\hat{s}$ the largest part of the phase space is associated to large $|\hat{t}|$, there is a value of $\hat{s}$ under which this is not the case anymore, and an important contribution comes from the region with $|\hat{t}|$ lower than or comparable to the scale set by the top mass. As shown in ref. [35], this value corresponds to $\sqrt{\hat{s}} \simeq 750$ GeV, which is higher than the limit $\sqrt{\hat{s}} \simeq 350$ GeV for an expansion in $4m_t^2/\hat{s}$. Therefore, we argue that the primary limitation of the HE expansion comes from the expansion in $4m_t^2/|\hat{t}|$, rather than in $4m_t^2/\hat{s}$. We also notice that the limit $\sqrt{\hat{s}} \simeq 750$ GeV is a lower limit for the HE expansion, while it is an upper limit for the p_T expansion (see fig. 2.5 and the related discussion).

4.3 Padè Approximants

In this section we give an introduction (see also ref. [126]) to the method of Padé approximation. This technique allows to improve the convergence of a Taylor expansion for a given function, by rearranging the expansion coefficients into a ratio of two polynomials.

Let us consider a function $f(x)$ which is expressed as a Taylor expansion in the vicinity of the regular point $x = 0$, such that only the first r terms are known

$$f(x) = \sum_{k=0}^{r-1} c_k x^k + \mathcal{O}(x^r) \tag{4.5}$$

and we are then neglecting $\mathcal{O}(x^r)$ terms. Then a Padé approximant of $f(x)$ is defined as the rational fraction

$$[m, n] = \frac{p_0 + p_1 x + \cdots + p_m x^m}{q_0 + q_1 x + \cdots + q_n x^n} \tag{4.6}$$

which has a Taylor expansion that reproduces exactly the first r terms in the r.h.s. of eq.(4.5),

$$\frac{p_0 + p_1 x + \cdots + p_m x^m}{q_0 + q_1 x + \cdots + q_n x^n} = \sum_{k=0}^{r-1} c_k x^k + \mathcal{O}(x^{m+n+1}). \tag{4.7}$$

It is customary to fix the arbitrary normalization in (4.6) by choosing $q_0 = 1$. To compute the set of unknown p_i, q_j necessary to construct an approximant, one can Taylor expand eq.(4.6) and equate the result to the sum of the first r terms in the r.h.s. of eq.(4.5). This provides a system of $m+n+1$ linear equations in the p_i, q_j, which can be solved under the condition $m+n+1 \leq r$.

Typically, the approximation of the exact function $f(x)$ provided by the Padé is quite better than the one provided by the Taylor expansion, suggesting that the information on $f(x)$ associated to the Taylor expansion can be used in a more efficient way. In particular, approximants (4.6) such that $m = n$ (denoted as *diagonal* Padé approximants) are known to bring the best improvement in convergence. We can then try to improve the convergence of the p_T-expanded form factors obtained in the previous chapters by constructing the associated Padé approximants. We will see that this does not guarantee an optimal result, and in the next section we will show that the complementarity in phase space of the HE expansion will be important. Therefore, in the following subsection we discuss the procedure for the construction of the Padé approximants starting both from the results of the p_T expansion (which will be denoted as *p_T-Padé*) and from those of the HE expansion (*HE-Padé*). For simplicity, in this thesis we will study only diagonal $[n, n]$ approximants.

Padé Approximants from the p_T expansion We recall here for convenience that the final expression of a form factor obtained using the p_T expansion is (see eq.(2.47))

$$\mathcal{A}_i = \mathcal{N} \sum_{N=0}^{2} \sum_{i+j+k=N} c_{ijk} (p_T^2)^i (m_Z^2)^j (\Delta_m)^k. \tag{4.8}$$

In order to define a procedure for the construction of the p_T-Padé, we recall that the results above could be obtained by assuming the same scaling x for the *small* parameters p_T^2, m_Z^2 and Δ_m. If we make x explicit again in eq.(4.8) we get

$$\begin{aligned} \mathcal{A}_i &= \mathcal{N} \sum_{N=0}^{2} x^N \sum_{i+j+k=N} c_{ijk} (p_T^2)^i (m_Z^2)^j (\Delta_m)^k \\ &= \mathcal{N} \sum_{N=0}^{2} x^N c_N \end{aligned} \tag{4.9}$$

and we are able to see a given form factor as a power series near $x = 0$, where the c_N coefficients include the small parameters, in addition to the linear combinations of MIs . Now we can use the c_N coefficients to construct Padé approximants $[n, n](x)$, in which we will set $x = 1$. Since not more than the first three c_N are known at NLO from the results in chap. 2, the only diagonal Padé that we can construct is a [1,1] approximant given by

$$[1, 1](x) = \mathcal{N} \frac{p_0 + p_1 x}{1 + q_1 x} \tag{4.10}$$

with

$$p_0 = c_0 \qquad p_1 = c_1 - \frac{c_0 c_2}{c_1} \qquad q_1 = -\frac{c_2}{c_1}. \tag{4.11}$$

We notice that even if $\mathcal{N}$ in eq.(4.8) may depend on the expansion parameters (and therefore on x), the method for the construction of the Padé approximant is not affected by an overall normalization.

Padé Approximants from the HE expansion The starting point for the construction of the HE-Padé are the form factors as expressed in eq.(4.3). We know that the scale set by the top mass is the one that truly limits the validity of the HE expansion. Therefore, in analogy to the p_T-Padé, we will associate the scaling parameter x to m_t^2. There is, however, a subtlety related to the presence in (4.3) of some terms involving odd powers of m_t. In order to address this issue, we follow the procedure discussed in ref. [35] and before constructing the Padé approximants we arrange the terms in eq.(4.3) as

$$\begin{aligned} \mathcal{A}_i &= F^{(0)} + \sum_{l=1}^{L} (F^{(2l-1)} m_t^{2l-1} + F^{(2l)} m_t^{2l}) x^l \\ &= \sum_{l=0}^{L} d_l x^l, \end{aligned} \tag{4.12}$$

where we note that terms associated to odd powers of m_t are grouped with those with the next even power of m_t. Starting from eq.(4.12), and knowing that L can be as large as 16 in ref. [35], we can then build $[n, n]$ Padé approximants with $n \leq 8$.

We want to comment here on the practical way in which the Padé used in this thesis are constructed compared to ref. [35] (see also ref. [36]). The approximants in that reference were obtained point-by-point in phase space, by first obtaining a numerical result for the d_l coefficients in eq.(4.12), then building the HE-Padé using x as variable and solving the linear equations for the coefficients *numerically*, eventually setting $x = 1$. We used a simpler approach: first, we constructed the general expressions of a given $[n, n](x)$ Padé by solving the systems of linear equations *symbolically* in `Mathematica`; when a numerical evaluation of the Padé is needed, we evaluate the c_N (for the p_T-Padé) and d_l (for the HE-Padé) coefficients separately for a specific value of the phase space point; finally, we replace these numerical values in the implicit expressions for the Padé approximants, setting $x = 1$ at the end of the evaluation. This method allows us to solve the required linear systems just once for a given $[n, n]$ Padé, and we also manage to have flexible analytical expressions. However, in the case of the HE-Padé, we must point out that solving the linear equations for the $[n, n]$ approximants with $n \geq 7$ becomes computationally demanding. In fact, we will show that the improvement in the convergence provided by the $[7, 7]$ and $[8, 8]$ Padé is not really necessary for our purposes.

4.4 Merging Method

In the previous section we have discussed the method of Padé approximation as a way to improve the convergence of the analytical approximations represented by the p_T and HE expansions. Now we are going to devise a strategy for obtaining an accurate prediction of the exact results over the complete phase space, using Padé approximants constructed from both expansions. In order to do so, we must first discuss in more detail the complementarity of the p_T and HE expansions mentioned in the introduction. In the following considerations on the kinematical limits of the expansions, we will use the same definitions introduced in chap. 2. Also, as discussed previously, for our purposes it is sufficient to discuss only the forward contribution to the cross section. Then, in the following we will always assume that $|\hat{t}| < |\hat{u}|$ and that

$$\hat{t} = -\frac{1}{2}\left(\hat{s} - m_Z^2 - m_H^2 - \sqrt{\lambda(\hat{s}, m_Z^2, m_H^2) - 4\hat{s}\, p_T^2}\right). \tag{4.13}$$

In chap. 2 we noticed that, for any fixed value of $\hat{s}$, the p_T expansion provides an accurate approximation of the exact results when $p_T^2 \lesssim 4m_t^2$, while in sec. 4.2 we saw that the HE expansion is accurate for $|\hat{t}| \gtrsim 4m_t^2$. These two limits are however interrelated, as we can always trade p_T with $\hat{t}$ via the relation

$$p_T^2 = -\hat{t} + \frac{\hat{t}(m_H^2 + m_Z^2 - \hat{t}) - m_H^2 m_Z^2}{\hat{s}} \tag{4.14}$$

and notice that for sufficiently high $\hat{s}$ the quantities p_T^2 and $|\hat{t}|$ are basically interchangeable. Thus, we can state that the validity of both the p_T and HE expansions is limited to values of $|\hat{t}|$ which are not too close to the scale set by the top mass, in particular

$$\begin{aligned} |\hat{t}| &\lesssim 4m_t^2 \qquad (p_T \text{ expansion}) \\ |\hat{t}| &\gtrsim 4m_t^2 \qquad (\text{HE expansion}). \end{aligned} \tag{4.15}$$

The origin of the limits in (4.15) can be better understood by inspecting the so-called *natural variable* x_t, upon which the GPLs used to express the scalar integrals typically depend,

$$x_t = \frac{1 - \sqrt{1 - \frac{4m_t^2}{\hat{t}}}}{1 + \sqrt{1 - \frac{4m_t^2}{\hat{t}}}}. \tag{4.16}$$

One can see that x_t admits a Taylor expansion both for $|\hat{t}| \ll 4m_t^2$, which we can relate to the p_T expansion, and for $|\hat{t}| \gg 4m_t^2$, corresponding to the HE expansion.

Having clarified in (4.15) what we mean by complementarity of the two expansions, we can now discuss a way to combine the results of the the p_T and HE expansion. We begin by noting that, for a fixed value of $\hat{s}$, there exists a maximum value of $|\hat{t}|$ allowed by the (forward) kinematics. This value, which we denote as $|\hat{t}|_{\max}$, is related to the maximum value allowed[4] for p_T, namely $p_T = 1/2\sqrt{\lambda(\hat{s}, m_Z^2, m_H^2)/\hat{s}}$, and corresponds to

$$|\hat{t}|_{\max} = \frac{1}{2}(\hat{s} - m_Z^2 - m_H^2). \tag{4.17}$$

If we now consider the whole set of partonic c.o.m. energies, we note that there is a range of $\hat{s}$-values such that $|\hat{t}|_{\max}$ is always lower than $4m_t^2$: in this range, the p_T expansion alone provides an accurate approximation of the exact result for any phase-space point $(\hat{s}, \hat{t})$, while the accuracy of the HE expansion is always poor and therefore the approximation provided by the latter cannot be trusted. On the other hand, we can define a critical value $\hat{s}_c$ given by

$$\hat{s}_c = 8m_t^2 + m_Z^2 + m_H^2, \tag{4.18}$$

such that when $\hat{s} \geq \hat{s}_c$ one has $|\hat{t}|_{\max} \geq 4m_t^2$. Then, when $\hat{s} \geq \hat{s}_c$, we understand that, in order to cover all the relevant phase-space points (i.e. $|\hat{t}| \lesseqgtr 4m_t^2$) the HE expansion must be considered in conjunction with the p_T expansion. For $gg \to ZH$ we find that $\sqrt{\hat{s}_c} \simeq 510$ GeV.

At this point, we could naively try to combine the results of the p_T and HE expansions into a single prediction, which uses the former expansion to describe the region $|\hat{t}| < 4m_t^2$ and the latter for $|\hat{t}| > 4m_t^2$. Unfortunately, both expansions diverge rather quickly near

[4] Assuming a real-valued $\hat{t}$.

$|\hat{t}| = 4m_t^2$ (see e.g. fig. 4.2(a)). In particular, a straightforward combination of the p_T-expanded results and the HE-expanded ones does not guarantee an accurate description of the $\hat{t}$-region corresponding roughly to $|\hat{t}|/(4m_t^2) \in [0.5, 1.5]$. We point out that this behavior is not expected to change substantially when higher orders in both the expansions are computed.

In order to address the loss in accuracy for $|\hat{t}|/(4m_t^2) \in [0.5, 1.5]$, we can use the p_T and HE Padé approximants introduced in the previous section. In the following we are going to define a simple procedure for the merging of the two expansions, and we are going to assess its reliability using the exact LO results as a benchmark.

Choice of HE-Padé and matching point As observed before, we can only use a [1,1] p_T-Padé to improve the convergence of the simple p_T expansion. Concerning the HE expansion, we would like to use a unique $[n, n]$ HE-Padé among the several ones that can be built from the results of ref. [35]: we consider an optimal choice to be a HE-Padé which is accurate enough to reproduce the exact results in the region $|\hat{t}|/(4m_t^2) \in [0.5, 1.5]$ for every $\hat{s} \geq \hat{s}_c$, and which is not too demanding from a computational point of view. To investigate this possibilities, we constructed several HE-Padé and studied how well they could reproduce the exact results for the LO box form factors. As in chap. 2, we are going to focus our discussion on $\mathcal{A}_1^{(0,\Box)}$. In order to express the results of ref. [35] in terms of our form factors we use the conversion formulae in app. A.1. Fig. 4.2(a) shows the absolute value of the form factor as a function of the ratio $|\hat{t}|/(4m_t^2)$, for fixed $\sqrt{\hat{s}} = 2$ TeV. For such a high c.o.m. energy, the HE energy expansion is expected to be very accurate in reproducing the exact result. Indeed, we see that the simple HE expansion (orange solid line) and the [2,2], [4,4] and [6,6] HE-Padé[5] (green, purple and yellow dashed lines, respectively) agree very well with each other and with the exact result from $|\hat{t}|_{\max}/(4m_t^2) \simeq 17$ (not shown in the figure) down to $|\hat{t}|/(4m_t^2) \simeq 1.2$. In the vicinity of the latter point, the simple HE expansion begins to diverge, while the HE-Padé are still in excellent agreement with the exact result. In particular, the [4,4] and [6,6] HE-Padé provide accurate results also in a region where the simple p_T expansion, included as a reference, works well.

When values of $\hat{s}$ closer to $\hat{s}_c$ are considered, the level of accuracy shown for $\sqrt{\hat{s}} = 2$ TeV is partially lost. In fig. 4.2(b) we show the same predictions as in fig. 4.2(a) but for $\sqrt{\hat{s}} = 600$ GeV. First, we point out that in this case the simple HE expansion gives very inaccurate results, and the corresponding line is not shown in the plot. This is understandable, as for $\sqrt{\hat{s}} = 600$ GeV one has $|\hat{t}|_{\max}/(4m_t^2) = 1.4$, and basically there are no $\hat{t}$ values allowed for which the HE expansion is sensible. Also the [2,2] HE-Padé is definitely off w.r.t. the exact prediction, suggesting that using only the first five orders of the HE expansion to build an approximant does not improve the convergence enough. However, the [4,4] and [6,6] HE-Padé are still in good agreement with each other and with the full result, down to $|\hat{t}|/(4m_t^2) = 0.6$. Then, it is clear that a $[n, n]$ HE-Padé with $n \geq 4$ can be used for our purposes. We also point out that using a [6,6] instead of a [7,7] HE-Padé requires substantially less evaluating time, while the difference in evaluating time between a [4,4] and a [6,6] is not dramatic. If we take into account that at NLO the ignorance on the exact prediction will introduce an additional source of uncertainty, we conclude that using a [6,6] HE-Padé is a good conservative choice to improve the convergence of the HE expansion in the vicinity of $|\hat{t}| = 4m_t^2$. Finally, we need to make a convenient choice for the value of $|\hat{t}|$ where we switch from using the results of the p_T expansion to the ones of the HE expansion in our prediction: a natural choice is precisely

[5] In the plots in fig. 4.2 we show only these HE-Padé for clarity. However, we studied the behavior of all the $[n, n]$ Padé with $n \leq 7$.

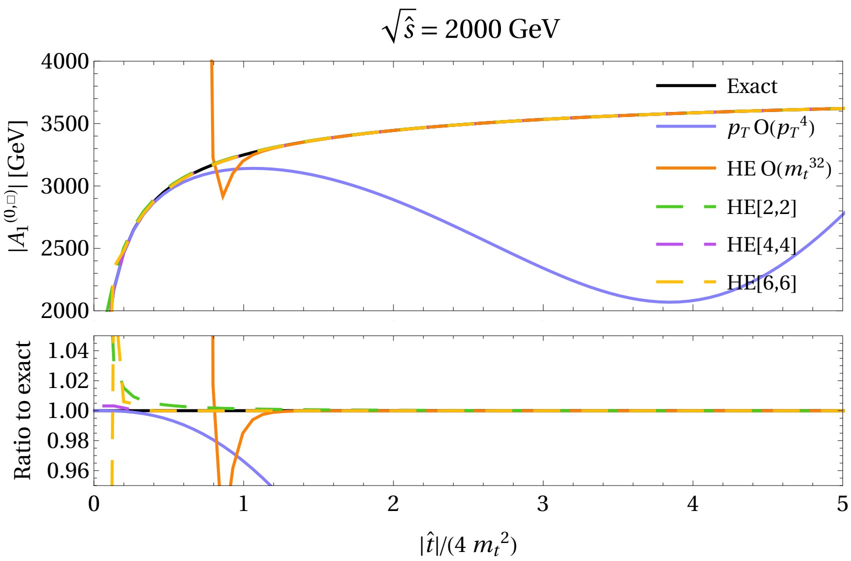

(a)

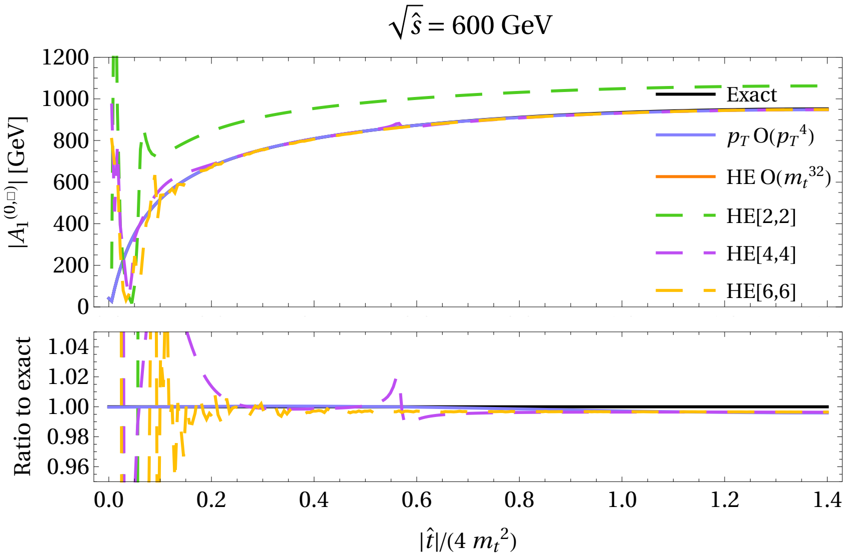

(b)

Figure 4.2: Absolute value of the $\mathcal{A}_1^{(0,\square)}$ form factor as defined in eq.(2.49), as a function of the ratio $|\hat{t}|/(4m_t^2)$ for $\sqrt{\hat{s}} = 2$ TeV (a) and for $\sqrt{\hat{s}} = 600$ GeV (b). The black solid line shows the exact result, the blue and orange solid lines show the simple p_T-expanded and HE-expanded results, respectively; the dashed lines represent the $[2,2]$ (green), [4,4] (purple) and [6,6] (yellow) HE-Padé. The bottom part of each plot shows the ratios of the various approximations to the exact result.

the value $|\hat{t}| = 4m_t^2$.

Merging Method We can now present our method for obtaining a prediction of the exact result for a form factor in the whole phase space, which will be used both at LO and NLO. When evaluating a form factor in a given region of the phase space

1. if $\hat{s} < \hat{s}_c$ the [1,1] p_T-Padé is used for every allowed value of $\hat{t}$,

2. if $\hat{s} \geq \hat{s}_c$ the [1,1] p_T-Padé is used for $0 < |\hat{t}| < 4m_t^2$ while the [6,6] HE-Padé is used for $4m_t^2 \leq |\hat{t}| \leq |\hat{t}|_{\max}$.

We remark that in our method we also use the [1,1] p_T-Padé as an additional improvement in the convergence of the p_T expansion. In fact, the [1,1] p_T-Padé is expected to cover the region $|\hat{t}|/(4m_t^2) \in [0.5, 1]$ more accurately than the [6,6] HE-Padé. Furthermore, using the two kinds of Padé allows us to cross check their reliability.

We recall that also in ref. [35] Padé approximants were used as way to improve the accuracy of the HE expansion. In that reference, the authors used a procedure (described in ref. [36]) to estimate the uncertainty associated to the Padé-improved results. This procedure is motivated by the need of extending the accuracy of the HE expansion to the region $\hat{s} \leq \hat{s}_c$. We have seen, however, that this very region of the phase space is covered by the predictions of the p_T expansion and its improvement using the [1,1] Padé. Therefore, we believe that a refined characterization of the uncertainty of our merging method is not necessary.

Merging at LO After we have specified which results we are going to use and the method to combine them, we can discuss how well the exact LO results are reproduced by our approach. In fig. 4.3 we show the results obtained for $\mathcal{A}_1^{(0,\square)}$ for two points in the $\hat{s}$-region where the simple p_T expansion does not provide accurate results, namely $\sqrt{\hat{s}} = 800$ GeV and $\sqrt{\hat{s}} = 1600$ GeV (see also fig. 2.4). As already observed in fig. 4.2, the simple p_T (solid blue line) and HE (solid orange line) expansions begin to lose accuracy in the region of $|\hat{t}|/(4m_t^2) \in [0.5, 1.5]$, leaving a gap in the coverage of the exact prediction (solid black line). The situation described above changes if we include the Padé approximants. In fig. 4.3(a) we see that for $\sqrt{\hat{s}} = 800$ GeV the [1,1] p_T-Padé (dashed light-blue line) can reproduce the exact result remarkably well for all the values of $|\hat{t}|$ allowed by the kinematics, and the ratio to the full result, shown in the bottom part of fig. 4.3(a), remains within the range [0.99, 1].

In fig. 4.3(b) we consider the case $\sqrt{\hat{s}} = 1600$ GeV and we find the same behavior as for lower energies. In particular, we see that the [6,6] HE-Padé agrees very well with the exact result down to $|\hat{t}|/(4m_t^2) = 0.5$, a value which is well covered by the simple p_T expansion and by the [1,1] p_T-Padé. We point out that the importance of the region $|\hat{t}| > (4m_t^2)$ over the phase space grows with the value of $\hat{s}$.

In fig. 4.4 we summarize our findings for all the form factors by showing the prediction for the partonic cross section at LO. We see that for the region $M_{ZH} \gtrsim 700$ GeV, in which the simple p_T expansion (dashed blue line) diverges, the prediction from the merging of the p_T- and HE-Padé approximants (dashed green line) is in excellent agreement with the full result (solid line) even for very high invariant masses. In particular, from the bottom part we can see that the deviation of the merged prediction from the exact one is always comparable to or below 1%.

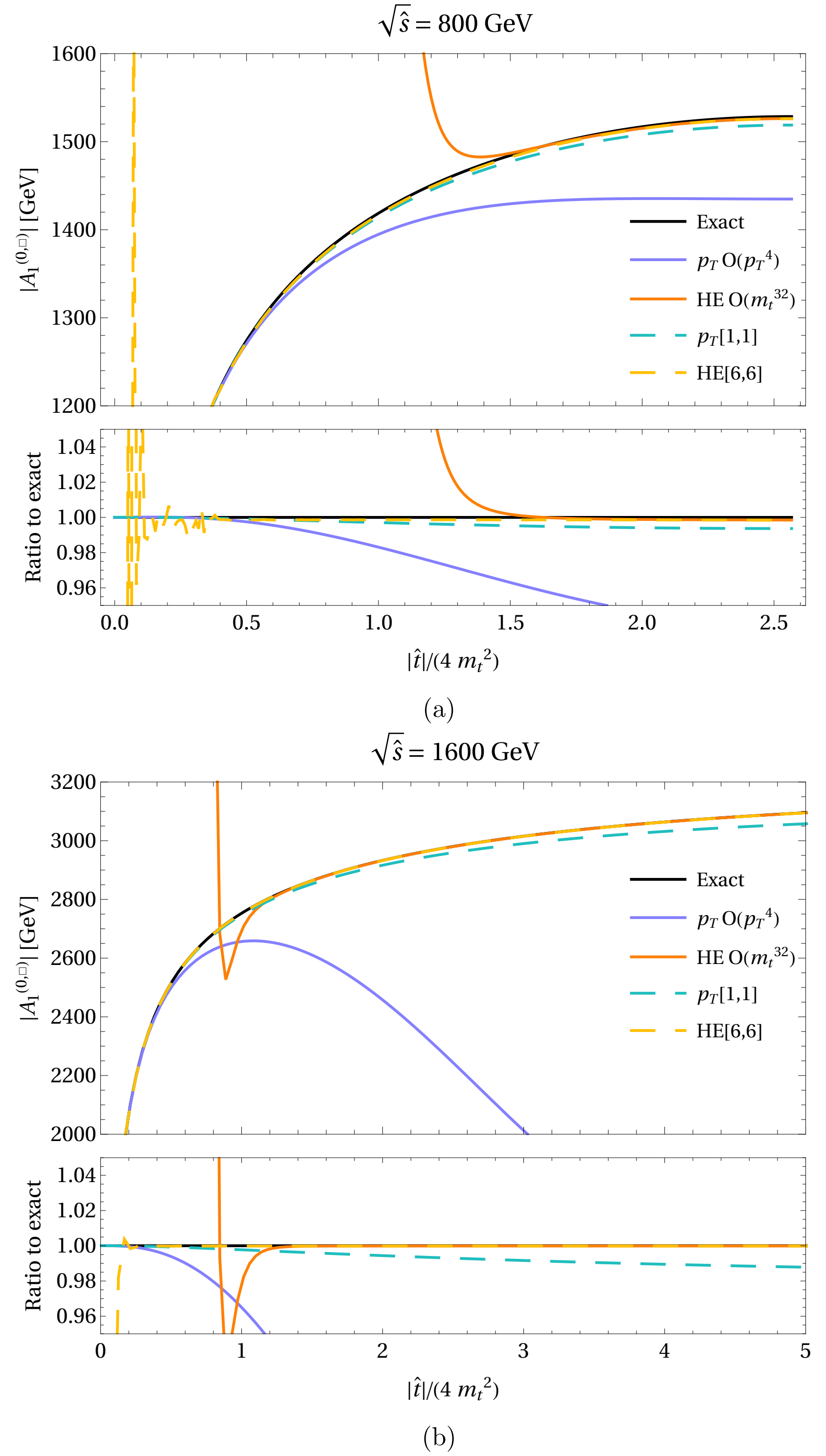

Figure 4.3: Absolute value of the $\mathcal{A}_1^{(0,\Box)}$ form factor as defined in eq.(2.49), for $\sqrt{\hat{s}} = 800$ GeV (a) and for $\sqrt{\hat{s}} = 1600$ GeV (b): the black solid line shows the exact result, the blue and orange solid lines show the simple p_T-expanded and HE-expanded results, respectively; the light-blue and yellow dashed lines represent the $[1,1]p_T$-Padé and the $[6,6]$ HE-Padé, respectively. The bottom part of each plot shows the ratios of the various approximations to the exact result.

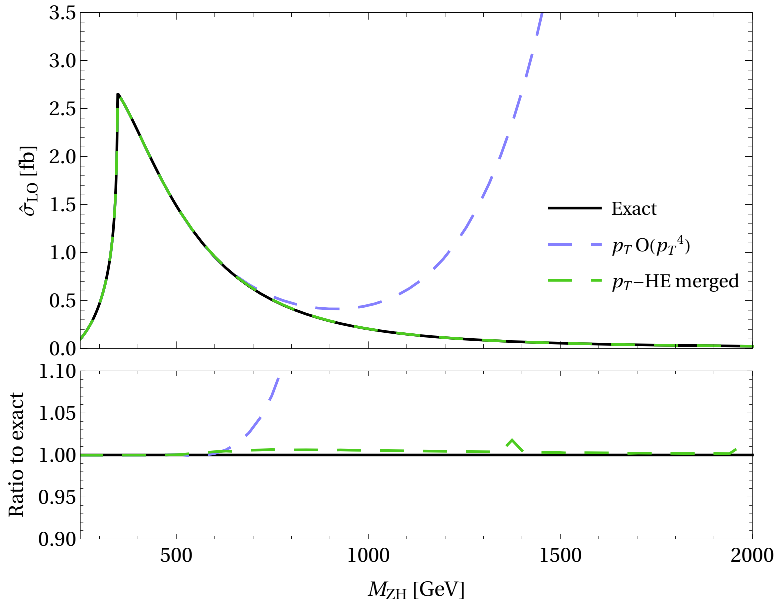

Figure 4.4: Predictions for the LO partonic cross section of $gg \to ZH$, as a function of the invariant mass: the solid line represents the exact result; the blue dashed line represents the simple p_T expansion up to $\mathcal{O}(p_T^4)$ terms,corresponding to the approach of chap. 2; the green dashed line represents the merging of the results of the p_T and HE expansions. The bottom part shows the ratios of the different results to the exact one.

4.5 Merging at NLO

The level of accuracy of the merged prediction that we observed at LO leads us to study the applicability of the merging method previously defined to the NLO virtual corrections for $gg \to ZH$. We recall that exact analytical results are available for the two-loop triangle and double triangle form factors, $\mathcal{A}_i^{(1,\triangle)}$ and $\mathcal{A}_i^{(1,\bowtie)}$. In the following we will then consider only the two-loop box form factors, and we will discuss the degree to which the Padé approximants can improve the convergence of the p_T and HE expansions at NLO. Since we don't have an exact NLO result to compare with, we first checked that the choice of a [6,6] HE-Padé, that was motivated in the previous section, is reliable also at NLO. For every form factor, we computed $[n, n]$ HE-Padé approximants with $n \leq 7$ and verified that, for a fixed $\hat{s} \geq \hat{s}_c$ the [6,6] Padé agreed with the [7,7] Padé from $|\hat{t}|_{\max}$ down to $|\hat{t}|/(4m_t^2) \simeq 0.5$.

Then, we compared the predictions from the [1,1] p_T-Padé and from the [6,6] HE-Padé to the ones of the corresponding Taylor expansions. In fig. 4.5 we show the results obtained for $\mathcal{A}_1^{(1,\square)}$ for the same $\hat{s}$-values that we showed at LO in fig. 4.3. In both plots we see that the [1,1] p_T-Padé agrees well with the simple p_T expansion up to $|\hat{t}|/(4m_t^2) \simeq 0.5$, but with increasing $|\hat{t}|$ the simple expansion diverges, as expected. On the other hand, one can see that for high energies (fig. 4.5(b)) the [6,6] HE-Padé agrees well with the simple HE expansion from $|\hat{t}|_{\max}/(4m_t^2)$ down to about 1, where the simple HE-expansion diverges. We notice however that for moderate energies like $\sqrt{\hat{s}} = 800$ GeV (fig. 4.5(a)) the simple HE-expansion is slightly off w.r.t. the [6,6] HE-Padé, even in the region $|\hat{t}| \gtrsim 4m_t^2$. From the comparison with the LO result discussed in the previous section, we understand that, between the [6,6] HE-Padé and the simple HE expansion, the [6,6] HE-Padé is the most accurate quantity, and the one to be trusted in our prediction.

Finally, we point out that in the region where the two simple expansions diverge, the p_T-Padé and the HE-Padé are always in good agreement. This can be observed from the bottom parts of fig. 4.5, where we show the relative difference between the two Padé. The relative difference is defined as

$$\Delta_{\text{Padé}} = \frac{|[1,1]_{p_T} - [6,6]_{\text{HE}}|}{|[1,1]_{p_T} + [6,6]_{\text{HE}}|/2} \tag{4.19}$$

and we remark that $\Delta_{\text{Padé}}$ never exceeds a few percents. To summarize, for both the p_T and HE Padé-improved predictions we observed the same behavior as for the LO case. We then expect that the results of the merging method can provide a comparable level of accuracy in the approximation of the unknown exact results. A promising feature, which can be appreciated from fig. 4.6(discussed in the next subsection), is that the merged result is convergent for any value of the invariant-mass.

4.5.1 Change of Renormalization Scheme

To demonstrate the flexibility of the results obtained with the merging procedure, we evaluated the finite virtual corrections to the cross section, $\Delta\sigma_{\text{virt}}$, defined in eq.(2.70), using a different renormalization scheme for the top mass, namely the modified minimal subtraction scheme ($\overline{\text{MS}}$). We recall that the NLO form factors were obtained in chap. 2 using the on-shell (OS) scheme for the top mass renormalization. In the $\overline{\text{MS}}$ scheme, the renormalization counterterms are defined by including only the UV-divergent parts. In order to express a given NLO form factor in the $\overline{\text{MS}}$ scheme, starting from the OS result $\mathcal{A}_i^{(1,\text{OS})}$ obtained in eq.(2.65), one must remove the finite parts associated to the counterterm δ_{OS}. This can be achieved as follows

$$\mathcal{A}_i^{(1,\overline{\text{MS}})} = \mathcal{A}_i^{(1,\text{OS})} - \Delta_{\overline{\text{MS}}}, \tag{4.20}$$

with

$$\Delta_{\overline{\text{MS}}} = 2m_t^2 \left(\frac{\partial}{\partial m_t^2}\mathcal{A}_i^{(0)}\right)\left[-\frac{C_F}{4}\left(4 - 3\log\left(\frac{m_t^2}{\mu_R^2}\right)\right)\right], \tag{4.21}$$

and where $\mathcal{A}_i^{(0)}$ is the LO form factor. In our merging method, we use the p_T-expanded (HE-expanded) result for $\mathcal{A}_i^{(0)}$ to obtain $\Delta_{\overline{\text{MS}}}$, we subtract the latter from the p_T-expanded (HE-expanded) $\mathcal{A}_i^{(1,\text{OS})}$ and we construct a p_T-Padé (HE-Padé) from the new result. From this point on, the merging procedure is the same as in the OS case.

In evaluating the $\overline{\text{MS}}$ results, the dependence of the top mass on the renormalization scale must be consistently taken into account. The results of ref. [127] are used to obtain the μ_R-dependent $\overline{\text{MS}}$ mass from the μ_R-independent OS mass. In fig. 4.6 we compare the OS result with several choices for μ_R in the $\overline{\text{MS}}$ results: $M_{ZH}/2$, $2M_{ZH}$ and the on-shell mass $m_t = 173.21$ GeV. From fig. 4.6 there are visible differences in the results w.r.t. the choice of renormalization scheme, and the height and the position of the peak in $\Delta\sigma_{\text{virt}}$ are clearly modified by the choice of the renormalization scale within the $\overline{\text{MS}}$ scheme. This variability may represent an additional source of systematic uncertainty to be considered in theory predictions. However, these effects may be partly compensated when $\Delta\sigma_{\text{virt}}$ is added to the LO partonic cross section evaluated using the $\overline{\text{MS}}$ top mass. More generally, a sensible assessment of this uncertainty may be achieved only with the inclusion of the real emission contribution, the calculation of which is beyond the scope of this thesis.

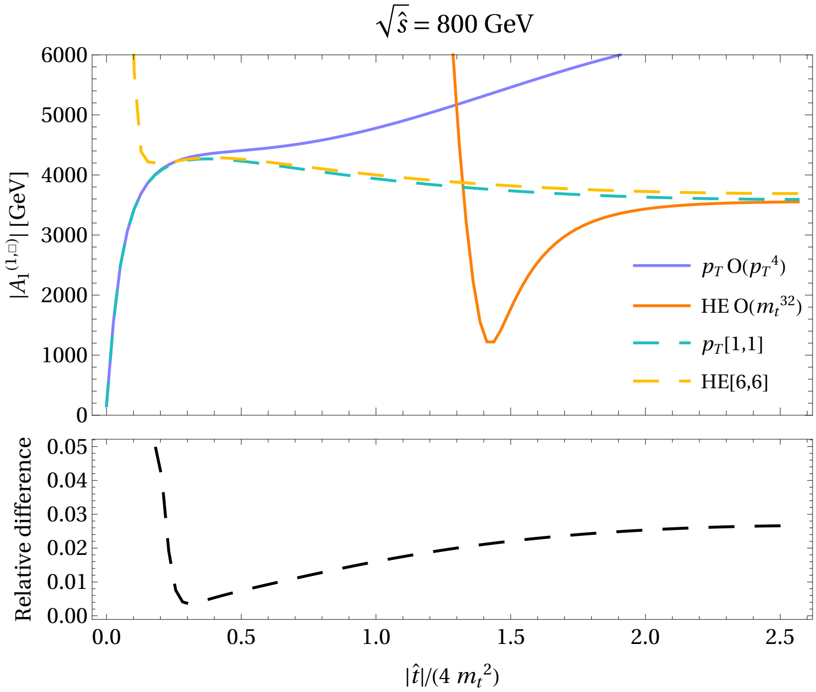

(a)

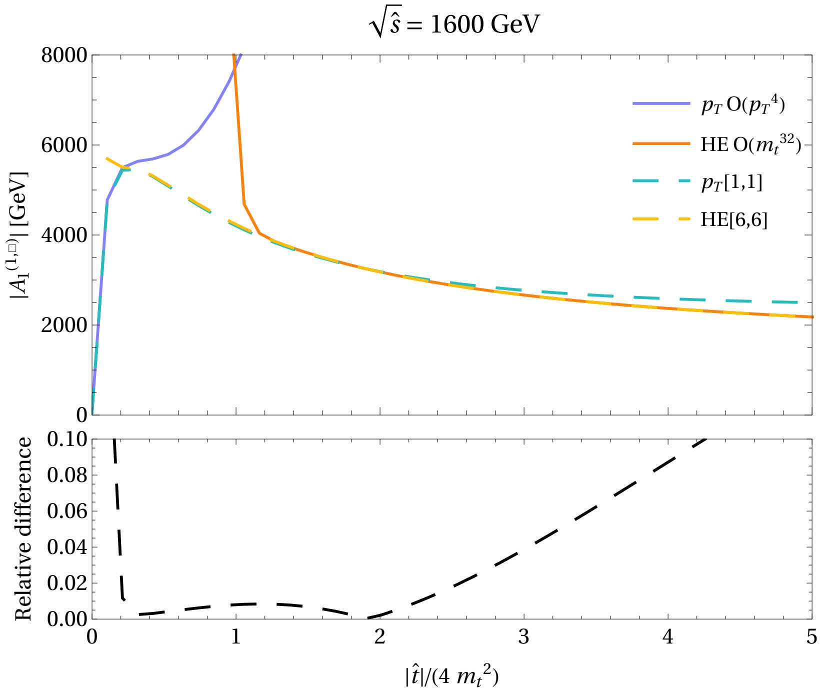

(b)

Figure 4.5: Absolute value of the $\mathcal{A}_1^{(1,\square)}$ form factor as a function of the ratio $|\hat{t}|/(4m_t^2)$, for $\sqrt{\hat{s}} = 800$ GeV (a) and for $\sqrt{\hat{s}} = 1600$ GeV (b): the blue and orange solid lines show the simple p_T-expanded and HE-expanded results, respectively; the light-blue and yellow dashed lines represent the [1,1] p_T-Padé and the $[6,6]$ HE-Padé, respectively. The bottom part of each plot shows the relative difference between the $[1,1]p_T$-Padé and the $[6,6]$ HE-Padé, as defined in eq.(4.19).

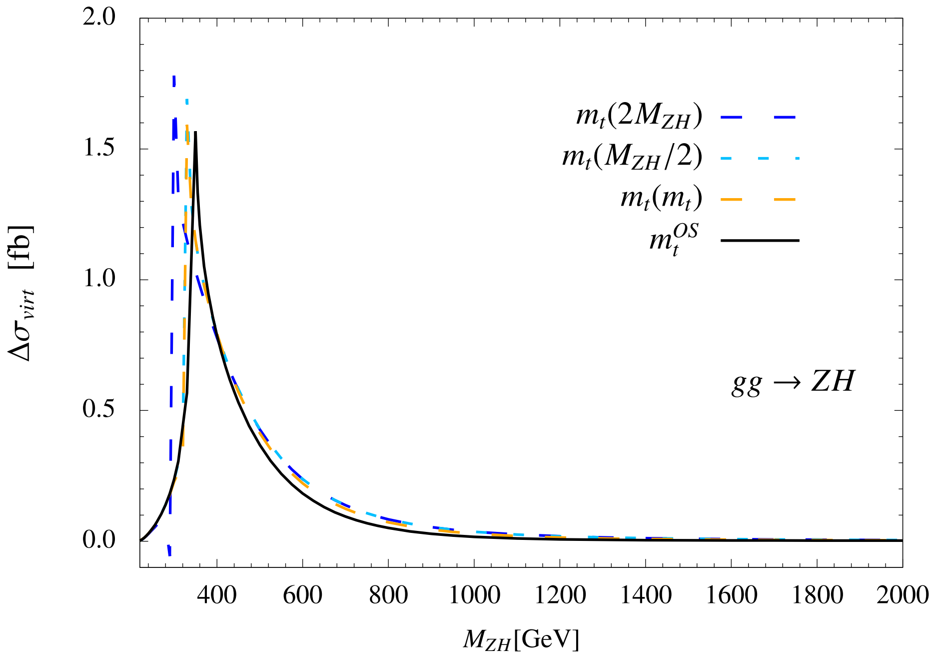

Figure 4.6: $\Delta\sigma_{\text{virt}}$ as a function of the invariant mass, obtained from the merging of the NLO predictions in the p_T and HE expansions. The solid line shows the results by using the on-shell renormalization for the top mass. The dashed lines show the results in the $\overline{\text{MS}}$ renormalization scheme, assuming different values for the renormalization scale μ_R. Courtesy of Ramona Gröber.

Chapter 5

Conclusions

The calculation of higher-order corrections in Higgs-related processes at hadron colliders is a challenging task which must be accomplished in order to provide accurate predictions to be compared with the experimental measurements. The QCD corrections associated to $2 \to 2$ gluon-initiated processes are known to be substantial, but the presence of two-loop multi-scale box integrals currently prevents an exact evaluation of the virtual corrections with analytical methods. The ignorance on these higher-order effects represents one of the limiting factors to the reduction of theoretical uncertainties in SM predictions.

In this thesis we applied the method of the p_T expansion proposed in ref. [39] to obtain an analytical approximation of the virtual QCD corrections due to top-quark loops in gluon-initiated ZH and ZZ production.

In chap. 2 we showed that it is possible to obtain an analytical approximation of the virtual QCD corrections to $gg \to ZH$ at NLO using an expansion of the amplitude in terms of a forward kinematics. The combination of the p_T expansion and of the IBP reduction technique that we have discussed allowed to approximate the two-loop box integrals using integrals which have a much simpler structure and which are already known in the literature. Loops of top quarks give the dominant contribution to the virtual corrections of $gg \to ZH$, therefore the calculation of these effects is very important. Our results can provide a reliable prediction for almost the totality of the hadronic cross section at LHC energies.

The expressions that we obtained for the NLO results are relatively simple, and the time of evaluation of the virtual corrections for a single point in phase space is only limited by the time of evaluation of the 52 MIs which constitute the final result. With the routines used in our work we were able to evaluate a single point of $\mathcal{V}_{\text{fin}}$ in less than one second.

In chap. 3 we presented the application of the p_T expansion to the calculation of top-quark loops in $gg \to ZZ$. Although in this process top effects are not the most relevant ones, they are important for an accurate description of Higgs production via gluon fusion and to constrain the total decay width of the Higgs. We have tested the reliability of the p_T expansion by comparing its results with the exact prediction at LO. Then we considered the NLO corrections in QCD: the contribution from two-loop irreducible triangle diagrams and from double triangles has been evaluated exactly, whereas the p_T expansion was used to approximate the two-loop box integrals. For the latter, we obtained analytical expressions for the first three orders in the expansion, that are expected to provide an accurate approximation of the box form factors in the range $p_T \lesssim 300$ GeV.

Based on the study of the above processes, we can identify two main limitations to the applicability of the p_T expansion, one technical and one more theoretical.

The technical limitation is connected to the length of the intermediate expressions involved in the IBP reduction. When higher orders in the p_T expansion are considered, the number of terms in the intermediate expressions increases roughly by a factor of 100, and this has forced us to stop our approximations at $\mathcal{O}(p_T^4)$ in the computation for $gg \to ZH$ and especially for $gg \to ZZ$. However, from the comparison with the full prediction at LO and with the exact numerical results at NLO in the case of $gg \to ZH$, we showed that three orders in the p_T expansion are enough to reach an accuracy, w.r.t. the exact result, of the permille level in a region of the phase space which is relevant for LHC studies. We also remark that, thanks to the lightness of the symbolic rules produced with `LiteRed` and to an optimized usage of the `Mathematica` computing resources, our method could be implemented on a desktop computer.

The theoretical limitation is related to the hierarchy that is established in the p_T expansion among the various energy scales in the calculation. One consequence of this hierarchy is that processes involving light virtual particles in the loops, like gluon-initiated W^+W^- production or $gg \to ZZ$ mediated by loops of light quarks, cannot be studied with the p_T expansion. Another consequence is that when only heavy particles are involved in the problem, the hierarchy prevents the approximation to converge in every region of the phase space.

Motivated by this latter issue, in chap. 4 we investigated the possibility of an analytical approximation of the virtual NLO corrections for $gg \to ZH$ which could be valid in any point of the phase space $(\hat{s}, \hat{t})$. We suggest that such an approximation can be obtained by combining the results of the p_T and the HE expansions. Indeed, we showed that the validity regions of the latter are complementary, and by selecting the results of either the p_T or the HE expansion according to the relevant phase-space region we could provide a merged prediction which agrees very well with the exact LO results. In order to achieve a sufficient level of accuracy for every phase-space point, we showed that not only the p_T and HE expansions must be combined, but they also need to be improved by constructing the respective Padé approximants. Additionally, we used the approximants to cross-check the compatibility of the HE-expanded results with the p_T-expanded ones. Given that the accuracy of the approximations provided by the p_T and HE expansions is not related to the perturbative order considered, we expect that our merging method can accurately reproduce also the virtual NLO corrections.

The computing time for the numerical evaluation of our merged prediction is not affected by the combination of the two analytical approximations, and the inclusion of the HE results still allows to evaluate one point of $\mathcal{V}_{\text{fin}}$ in less than one second. This figure is competitive with the results of the small-mass expansion of ref. [38], which quotes an average time of 2 seconds. In particular, once the real-emission contributions are included in our results, an implementation in a Monte Carlo code is viable. Therefore, our merged prediction could be used for phenomenological studies both at the LHC and at future hadronic colliders.

We finally note that the merging method studied in chap. 4 could be straightforwardly applied also to other processes for which the results of both the p_T and HE expansions are available, namely for $gg \to HH$ [39, 123] and for $gg \to ZZ$ [36]. In the future, the method can be also applied to other 2→2 processes involving top loops, like $gg \to \gamma\gamma$ and $gg \to \gamma Z$.

Appendix A

Results for $gg \to ZH$

A.1 Projectors

We present the explicit expressions of the orthonormal projectors $\mathcal{P}_i^{\mu\nu\rho}$ appearing in eq.(2.18). Following the notation of sec. 2.3, we obtain

$$\mathcal{P}_1^{\mu\nu\rho} = \frac{m_Z}{\sqrt{2}s'p_T^2}\left[S_2^{\mu\nu\rho}t' - S_1^{\mu\nu\rho}u' + \frac{s'S_{11}^{\mu\nu\rho}}{t'} + \frac{s'S_{12}^{\mu\nu\rho}}{u'} + \frac{S_5^{\mu\nu\rho}u'}{s'} - \frac{S_6^{\mu\nu\rho}t'}{s'} - \frac{S_{13}^{\mu\nu\rho}t'}{u'} - \frac{S_{14}^{\mu\nu\rho}u'}{t'}\right], \tag{A.1}$$

$$\mathcal{P}_2^{\mu\nu\rho} = \frac{1}{\sqrt{2}s'p_T}\left[\frac{s'S_{11}^{\mu\nu\rho}}{t'} + \frac{s'S_{12}^{\mu\nu\rho}}{u'} - \frac{S_{13}^{\mu\nu\rho}t'}{u'} - \frac{S_{14}^{\mu\nu\rho}u'}{t'}\right], \tag{A.2}$$

$$\begin{aligned}\mathcal{P}_3^{\mu\nu\rho} = \frac{\sqrt{3}}{2s'p_T}\Bigg[&\left(\frac{s'S_{11}^{\mu\nu\rho}}{t'} - \frac{s'S_{12}^{\mu\nu\rho}}{u'} + \frac{S_{13}^{\mu\nu\rho}t'}{u'} - \frac{S_{14}^{\mu\nu\rho}u'}{t'}\right)\frac{(p_T^2+3m_Z^2)}{3p_T^2} \\ &+ \left(S_5^{\mu\nu\rho}u' + S_6^{\mu\nu\rho}t'\right)\frac{(m_Z^2-p_T^2)}{p_T^2 s'} - \frac{S_{10}^{\mu\nu\rho}m_Z^2}{p_T^2} - \frac{S_9^{\mu\nu\rho}m_Z^2}{p_T^2} + S_1^{\mu\nu\rho}u' + S_2^{\mu\nu\rho}t'\Bigg],\end{aligned} \tag{A.3}$$

$$\mathcal{P}_4^{\mu\nu\rho} = \frac{m_Z}{\sqrt{2}s'p_T^2}\left[\frac{s'S_{11}^{\mu\nu\rho}}{t'} - \frac{s'S_{12}^{\mu\nu\rho}}{u'} + \frac{S_5^{\mu\nu\rho}u'}{s'} + \frac{S_6^{\mu\nu\rho}t'}{s'} + \frac{S_{13}^{\mu\nu\rho}t'}{u'} - \frac{S_{14}^{\mu\nu\rho}u'}{t'} - S_9^{\mu\nu\rho} - S_{10}^{\mu\nu\rho}\right], \tag{A.4}$$

$$\mathcal{P}_5^{\mu\nu\rho} = \frac{1}{\sqrt{6}s'p_T}\left[-\frac{s'S_{11}^{\mu\nu\rho}}{t'} + \frac{s'S_{12}^{\mu\nu\rho}}{u'} - \frac{S_{13}^{\mu\nu\rho}t'}{u'} + \frac{S_{14}^{\mu\nu\rho}u'}{t'}\right], \tag{A.5}$$

$$\begin{aligned}\mathcal{P}_6^{\mu\nu\rho} = \frac{1}{s'p_T}\Bigg[&\left(\frac{s'S_{11}^{\mu\nu\rho}}{t'} - \frac{s'S_{12}^{\mu\nu\rho}}{u'} + \frac{S_5^{\mu\nu\rho}u'}{s'} + \frac{S_6^{\mu\nu\rho}t'}{s'} + \frac{S_{13}^{\mu\nu\rho}t'}{u'} - \frac{S_{14}^{\mu\nu\rho}u'}{t'}\right)\frac{(p_T^2+m_Z^2)}{2p_T^2} \\ &- \frac{S_{10}^{\mu\nu\rho}m_Z^2}{2p_T^2} - \frac{S_9^{\mu\nu\rho}m_Z^2}{2p_T^2} - \frac{S_1^{\mu\nu\rho}u'}{2} - \frac{S_2^{\mu\nu\rho}t'}{2} + S_4^{\mu\nu\rho} + S_7^{\mu\nu\rho} - S_8^{\mu\nu\rho} + s'S_3^{\mu\nu\rho}\Bigg]\end{aligned} \tag{A.6}$$

We also present the relations that allow to express the $\mathcal{A}_i$ computed in this thesis in terms of the form factors presented in ref. [35]. We make use of these relations in chap. 4, as they are needed to adapt the results of the HE expansion for the merging with those obtained in chap. 2.

$$\mathcal{A}_1 = \frac{p_T^2}{2\sqrt{2} m_Z (p_T^2 + m_Z^2)} \left[(t' + u') F_{12}^+ - (t' - u') F_{12}^- \right], \tag{A.7}$$

$$\begin{aligned} \mathcal{A}_2 = &- \frac{p_T}{2\sqrt{2}(p_T^2 + m_Z^2)} \Bigg[(t' + u') F_{12}^+ - (t' - u') F_{12}^- \\ &- \frac{p_T^2 + m_Z^2}{2s'} \left((t' + u') F_3^+ - (t' - u') F_3^- \right) \Bigg], \end{aligned} \tag{A.8}$$

$$\begin{aligned} \mathcal{A}_3 = &\frac{p_T}{2\sqrt{3}(p_T^2 + m_Z^2)} \Bigg[(t' + u') F_{12}^- - (t' - u') F_{12}^+ \\ &+ (p_T^2 + m_Z^2)(F_2^- + F_4) \Bigg], \end{aligned} \tag{A.9}$$

$$\begin{aligned} \mathcal{A}_4 = &- \frac{m_Z}{2\sqrt{2}(p_T^2 + m_Z^2)} \Bigg[(t' + u') F_{12}^- - (t' - u') F_{12}^+ \\ &+ (p_T^2 + m_Z^2) \left(\left(1 - \frac{p_T^2}{m_Z^2} \right) F_2^- + 2F_4 \right) \Bigg], \end{aligned} \tag{A.10}$$

$$\begin{aligned} \mathcal{A}_5 = &\frac{p_T}{2\sqrt{6}(p_T^2 + m_Z^2)} \Bigg[(t' + u') F_{12}^- - (t' - u') F_{12}^+ \\ &+ (p_T^2 + m_Z^2) \left(4(F_2^- + F_4) + \frac{3}{2s'} \left((t' + u') F_3^- - (t' - u') F_3^+ \right) \right) \Bigg], \end{aligned} \tag{A.11}$$

$$\mathcal{A}_6 = \frac{p_T}{2} F_4. \tag{A.12}$$

A.2 Analytical Results

LO Box Form Factor With reference to eq.(2.49) we report here the analytical expression for the form factor $\mathcal{A}_1^{(0,\square)}$ as a result of the p_T expansion, up to $\mathcal{O}(p_T^4)$ terms. We expressed the result in terms of the frequent combination $w_t = 4m_t^2 + \hat{s}$.

$$
\begin{aligned}
\mathcal{A}_1^{(0,\square)} = \frac{p_T^2 m_t^2}{\sqrt{2} m_Z (p_T^2 + m_Z^2)} \Bigg\{ & C_0(0,0,0,\hat{s},m_t^2,m_t^2,m_t^2) \Bigg[-\frac{9\hat{s}}{2} + \frac{3w_t}{2} + \left(-\frac{w_t^2}{2\hat{s}^2} + \frac{2w_t}{\hat{s}} - \frac{3}{2} \right) p_T^2 \\
& + \left(-\frac{w_t^2}{4\hat{s}^2} + \frac{3w_t}{2\hat{s}} - \frac{5}{4} \right) m_Z^2 + p_T^2 m_Z^2 \left(\frac{w_t^3}{8\hat{s}^4} - \frac{15w_t^2}{8\hat{s}^3} + \frac{47w_t}{8\hat{s}^2} - \frac{25}{8\hat{s}} \right) \\
& + \left(-\frac{w_t^2}{2\hat{s}^3} + \frac{2w_t}{\hat{s}^2} + \frac{1}{2\hat{s}} \right) m_Z^2 \Delta_m + p_T^2 \Delta_m \left(-\frac{w_t^2}{\hat{s}^3} + \frac{4w_t}{\hat{s}^2} - \frac{3}{\hat{s}} \right) \\
& + \left(\frac{3w_t^3}{16\hat{s}^4} - \frac{21w_t^2}{16\hat{s}^3} + \frac{49w_t}{16\hat{s}^2} - \frac{31}{16\hat{s}} \right) p_T^4 + \left(-\frac{3w_t^2}{4\hat{s}^3} + \frac{2w_t}{\hat{s}^2} + \frac{11}{4\hat{s}} \right) m_Z^4 \Bigg] \\
& + B_0(\hat{s},m_t^2,m_t^2) \Bigg[-3 + \left(\frac{w_t}{\hat{s}^2} - \frac{7}{3\hat{s}} + \frac{4}{3(w_t-\hat{s})} \right) p_T^2 + \left(\frac{w_t}{2\hat{s}^2} - \frac{13}{6\hat{s}} + \frac{8}{3(w_t-\hat{s})} \right) m_Z^2 \\
& + \left(-\frac{3w_t^2}{8\hat{s}^4} + \frac{2w_t}{\hat{s}^3} + \frac{26}{15\hat{s}(w_t-\hat{s})} - \frac{113}{40\hat{s}^2} - \frac{8}{15(w_t-\hat{s})^2} \right) p_T^4 \\
& + \left(\frac{3w_t}{2\hat{s}^3} + \frac{6}{\hat{s}(w_t-\hat{s})} - \frac{3}{2\hat{s}^2} \right) m_Z^4 + \left(\frac{w_t}{\hat{s}^3} + \frac{16}{3\hat{s}(w_t-\hat{s})} - \frac{7}{3\hat{s}^2} \right) m_Z^2 \Delta_m \\
& + p_T^2 m_Z^2 \left(-\frac{w_t^2}{4\hat{s}^4} + \frac{10w_t}{3\hat{s}^3} + \frac{28}{5\hat{s}(w_t-\hat{s})} - \frac{373}{60\hat{s}^2} - \frac{4}{5(w_t-\hat{s})^2} \right) \Bigg] \\
& + C_0(0,0,-\hat{s},m_t^2,m_t^2,m_t^2) \Bigg[\frac{3\hat{s}}{2} - \frac{3w_t}{2} + \left(\frac{w_t^2}{2\hat{s}^2} - \frac{2w_t}{\hat{s}} + \frac{3}{2} \right) p_T^2 \\
& + 4\Delta_m + \left(\frac{w_t^2}{4\hat{s}^2} - \frac{3w_t}{2\hat{s}} + \frac{13}{4} \right) m_Z^2 + p_T^2 \Delta_m \left(\frac{2w_t}{\hat{s}^3} + \frac{8}{3\hat{s}(w_t-\hat{s})} - \frac{14}{3\hat{s}^2} \right) \\
& + \left(-\frac{3w_t^3}{16\hat{s}^4} + \frac{21w_t^2}{16\hat{s}^3} - \frac{49w_t}{16\hat{s}^2} + \frac{31}{16\hat{s}} \right) p_T^4 + \left(\frac{3w_t^2}{4\hat{s}^3} - \frac{2w_t}{\hat{s}^2} + \frac{13}{4\hat{s}} \right) m_Z^4 \\
& + p_T^2 \Delta_m \left(\frac{w_t^2}{\hat{s}^3} - \frac{4w_t}{\hat{s}^2} + \frac{3}{\hat{s}} \right) + p_T^2 m_Z^2 \left(-\frac{w_t^3}{8\hat{s}^4} + \frac{15w_t^2}{8\hat{s}^3} - \frac{47w_t}{8\hat{s}^2} + \frac{41}{8\hat{s}} \right) \\
& + \left(\frac{w_t^2}{2\hat{s}^3} - \frac{2w_t}{\hat{s}^2} + \frac{7}{2\hat{s}} \right) m_Z^2 \Delta_m \Bigg]
\end{aligned}
$$

$$
\begin{aligned}
&+ B_0(-\hat{s}, m_t^2, m_t^2)\Bigg[3 + \left(-\frac{w_t}{\hat{s}^2} + \frac{11}{3\hat{s}} - \frac{4}{3(w_t-\hat{s})} - \frac{2}{w_t}\right)p_T^2 - \frac{4\Delta_m}{w_t} \\
&+ \left(-\frac{w_t}{2\hat{s}^2} + \frac{17}{6\hat{s}} - \frac{8}{3(w_t-\hat{s})} - \frac{4}{w_t}\right)m_Z^2 + \left(-\frac{3w_t}{2\hat{s}^3} + \frac{7}{2\hat{s}^2} - \frac{6}{\hat{s}w_t} - \frac{1}{w_t^2}\right)m_Z^4 \\
&+ \left(\frac{3w_t^2}{8\hat{s}^4} - \frac{5w_t}{2\hat{s}^3} - \frac{4}{15\hat{s}(w_t-\hat{s})} + \frac{213}{40\hat{s}^2} + \frac{8}{15(w_t-\hat{s})^2} - \frac{11}{4\hat{s}w_t} - \frac{1}{4w_t^2}\right)p_T^4 \\
&+ \left(-\frac{3}{\hat{s}w_t} - \frac{1}{w_t^2}\right)\Delta_m^2 + p_T^2\Delta_m\left(-\frac{2w_t}{\hat{s}^3} - \frac{8}{3\hat{s}(w_t-\hat{s})} + \frac{22}{3\hat{s}^2} - \frac{7}{\hat{s}w_t} - \frac{1}{w_t^2}\right) \\
&+ p_T^2 m_Z^2\left(\frac{w_t^2}{4\hat{s}^4} - \frac{11w_t}{3\hat{s}^3} - \frac{2}{5\hat{s}(w_t-\hat{s})} + \frac{211}{20\hat{s}^2} + \frac{4}{5(w_t-\hat{s})^2} - \frac{8}{\hat{s}w_t} - \frac{1}{w_t^2}\right) \\
&+ \left(-\frac{w_t}{\hat{s}^3} - \frac{4}{3\hat{s}(w_t-\hat{s})} + \frac{11}{3\hat{s}^2} - \frac{10}{\hat{s}w_t} - \frac{2}{w_t^2}\right)m_Z^2\Delta_m\Bigg] \\
&+ \log\left(\frac{m_t^2}{\mu_R^2}\right)\Bigg[\left(\frac{4}{3\hat{s}} - \frac{2}{w_t}\right)p_T^2 + \left(\frac{2}{3\hat{s}} - \frac{4}{w_t}\right)m_Z^2 - \frac{4\Delta_m}{w_t} + \left(-\frac{3}{\hat{s}w_t} - \frac{1}{w_t^2}\right)\Delta_m^2 \\
&+ \left(-\frac{w_t}{2\hat{s}^3} + \frac{22}{15\hat{s}(w_t-\hat{s})} + \frac{5}{2\hat{s}^2} - \frac{11}{4\hat{s}w_t} - \frac{1}{4w_t^2}\right)p_T^4 + \left(\frac{6}{\hat{s}(w_t-\hat{s})} + \frac{2}{\hat{s}^2} - \frac{6}{\hat{s}w_t} - \frac{1}{w_t^2}\right)m_Z^4 \\
&+ p_T^2\Delta_m\left(\frac{8}{3\hat{s}^2} - \frac{7}{\hat{s}w_t} - \frac{1}{w_t^2}\right) + p_T^2 m_Z^2\left(-\frac{w_t}{3\hat{s}^3} + \frac{26}{5\hat{s}(w_t-\hat{s})} + \frac{13}{3\hat{s}^2} - \frac{8}{\hat{s}w_t} - \frac{1}{w_t^2}\right) \\
&+ \left(\frac{4}{\hat{s}(w_t-\hat{s})} + \frac{4}{3\hat{s}^2} - \frac{10}{\hat{s}w_t} - \frac{2}{w_t^2}\right)m_Z^2\Delta_m\Bigg] \\
&+ \left(\frac{4}{w_t} - \frac{2}{\hat{s}}\right)p_T^2 + \left(\frac{8}{w_t} - \frac{1}{\hat{s}}\right)m_Z^2 + \frac{8\Delta\mathrm{m}}{w_t} + \left(\frac{4}{\hat{s}(w_t-\hat{s})} - \frac{3}{\hat{s}^2} + \frac{10}{\hat{s}w_t} + \frac{2}{w_t^2}\right)m_Z^4 \\
&+ \left(\frac{3w_t}{4\hat{s}^3} - \frac{2}{5\hat{s}(w_t-\hat{s})} - \frac{15}{4\hat{s}^2} + \frac{5}{\hat{s}w_t} + \frac{1}{2w_t^2}\right)p_T^4 + \left(-\frac{4}{\hat{s}(w_t-\hat{s})} + \frac{4}{\hat{s}w_t} + \frac{2}{w_t^2}\right)\Delta_m^2 \\
&+ p_T^2\Delta_m\left(-\frac{4}{\hat{s}(w_t-\hat{s})} - \frac{4}{\hat{s}^2} + \frac{12}{\hat{s}w_t} + \frac{2}{w_t^2}\right) + p_T^2 m_Z^2\left(\frac{w_t}{2\hat{s}^3} + \frac{2}{5\hat{s}(w_t-\hat{s})} - \frac{13}{2\hat{s}^2} + \frac{14}{\hat{s}w_t} + \frac{2}{w_t^2}\right) \\
&+ \left(-\frac{4}{\hat{s}(w_t-\hat{s})} - \frac{2}{\hat{s}^2} + \frac{16}{\hat{s}w_t} + \frac{4}{w_t^2}\right)m_Z^2\Delta_m\Bigg\}
\end{aligned}
\tag{A.13}
$$

Results for Double-Triangle Diagrams With reference to eq.(2.62), we present here the exact results for the double-triangle contributions to all the NLO form factors. We find

$$\mathcal{A}_1^{(1,\bowtie)} = -\frac{m_t^2 p_T^2}{4\sqrt{2}\, m_Z \left(m_Z^2 + p_T^2\right)^2} \left[F_t(\hat{t}) \left(G_t(\hat{t},\hat{u}) - G_b(\hat{t},\hat{u}) \right) + (\hat{t} \leftrightarrow \hat{u}) \right], \tag{A.14}$$

$$\mathcal{A}_2^{(1,\bowtie)} = \frac{m_t^2 p_T}{4\sqrt{2} \left(m_Z^2 + p_T^2\right)^2} \left[F_t(\hat{t}) \left(G_t(\hat{t},\hat{u}) - G_b(\hat{t},\hat{u}) \right) + (\hat{t} \leftrightarrow \hat{u}) \right], \tag{A.15}$$

$$\mathcal{A}_3^{(1,\bowtie)} = \frac{m_t^2 p_T}{4\sqrt{3}\, \hat{s} \left(m_Z^2 + p_T^2\right)^2} \left[\left(m_H^2 - \hat{t}\right) F_t(\hat{t}) \left(G_t(\hat{t},\hat{u}) - G_b(\hat{t},\hat{u}) \right) - (\hat{t} \leftrightarrow \hat{u}) \right], \tag{A.16}$$

$$\begin{aligned} \mathcal{A}_4^{(1,\bowtie)} = &-\frac{m_t^2}{4\sqrt{2}\, m_Z \hat{s}^2 \left(m_Z^2 + p_T^2\right)^2} \left[\left(m_Z^2 \left(m_H^2 - \hat{t}\right)^2 \right.\right. \\ &\left.\left. - \hat{t} \left(m_Z^2 - \hat{u}\right)^2 \right) F_t(\hat{t}) \left(G_t(\hat{t},\hat{u}) - G_b(\hat{t},\hat{u}) \right) - (\hat{t} \leftrightarrow \hat{u}) \right], \end{aligned} \tag{A.17}$$

$$\begin{aligned} \mathcal{A}_5^{(1,\bowtie)} = &-\frac{m_t^2 p_T}{4\sqrt{6}\, \hat{s} \left(m_Z^2 + p_T^2\right)^2} \left[\left(4m_Z^2 - \hat{s} - 4\hat{u}\right) F_t(\hat{t}) \left(G_t(\hat{t},\hat{u}) - G_b(\hat{t},\hat{u}) \right) \right. \\ &\left. - (\hat{t} \leftrightarrow \hat{u}) \right], \end{aligned} \tag{A.18}$$

$$\mathcal{A}_6^{(1,\bowtie)} = 0, \tag{A.19}$$

where

$$\begin{aligned} F_t(\hat{t}) = &\frac{1}{\left(m_H^2 - \hat{t}\right)^2} \left[2\hat{t} \Big(B_0\left(\hat{t}, m_t^2, m_t^2\right) - B_0\left(m_H^2, m_t^2, m_t^2\right) \Big) \right. \\ &\left. + \left(m_H^2 - \hat{t}\right) \Big(\left(m_H^2 - 4m_t^2 - \hat{t}\right) C_0\left(0, m_H^2, \hat{t}, m_t^2, m_t^2, m_t^2\right) - 2 \Big) \right], \end{aligned} \tag{A.20}$$

$$\begin{aligned} G_x(\hat{t},\hat{u}) = &\left(m_Z^2 - \hat{u}\right) \left[m_Z^2 \Big(B_0\left(\hat{t}, m_x^2, m_x^2\right) - B_0\left(m_Z^2, m_x^2, m_x^2\right) \Big) \right. \\ &\left. + \left(\hat{t} - m_Z^2\right) \Big(2m_x^2 C_0\left(0, \hat{t}, m_Z^2, m_x^2, m_x^2, m_x^2\right) + 1 \Big) \right]. \end{aligned} \tag{A.21}$$

The Passarino-Veltman scalar functions B_0 and C_0 are defined as in eqs.(2.56, 2.57).

Results for Triangle Diagrams at NLO With reference to eq.(2.62), we present here the exact results for the two-loop one-particle-irreducible triangle contributions to all the NLO form factors. We obtain

$$\mathcal{A}_1^{(1,\triangle)} = \frac{p_T^2\,(\hat{s}-\Delta_m)}{4\sqrt{2}m_Z}\frac{\mathcal{K}_t^{(2l)}}{(p_T^2+m_Z^2)}, \tag{A.22}$$

$$\mathcal{A}_2^{(1,\triangle)} = -\frac{p_T\,(\hat{s}-\Delta_m)}{4\sqrt{2}}\frac{\mathcal{K}_t^{(2l)}}{(p_T^2+m_Z^2)}, \tag{A.23}$$

$$\mathcal{A}_3^{(1,\triangle)} = \frac{p_T\,(\hat{t}-\hat{u})}{4\sqrt{3}}\frac{\mathcal{K}_t^{(2l)}}{(p_T^2+m_Z^2)}, \tag{A.24}$$

$$\mathcal{A}_4^{(1,\triangle)} = -\frac{m_Z\,(\hat{t}-\hat{u})}{4\sqrt{2}}\frac{\mathcal{K}_t^{(2l)}}{(p_T^2+m_Z^2)}, \tag{A.25}$$

$$\mathcal{A}_5^{(1,\triangle)} = -\frac{p_T\,(\hat{t}-\hat{u})}{4\sqrt{6}}\frac{\mathcal{K}_t^{(2l)}}{(p_T^2+m_Z^2)}, \tag{A.26}$$

$$\mathcal{A}_6^{(1,\triangle)} = 0, \tag{A.27}$$

where the $\mathcal{K}_t^{(2l)}$ function is defined in eq.(4.11) of ref. [77].

A.3 Master Integrals

The following list includes the 52 MIs that resulted from the IBP reduction of the $\mathcal{A}_i^{(1,\square)}$ form factors discussed in sec. 2.8. The integral families to which these MIs belong are defined in tab. 2.2. The same list of MIs has been used in the calculation of the $\mathcal{A}_i^{(1,\square)}$ form factors for $gg \to ZZ$, presented in chap. 3.

$$
\begin{aligned}
&\{J_1(0,0,1,0,0,0,1,0,0), J_1(0,0,1,0,1,0,1,0,0), J_1(0,0,1,0,1,1,1,0,0),\\
&J_1(0,0,1,1,1,0,0,0,0), J_1(0,0,1,1,1,1,0,0,0), J_1(0,0,2,1,1,0,0,0,0),\\
&J_1(0,1,0,1,1,0,1,0,0), J_1(0,1,0,2,1,0,1,0,0), J_1(0,1,1,1,1,0,1,0,0),\\
&J_1(0,1,1,1,1,1,0,0,0), J_1(0,2,0,1,1,0,1,0,0), J_1(0,2,1,1,1,0,1,0,0),\\
&J_1(1,0,1,0,1,0,1,0,0), J_1(1,0,1,0,1,1,1,0,0), J_1(1,1,1,0,1,1,1,0,0),\\
&J_2(0,0,1,0,0,1,1,0,0), J_2(0,0,1,0,1,1,1,0,0), J_2(0,0,1,1,0,1,1,0,0),\\
&J_2(0,0,1,1,1,1,1,0,0), J_2(0,0,1,2,0,1,1,0,0), J_2(0,0,2,1,0,1,1,0,0),\\
&J_2(0,1,0,1,0,1,0,0,0), J_2(0,1,0,1,1,1,0,0,0), J_2(0,1,1,1,0,1,1,0,0),\\
&J_2(0,1,1,1,1,1,1,0,0), J_2(0,2,0,1,0,1,0,0,0), J_2(0,2,1,1,0,1,1,0,0),\\
&J_2(1,1,0,0,0,1,1,0,0), J_2(1,1,0,0,1,1,1,0,0), J_2(1,1,0,1,1,0,1,0,0),\\
&J_2(1,1,1,0,1,1,1,0,0), J_2(1,1,1,1,1,1,1,0,0), J_2(2,1,0,1,1,0,1,0,0),\\
&J_3(1,0,1,1,1,1,0,0,0), J_3(1,1,1,0,1,1,1,0,0), J_4(1,0,1,1,1,1,1,0,0),\\
&J_4(1,1,1,1,0,0,1,0,0), J_4(1,1,1,1,0,1,1,0,0), J_5(0,0,1,0,1,0,1,0,0),\\
&J_5(0,1,1,0,1,1,0,0,0), J_5(0,1,1,0,1,1,1,0,0), J_5(0,2,1,0,1,1,0,0,0),\\
&J_5(1,1,1,0,1,1,1,0,0), J_5(2,1,1,0,1,1,1,0,0), J_6(1,1,1,0,1,1,1,0,0),\\
&J_6(1,1,1,1,1,1,1,0,0), J_7(0,1,1,0,0,1,1,0,0), J_7(0,1,1,0,1,1,1,0,0),\\
&J_7(1,1,1,0,0,1,1,0,0), J_7(1,1,1,0,1,1,1,0,0), J_7(1,1,1,1,1,1,1,0,0),\\
&J_8(0,1,1,1,1,1,1,0,0)\}
\end{aligned}
$$

A.4 Additional Plots

In chap. 2 we presented the results of the p_T expansion by discussing the form factor $\mathcal{A}_1$ in detail. In this section we summarize the results for all the other form factors contributing to the $gg \to ZH$ amplitude. In fig. A.1 we show that $\mathcal{A}_1$ is indeed the form factor which gives the dominant contribution to the LO partonic cross section, especially for values of invariant masses greater than 400 GeV.

In fig. A.2 we show the absolute value of the box form factors at LO for a partonic c.o.m. energy of 1600 GeV. This value is chosen as a representative value of the high-energy kinematical regime, where the p_T expansion can provide accurate results only for $p_T \lesssim 300$ GeV. We notice that the behavior of the form factors shown in fig. A.2 is very similar to the one of $\mathcal{A}_1^{(0,\Box)}$, discussed in sec. 2.7.2. Finally, in fig. A.3 we show the absolute value of all the $\mathcal{A}_i^{(1,\Box)}$: as a general feature, one can see that the $\mathcal{O}(p_T^2)$ and the $\mathcal{O}(p_T^4)$ results are always in agreement for $p_T \lesssim 200$ GeV, but begin to diverge for larger p_T. However, by comparing with the behavior at LO (fig. A.2), for which the exact result is known, it is reasonable to expect that the $\mathcal{O}(p_T^4)$ result can still be accurate for $p_T \lesssim 300$ GeV.

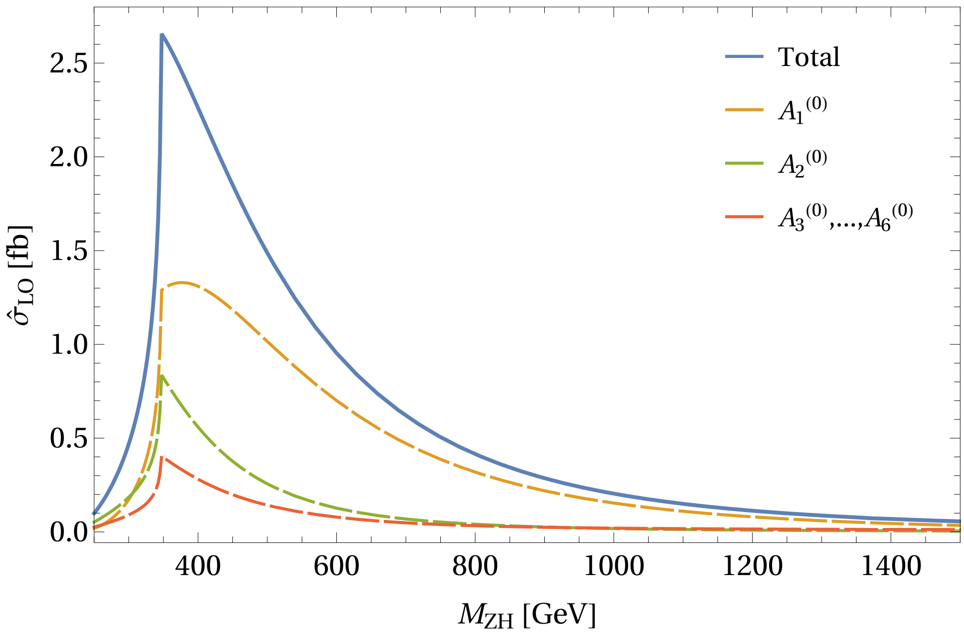

Figure A.1: Contributions to the LO partonic cross section from the various form factors $\mathcal{A}_i^{(0)}$, shown as dashed lines: the contributions from $\mathcal{A}_1^{(0)}$ (yellow) and $\mathcal{A}_2^{(0)}$ (green) are shown separately, while the sum of the contributions from the remaining form factors is shown as a red line. The solid line represents the sum of all contributions.

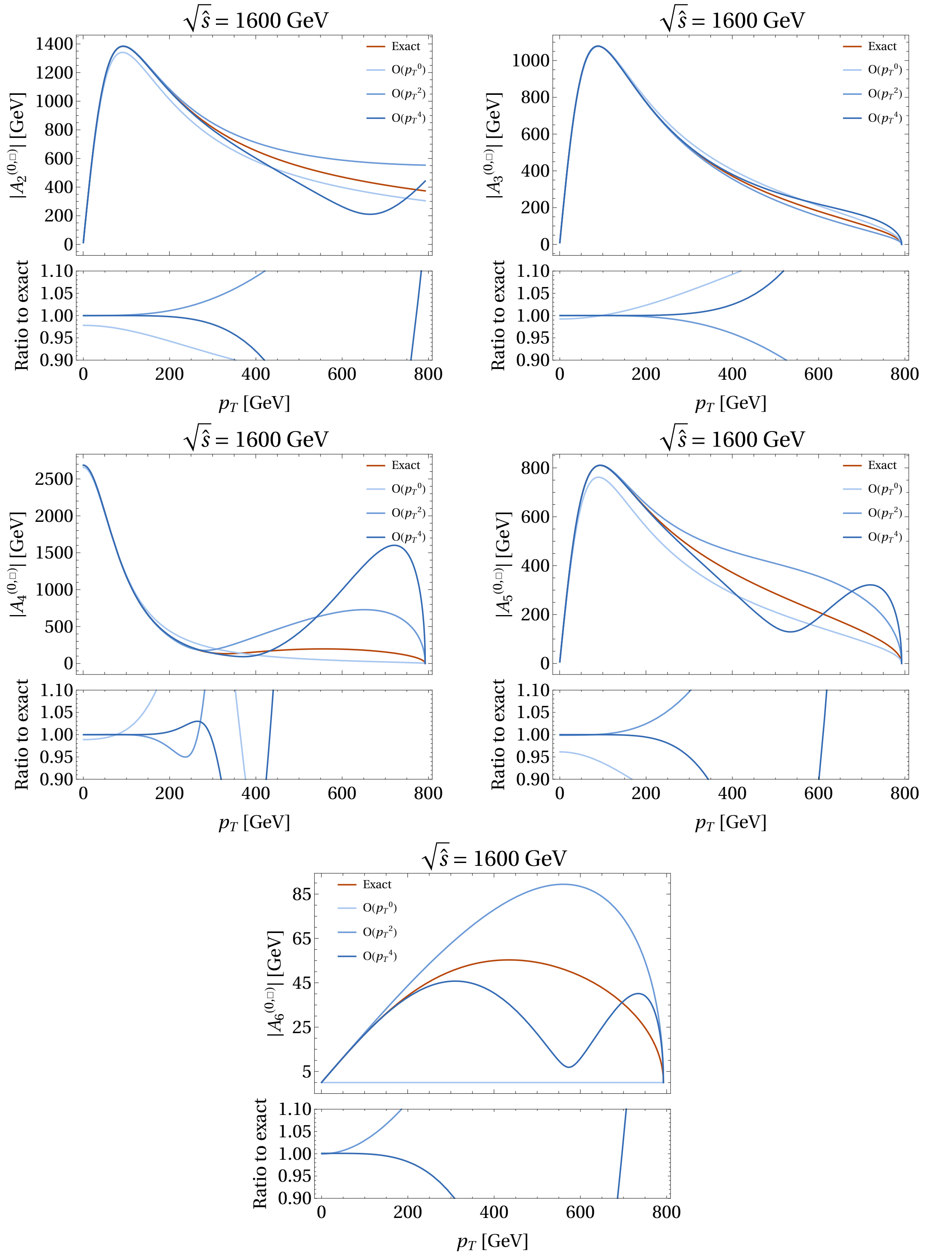

Figure A.2: Absolute value of the $\mathcal{A}_i^{(0,\square)}$ form factors for $i = 2, \ldots, 6$, for fixed $\sqrt{\hat{s}} = 1600$ GeV: the blue lines represent the first three orders of the p_T expansion, while the brown line stands for the exact result. The bottom part of each graph shows the ratio of the various orders of the p_T expansion to the exact result.

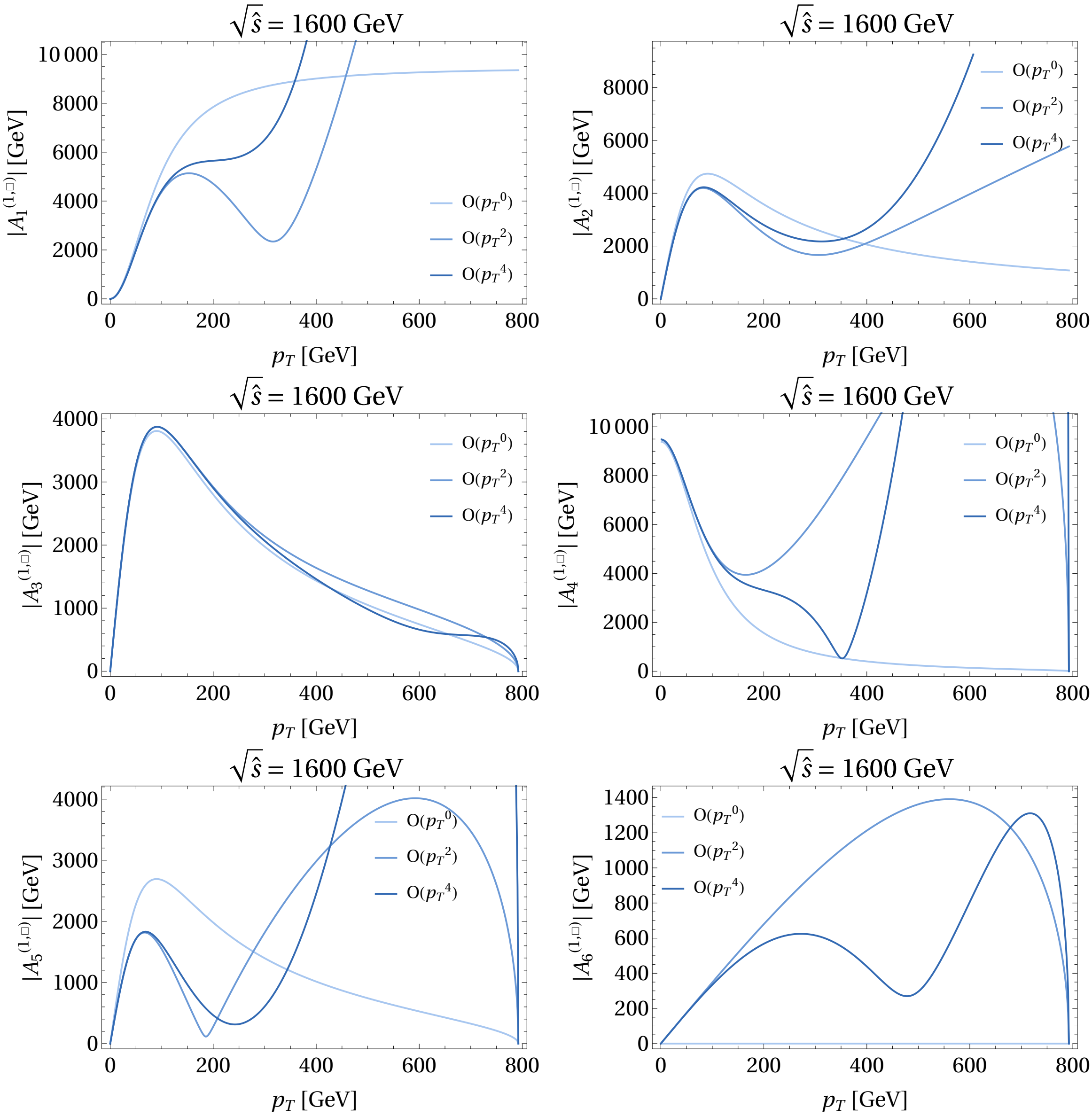

Figure A.3: Absolute value of the $\mathcal{A}_i^{(1,\Box)}$ form factors for $i = 1, \ldots, 6$, for fixed $\sqrt{\hat{s}} = 1600$ GeV, shown as a function of p_T: the blue lines represent the first three orders of the p_T expansion.

Appendix B

Results for $gg \to ZZ$

B.1 Projectors

We present the explicit expressions of the orthonormal projectors $\mathcal{P}_i^{\mu\nu\rho\sigma}$ appearing in eq.(3.15). Following the notation of sec. 3.3. The antisymmetric projectors under the exchange $\{\mu \leftrightarrow \nu$, $p_1 \leftrightarrow p_2\}$ are

$$\mathcal{P}_1^{\mu\nu\rho\sigma} = \frac{m_Z}{\sqrt{2}p_T}\left[\frac{1}{p_T^2 s'}\left(S_{17}^{\mu\nu\rho\sigma} - S_{20}^{\mu\nu\rho\sigma}\right)\right] \tag{B.1}$$

$$\mathcal{P}_2^{\mu\nu\rho\sigma} = \frac{m_Z}{\sqrt{2}p_T}\left[\frac{1}{p_T^2 s'}\left(\frac{t'}{u'}S_{19}^{\mu\nu\rho\sigma} - \frac{u'}{t'}S_{18}^{\mu\nu\rho\sigma}\right)\right] \tag{B.2}$$

$$\mathcal{P}_3^{\mu\nu\rho\sigma} = \frac{m_Z}{\sqrt{2}p_T}\left[\frac{S_5^{\mu\nu\rho\sigma}}{u'} - \frac{S_6^{\mu\nu\rho\sigma}}{t'} - \frac{1}{p_T^2 s'}\left(S_{17}^{\mu\nu\rho\sigma} - S_{20}^{\mu\nu\rho\sigma} + \frac{u'}{t'}S_{18}^{\mu\nu\rho\sigma} - \frac{t'}{u'}S_{19}^{\mu\nu\rho\sigma}\right)\right] \tag{B.3}$$

$$\mathcal{P}_4^{\mu\nu\rho\sigma} = \frac{m_Z}{\sqrt{2}p_T}\left[\frac{1}{s'}\left(S_9^{\mu\nu\rho\sigma} - S_{12}^{\mu\nu\rho\sigma}\right) + \frac{1}{p_T^2 s'}\left(S_{17}^{\mu\nu\rho\sigma} - S_{20}^{\mu\nu\rho\sigma}\right)\right] \tag{B.4}$$

$$\mathcal{P}_5^{\mu\nu\rho\sigma} = \frac{m_Z}{\sqrt{2}p_T}\left[\frac{1}{s'}\left(\frac{t'}{u'}S_{11}^{\mu\nu\rho\sigma} - \frac{u'}{t'}S_{10}^{\mu\nu\rho\sigma}\right) + \frac{1}{p_T^2 s'}\left(\frac{t'}{u'}S_{19}^{\mu\nu\rho\sigma} - \frac{u'}{t'}S_{18}^{\mu\nu\rho\sigma}\right)\right] \tag{B.5}$$

$$\mathcal{P}_6^{\mu\nu\rho\sigma} = \frac{m_Z}{\sqrt{2}p_T}\left[\frac{S_{13}^{\mu\nu\rho\sigma}}{u'} - \frac{S_{16}^{\mu\nu\rho\sigma}}{t'} - \frac{1}{p_T^2 s'}\left(S_{17}^{\mu\nu\rho\sigma} - S_{20}^{\mu\nu\rho\sigma} + \frac{t'}{u'}S_{19}^{\mu\nu\rho\sigma} - \frac{u'}{t'}S_{18}^{\mu\nu\rho\sigma}\right)\right] \tag{B.6}$$

$$\begin{aligned}\mathcal{P}_7^{\mu\nu\rho\sigma} = \frac{m_Z^2}{\sqrt{2}p_T^2}&\left[\frac{\left(m_Z^2 - p_T^2\right)}{2m_Z^2}\left(\frac{S_{13}^{\mu\nu\rho\sigma}}{u'} - \frac{S_{16}^{\mu\nu\rho\sigma}}{t'}\right) + \frac{1}{m_Z^2 s'}\left(u' S_{14}^{\mu\nu\rho\sigma} - t' S_{15}^{\mu\nu\rho\sigma}\right)\right. \\ &\left. + \frac{1}{m_Z^2 s'}\left(S_{17}^{\mu\nu\rho\sigma} - S_{20}^{\mu\nu\rho\sigma} + \frac{t'}{u'}S_{19}^{\mu\nu\rho\sigma} - \frac{u'}{t'}S_{18}^{\mu\nu\rho\sigma}\right)\right]\end{aligned} \tag{B.7}$$

$$\begin{aligned}\mathcal{P}_8^{\mu\nu\rho\sigma} = \frac{m_Z^2}{\sqrt{2}p_T^2}&\left[\frac{1}{m_Z^2 s'}\left(u' S_4^{\mu\nu\rho\sigma} - t' S_7^{\mu\nu\rho\sigma}\right) + \frac{\left(m_Z^2 - p_T^2\right)}{2m_Z^2}\left(\frac{S_5^{\mu\nu\rho\sigma}}{u'} - \frac{S_6^{\mu\nu\rho\sigma}}{t'}\right)\right. \\ &\left. + \frac{1}{m_Z^2 s'}\left(S_{17}^{\mu\nu\rho\sigma} - S_{20}^{\mu\nu\rho\sigma} + \frac{u'}{t'}S_{18}^{\mu\nu\rho\sigma} - \frac{t'}{u'}S_{19}^{\mu\nu\rho\sigma}\right)\right].\end{aligned} \tag{B.8}$$

The symmetric projectors are

$$\mathcal{P}_9^{\mu\nu\rho\sigma} = \frac{m_Z^2}{\sqrt{p_T^4+m_Z^4}}\left[\frac{1}{p_T^2 s'}\left(S_{17}^{\mu\nu\rho\sigma}+S_{20}^{\mu\nu\rho\sigma}\right)\right] \tag{B.9}$$

$$\mathcal{P}_{10}^{\mu\nu\rho\sigma} = \frac{\sqrt{p_T^4+m_Z^4}}{2p_T^2}\left[\frac{\left(m_Z^4-p_T^4\right)}{\left(m_Z^4+p_T^4\right)p_T^2 s'}\left(S_{17}^{\mu\nu\rho\sigma}+S_{20}^{\mu\nu\rho\sigma}\right)+\frac{1}{p_T^2 s'}\left(\frac{u'}{t'}S_{18}^{\mu\nu\rho\sigma}+\frac{t'}{u'}S_{19}^{\mu\nu\rho\sigma}\right)\right] \tag{B.10}$$

$$\mathcal{P}_{11}^{\mu\nu\rho\sigma} = \frac{m_Z^2}{\sqrt{p_T^4+m_Z^4}}\left[\frac{1}{s'}\left(S_{9}^{\mu\nu\rho\sigma}+S_{12}^{\mu\nu\rho\sigma}\right)+\frac{1}{p_T^2 s'}\left(S_{17}^{\mu\nu\rho\sigma}+S_{20}^{\mu\nu\rho\sigma}\right)\right] \tag{B.11}$$

$$\begin{aligned}\mathcal{P}_{12}^{\mu\nu\rho\sigma} = {}& \frac{\sqrt{p_T^4+m_Z^4}}{2p_T^2}\left[\frac{\left(m_Z^4-p_T^4\right)}{\left(m_Z^4+p_T^4\right)s'}\left(S_{9}^{\mu\nu\rho\sigma}+S_{12}^{\mu\nu\rho\sigma}\right)+\frac{1}{s'}\left(\frac{u'}{t'}S_{10}^{\mu\nu\rho\sigma}+\frac{t'}{u'}S_{11}^{\mu\nu\rho\sigma}\right)\right. \\ & \left.+\frac{\left(m_Z^4-p_T^4\right)}{\left(m_Z^4+p_T^4\right)p_T^2 s'}\left(S_{17}^{\mu\nu\rho\sigma}+S_{20}^{\mu\nu\rho\sigma}\right)+\frac{1}{p_T^2 s'}\left(\frac{u'}{t'}S_{18}^{\mu\nu\rho\sigma}+\frac{t'}{u'}S_{19}^{\mu\nu\rho\sigma}\right)\right]\end{aligned} \tag{B.12}$$

$$\mathcal{P}_{13}^{\mu\nu\rho\sigma} = \frac{m_Z}{\sqrt{2}p_T}\left[\frac{S_{13}^{\mu\nu\rho\sigma}}{u'}+\frac{S_{16}^{\mu\nu\rho\sigma}}{t'}-\frac{1}{p_T^2 s'}\left(S_{17}^{\mu\nu\rho\sigma}+S_{20}^{\mu\nu\rho\sigma}\right)-\frac{1}{p_T^2 s'}\left(\frac{u'}{t'}S_{18}^{\mu\nu\rho\sigma}+\frac{t'}{u'}S_{19}^{\mu\nu\rho\sigma}\right)\right] \tag{B.13}$$

$$\begin{aligned}\mathcal{P}_{14}^{\mu\nu\rho\sigma} = {}& \frac{m_Z^2}{\sqrt{2}p_T^2}\left[\frac{\left(m_Z^2-p_T^2\right)}{2m_Z^2}\left(\frac{S_{13}^{\mu\nu\rho\sigma}}{u'}+\frac{S_{16}^{\mu\nu\rho\sigma}}{t'}\right)+\frac{1}{m_Z^2 s'}\left(u'S_{14}^{\mu\nu\rho\sigma}+t'S_{15}^{\mu\nu\rho\sigma}\right)\right. \\ & \left.-\frac{1}{p_T^2 s'}\left(S_{17}^{\mu\nu\rho\sigma}+S_{20}^{\mu\nu\rho\sigma}+\frac{u'}{t'}S_{18}^{\mu\nu\rho\sigma}+\frac{t'}{u'}S_{19}^{\mu\nu\rho\sigma}\right)\right]\end{aligned} \tag{B.14}$$

$$\begin{aligned}\mathcal{P}_{15}^{\mu\nu\rho\sigma} = {}& \frac{\sqrt{2}m_Z^3}{p_T(p_T^2+m_Z^2)}\left[\frac{1}{m_Z^2 s'}\left(u'S_{4}^{\mu\nu\rho\sigma}+t'S_{7}^{\mu\nu\rho\sigma}\right)\right. \\ & \left.+\frac{\left(m_Z^2+p_T^2\right)}{2m_Z^2 p_T^2 s'}\left(S_{17}^{\mu\nu\rho\sigma}+S_{20}^{\mu\nu\rho\sigma}+\frac{u'}{t'}S_{18}^{\mu\nu\rho\sigma}+\frac{t'}{u'}S_{19}^{\mu\nu\rho\sigma}\right)\right]\end{aligned} \tag{B.15}$$

$$\begin{aligned}\mathcal{P}_{16}^{\mu\nu\rho\sigma} = {}& \frac{p_T^2+m_Z^2}{2\sqrt{2}p_T^2}\left[\frac{2m_Z^2}{s'p_T^2(p_T^2+m_Z^2)}\left(S_{17}^{\mu\nu\rho\sigma}+S_{20}^{\mu\nu\rho\sigma}+\frac{u'}{t'}S_{18}^{\mu\nu\rho\sigma}+\frac{t'}{u'}S_{19}^{\mu\nu\rho\sigma}\right)\right. \\ & \left.-\frac{2\left(p_T^2-m_Z^2\right)}{\left(m_Z^2+p_T^2\right)^2 s'}\left(u'S_{4}^{\mu\nu\rho\sigma}+t'S_{7}^{\mu\nu\rho\sigma}\right)+\frac{S_{5}^{\mu\nu\rho\sigma}}{u'}+\frac{S_{6}^{\mu\nu\rho\sigma}}{t'}\right]\end{aligned} \tag{B.16}$$

$$\begin{aligned}\mathcal{P}_{17}^{\mu\nu\rho\sigma} = {}& \frac{p_T^2+2m_Z^2}{2m_Z^2}\left\{\frac{m_Z^2}{2m_Z^2+p_T^2}\left(S_{2}^{\mu\nu\rho\sigma}+S_{3}^{\mu\nu\rho\sigma}\right)-\frac{m_Z^2}{(p_T^2+2m_Z^2)s'p_T^2}\left(u'S_{4}^{\mu\nu\rho\sigma}+t'S_{7}^{\mu\nu\rho\sigma}\right)\right. \\ & -\frac{\left(m_Z^2+p_T^2\right)m_Z^2}{p_T^2\left(2m_Z^2+p_T^2\right)}\left[\frac{S_{5}^{\mu\nu\rho\sigma}}{2u'}+\frac{S_{6}^{\mu\nu\rho\sigma}}{2t'}-\frac{S_{13}^{\mu\nu\rho\sigma}}{2u'}-\frac{S_{16}^{\mu\nu\rho\sigma}}{2t'}+\frac{1}{p_T^2 s'}\left(S_{17}^{\mu\nu\rho\sigma}+S_{20}^{\mu\nu\rho\sigma}\right.\right. \\ & \left.\left.\left.+\frac{u'}{t'}S_{18}^{\mu\nu\rho\sigma}+\frac{t'}{u'}S_{19}^{\mu\nu\rho\sigma}\right)\right]+\frac{m_Z^2}{p_T^2 s'\left(2m_Z^2+p_T^2\right)}\left(u'S_{14}^{\mu\nu\rho\sigma}+t'S_{15}^{\mu\nu\rho\sigma}\right)\right\}\end{aligned} \tag{B.17}$$

$$\begin{aligned}
\mathcal{P}_{18}^{\mu\nu\rho\sigma} = & \frac{S_8^{\mu\nu\rho\sigma}}{p_T^2} - \frac{\left(m_Z^2+p_T^2\right)}{2p_T^4 s'}\left(S_{17}^{\mu\nu\rho\sigma}+S_{20}^{\mu\nu\rho\sigma}\right) + \frac{u' \ \left(-m_Z^4+p_T^4-2p_T^2(s'-t'+u')\right) S_{18}^{\mu\nu\rho\sigma}}{2p_T^4 \ \left(m_Z^2+p_T^2\right) s't'} \\
& - \frac{t' \ \left(m_Z^4-p_T^4+2p_T^2(s'+t'-u')\right) S_{19}^{\mu\nu\rho\sigma}}{2p_T^4 \ \left(m_Z^2+p_T^2\right) s' \ u'}.
\end{aligned} \tag{B.18}$$

Finally, we include the last two projectors, which have a zero norm in $D=4$ dimensions.

$$\begin{aligned}
\mathcal{P}_{19}^{\mu\nu\rho\sigma} = & S_1^{\mu\nu\rho\sigma} - \frac{S_2^{\mu\nu\rho\sigma}}{2} - \frac{S_3^{\mu\nu\rho\sigma}}{2} + \frac{1}{2 \ p_T^2 s'}\left(u' S_4^{\mu\nu\rho\sigma} + t' S_7^{\mu\nu\rho\sigma}\right) + \frac{\left(m_Z^2+p_T^2\right)}{4 \ p_T^2}\left(\frac{S_5^{\mu\nu\rho\sigma}}{u'}+\frac{S_6^{\mu\nu\rho\sigma}}{t'}\right) \\
& + \frac{S_8^{\mu\nu\rho\sigma}}{p_T^2} - \frac{\left(m_Z^2+p_T^2\right)}{2p_T^2 s'}\left(S_9^{\mu\nu\rho\sigma}+S_{12}^{\mu\nu\rho\sigma}\right) + \frac{u' \ \left(-m_Z^4+p_T^4-2p_T^2(s'-t'+u')\right) S_{10}^{\mu\nu\rho\sigma}}{2p_T^2 \ \left(m_Z^2+p_T^2\right) s't'} \\
& - \frac{t' \ \left(m_Z^4-p_T^4+2p_T^2(s'+t'-u')\right) S_{11}^{\mu\nu\rho\sigma}}{2p_T^2 \ \left(m_Z^2+p_T^2\right) s' \ u'} - \frac{\left(m_Z^2+p_T^2\right)}{4p_T^2}\left(\frac{S_{13}^{\mu\nu\rho\sigma}}{u'}+\frac{S_{16}^{\mu\nu\rho\sigma}}{t'}\right) \\
& - \frac{1}{2p_T^2 s'}\left(u' S_{14}^{\mu\nu\rho\sigma} + t' \ S_{15}^{\mu\nu\rho\sigma}\right) + \frac{\left(m_Z^2+p_T^2-s'+t'-u'\right) u' S_{18}^{\mu\nu\rho\sigma}}{p_T^2\left(m_Z^2+p_T^2\right) \ s't'} \\
& + \frac{t' \ \left(m_Z^2+p_T^2-s'-t'+u'\right) \ S_{19}^{\mu\nu\rho\sigma}}{p_T^2\left(m_Z^2+p_T^2\right) s' \ u'}
\end{aligned} \tag{B.19}$$

$$\begin{aligned}
\mathcal{P}_{20}^{\mu\nu\rho\sigma} = & \frac{1}{2m_Z^2+p_T^2}\left[S_3^{\mu\nu\rho\sigma} - S_2^{\mu\nu\rho\sigma} - \frac{1}{p_T^2 s'}\left(u' S_4^{\mu\nu\rho\sigma} - t' S_7^{\mu\nu\rho\sigma} + u' S_{14}^{\mu\nu\rho\sigma} - t' S_{15}^{\mu\nu\rho\sigma}\right)\right. \\
& \left. - \frac{\left(m_Z^2+p_T^2\right)}{2p_T^2}\left(\frac{S_5^{\mu\nu\rho\sigma}}{u'} - \frac{S_6^{\mu\nu\rho\sigma}}{t'} + \frac{S_{13}^{\mu\nu\rho\sigma}}{u'} - \frac{S_{16}^{\mu\nu\rho\sigma}}{t'}\right)\right]
\end{aligned} \tag{B.20}$$

The form factors $\mathcal{A}_i$ associated to the above projectors can be expressed in terms of the form factors f_i defined in eq.(2.8) of ref. [36] via the following relations

$$\mathcal{A}_1 = 0 \tag{B.21}$$

$$\begin{aligned}\mathcal{A}_2 = \frac{p_T^2}{m_Z^2}\Bigg[&\frac{2(t'-u')}{\left(m_Z^2+p_T^2\right)}\left(p_T^2 f_8 - f_1\right) + s' p_T^2\left(\frac{u'}{t'}f_{19} - \frac{t'}{u'}f_{18}\right)\\ &+ 2t' f_4 - 2u' f_5 + 2t' f_6 - 2u' f_7 + \frac{s't'}{u'}f_{10} - \frac{s'u'}{t'}f_{11}\Bigg]\end{aligned} \tag{B.22}$$

$$\mathcal{A}_3 = \frac{p_T^2}{m_Z^2}\left[f_3 - f_2 + \frac{\left(m_Z^2 - p_T^2\right)s'}{2}\left(\frac{f_7}{t'} - \frac{f_4}{u'}\right) + u' f_5 - t' f_6\right] \tag{B.23}$$

$$\mathcal{A}_4 = 0 \tag{B.24}$$

$$\mathcal{A}_5 = \frac{p_T^2}{m_Z^2}\left[\frac{2(t'-u')}{\left(m_Z^2+p_T^2\right)}f_1 + \frac{s'u'}{t'}f_{11} - \frac{s't'}{u'}f_{10}\right] \tag{B.25}$$

$$\mathcal{A}_6 = \frac{p_T^2}{m_Z^2}\left[f_3 - f_2 + t' f_4 - u' f_7 + \frac{\left(m_Z^2 - p_T^2\right)s'}{2}\left(\frac{f_6}{u'} - \frac{f_5}{u'}\right)\right] \tag{B.26}$$

$$\mathcal{A}_7 = \frac{p_T^2}{m_Z^2}\left[f_3 - f_2 + \frac{\left(3s' m_Z^2 + p_T^2 s' - 2\left(u' m_Z^2 + t'\left(m_Z^2 + u'\right)\right)\right)p_T^2}{4m_Z^2}\left(\frac{f_5}{t'} - \frac{f_6}{u'}\right)\right] \tag{B.27}$$

$$\mathcal{A}_8 = \frac{p_T^2}{m_Z^2}\left[f_3 - f_2\frac{\left(3s' m_Z^2 + p_T^2 s' - 2\left(u' m_Z^2 + t'\left(m_Z^2 + u'\right)\right)\right)p_T^2}{4m_Z^2}\left(\frac{f_4}{u'} - \frac{f_7}{t'}\right)\right] \tag{B.28}$$

$$\begin{aligned}\mathcal{A}_9 = \frac{1}{m_Z^4}\Bigg[&-2p_T^4\left(t' f_4 + u' f_5 + t' f_6 + u' f_7\right) - \left(m_Z^2 + p_T^2\right)p_T^2\left(f_2 + f_3\right)\\ &- \frac{\left(s'(m_Z^2+p_T^2)(m_Z^2-s') + 2m_Z^2(t'^2+u'^2)\right)}{s'}\left(p_T^2 f_8 - f_1\right) - s'\left(m_Z^4 + p_T^4\right)\left(f_9 - p_T^2 f_{20}\right)\\ &+ \frac{2\left(u' m_Z^2 + t'\left(m_Z^2+u'\right)\right)}{s'}\left(p_T^2\left(t'^2 f_{18} + u'^2 f_{19}\right) - \left(t'^2 f_{10} + u'^2 f_{11}\right)\right)\Bigg]\end{aligned} \tag{B.29}$$

$$\begin{aligned}\mathcal{A}_{10} = \frac{2p_T^2}{\left(m_Z^4 + p_T^4\right)}\Bigg[&s' p_T^2\left(p_T^2\left(\frac{t'}{u'}f_{18} + \frac{u'}{t'}f_{19}\right) - \left(\frac{t'}{u'}f_{10} + \frac{u'}{t'}f_{11}\right)\right) - 2p_T^2\left(t' f_4 + u' f_5 + t' f_6 + u' f_7\right)\\ &+ \frac{\left(\left(s'^2 - t'^2 - u'^2\right)m_Z^2 + p_T^2\left(s'^2 + t'^2 + u'^2\right)\right)}{\left(m_Z^2 + p_T^2\right)s'}\left(f_8 p_T^2 - f_1\right) - \left(m_Z^2 + p_T^2\right)\left(f_2 + f_3\right)\Bigg]\end{aligned} \tag{B.30}$$

$$\begin{aligned}\mathcal{A}_{11} = \frac{1}{m_Z^4}\Bigg[&s'\left(m_Z^4 + p_T^4\right)f_9 + \frac{2\left(u' m_Z^2 + t'\left(m_Z^2 + u'\right)\right)}{s'}\left(t'^2 f_{10} + u'^2 f_{11}\right)\\ &- \frac{\left(2u'^2 m_Z^2 + s'\left(m_Z^2 + u'\right)\left(s' m_Z^2 + 2t'^2 + p_T^2 s'\right)\right)}{s'}f_1\Bigg]\end{aligned} \tag{B.31}$$

$$\mathcal{A}_{12} = \frac{2p_T^2}{\left(m_Z^4 + p_T^4\right)} \left[\frac{\left(\left(s'^2 - t'^2 - u'^2\right) m_Z^2 + p_T^2 \left(s'^2 + t'^2 + u'^2\right)\right)}{\left(m_Z^2 + p_T^2\right) s'} f_1 + p_T^2 s' \left(\frac{t'}{u'} f_{10} + \frac{u'}{t'} f_{11} \right) \right] \tag{B.32}$$

$$\mathcal{A}_{13} = \frac{p_T^2}{m_Z^2} \left[\frac{\left(m_Z^2 - p_T^2\right) s'}{2} \left(\frac{f_5}{t'} + \frac{f_6}{u'} \right) - \left(f_2 + f_3 + t' f_4 + u' f_7\right) \right] \tag{B.33}$$

$$\mathcal{A}_{14} = -\frac{p_T^2}{m_Z^2} \left[f_2 + f_3 + p_T^2 s' \left(\frac{f_5}{t'} + \frac{f_6}{u'} \right) \right] \tag{B.34}$$

$$\mathcal{A}_{15} = \frac{p_T^2}{2m_Z^4} \left[\left(m_Z^2 + p_T^2\right) \left(f_2 + f_3 + t' f_4 + u' f_7\right) - \left(m_Z^2 - p_T^2\right) \left(u' f_5 + t' f_6\right) \right] \tag{B.35}$$

$$\mathcal{A}_{16} = \frac{2p_T^2}{m_Z^2 + p_T^2} \left[f_2 + f_3 + \frac{2p_T^2}{m_Z^2 + p_T^2} \left(u' f_5 + t' f_6\right) \right] \tag{B.36}$$

$$\mathcal{A}_{17} = \frac{2m_Z^2}{2m_Z^2 + p_T^2} \left[\frac{\left(s'^2 \left(t'^2 + u'^2\right) - \left(t'^2 - u'^2\right)^2 \right)}{s'^3 \left(m_Z^2 + p_T^2\right)} f_1 + f_2 + f_3 \right] \tag{B.37}$$

$$\mathcal{A}_{18} = \frac{\left(m_Z^2 \left(2s'^2 - t'^2 - u'^2\right) + s'(s'(p_T^2 - s') + t'^2 + u'^2)\right)}{m_Z^2 s' \left(m_Z^2 + p_T^2\right)} \left(p_T^2 f_8 - f_1\right) \tag{B.38}$$

B.2 Analytical Results

Results for Double-Triangle Diagrams With reference to eq.(3.30), we present here the exact results for the double-triangle contributions to the $\mathcal{A}_i^{(1,\bowtie)}$ with $i = 1, \ldots, 18$. We keep the dependence of the final result on the mass of the bottom quark, m_b. We find

$$\mathcal{A}_1^{(1,\bowtie)} = 0 \tag{B.39}$$

$$\mathcal{A}_2^{(1,\bowtie)} = \frac{p_T \left(\left(m_Z^2 + 2t'\right) \ \Delta(t')^2 - (t' \leftrightarrow u')\right)}{32\sqrt{2} m_Z \ \left(m_Z^2 + p_T^2\right)} \tag{B.40}$$

$$\mathcal{A}_3^{(1,\bowtie)} = -\frac{p_T^3 \left(u' \Delta(t')^2 - (t' \leftrightarrow u')\right)}{16 \ \sqrt{2} m_Z \left(m_Z^2 + p_T^2\right)^2} \tag{B.41}$$

$$\mathcal{A}_4^{(1,\bowtie)} = 0 \tag{B.42}$$

$$\mathcal{A}_5^{(1,\bowtie)} = -\frac{p_T \ \left(t' \ \Delta(t')^2 - (t' \leftrightarrow u')\right)}{16\sqrt{2} m_Z \ \left(m_Z^2 + p_T^2\right)} \tag{B.43}$$

$$\mathcal{A}_6^{(1,\bowtie)} = -\frac{p_T \left(\left(m_Z^2 + 2t'\right) u'^2 \ \Delta(t')^2 - (t' \leftrightarrow u')\right)}{16\sqrt{2} m_Z \ \left(m_Z^2 + p_T^2\right)^2 s'} \tag{B.44}$$

$$\mathcal{A}_7^{(1,\bowtie)} = \frac{\left(s' \ p_T^2 + t'^2\right) u'^2 \ \Delta(t')^2 - (t' \leftrightarrow u')}{16\sqrt{2} \ \left(m_Z^2 + p_T^2\right)^2 s'^2} \tag{B.45}$$

$$\mathcal{A}_8^{(1,\bowtie)} = \frac{u' \left(t'(m_Z^2 + p_T^2) - 2s' p_T^2\right) \Delta(t')^2 - (t' \leftrightarrow u')}{32\sqrt{2} \ \left(m_Z^2 + p_T^2\right)^2 \ s'} \tag{B.46}$$

$$\mathcal{A}_9^{(1,\bowtie)} = \frac{\left(m_Z^2 - p_T^2\right) \left(\left(m_Z^2 + 2t'\right) \ \Delta(t')^2 + (t' \leftrightarrow u')\right)}{64 m_Z^2 \ \sqrt{m_Z^4 + p_T^4}} \tag{B.47}$$

$$\mathcal{A}_{10}^{(1,\bowtie)} = -\frac{p_T^2 \ \left(\left(m_Z^2 + 2t'\right) \ \Delta(t')^2 + (t' \leftrightarrow u')\right)}{32 \left(m_Z^2 + p_T^2\right) \ \sqrt{m_Z^4 + p_T^4}} \tag{B.48}$$

$$\mathcal{A}_{11}^{(1,\bowtie)} = \frac{u' \left(m_Z^2 + 2 \ t'\right) \left(2s' \ m_Z^2 + \left(m_Z^2 + p_T^2\right) (t' + 2 \ u')\right) \Delta(t')^2 + (t' \leftrightarrow u')}{32 m_Z^2 \ \left(m_Z^2 + p_T^2\right) \sqrt{m_Z^4 + p_T^4} \ s'} \tag{B.49}$$

$$\mathcal{A}_{12}^{(1,\bowtie)} = -\frac{\left(s' m_Z^4 + 4 p_T^2 s' \ m_Z^2 + 3 p_T^4 s' + 4 p_T^2 \ \left(t'^2 + u'^2\right)\right) \ \left(\Delta(t')^2 + \Delta(u')^2\right)}{64 \ \left(m_Z^2 + p_T^2\right) \sqrt{m_Z^4 + p_T^4} \ s'} \tag{B.50}$$

$$\mathcal{A}_{13}^{(1,\bowtie)} = \frac{p_T \left(\left(m_Z^2 + 2t'\right) \ u'^2 \Delta(t')^2 + (t' \leftrightarrow u')\right)}{16\sqrt{2} m_Z \ \left(m_Z^2 + p_T^2\right)^2 s'} \tag{B.51}$$

$$\mathcal{A}_{14}^{(1,\bowtie)} = -\frac{\left(s'\ p_T^2 + t'^2\right) u'^2\ \Delta(t')^2 + (t' \leftrightarrow u')}{16\sqrt{2}\ \left(m_Z^2 + p_T^2\right)^2 s'^2} \tag{B.52}$$

$$\mathcal{A}_{15}^{(1,\bowtie)} = -\frac{p_T\ \left(\left(m_Z^2 + 2t'\right) u'^2\ \Delta(t')^2 + (t' \leftrightarrow u')\right)}{16\sqrt{2} m_Z\ \left(m_Z^2 + p_T^2\right)^2 s'} \tag{B.53}$$

$$\mathcal{A}_{16}^{(1,\bowtie)} = \frac{\left(s'\ p_T^2 + t'^2\right) u'^2\ \Delta(t')^2 + (t' \leftrightarrow u')}{16\sqrt{2}\ \left(m_Z^2 + p_T^2\right)^2 s'^2} \tag{B.54}$$

$$\mathcal{A}_{17}^{(1,\bowtie)} = 0 \tag{B.55}$$

$$\mathcal{A}_{18}^{(1,\bowtie)} = \frac{1}{64}\left(\left(\frac{s'\ p_T^2}{t'^2} + 1\right)\ \Delta(t')^2 + (t' \leftrightarrow u')\right) \tag{B.56}$$

where

$$\Delta(x) = F(x, m_t) - F(x, m_b) \tag{B.57}$$

and

$$\begin{aligned} F(x, M) = \frac{m_Z^2}{x}&\left[B_0(2x + m_Z^2, M^2, M^2) - B_0(m_Z^2, M^2, M^2)\right] \\ &+ 4M^2 C_0(0, m_Z^2, 2x + m_Z^2, M^2, M^2, M^2) + 2 \end{aligned} \tag{B.58}$$

Results for Triangle Diagrams at NLO With reference to eq.(3.30), we present here the exact results for the two-loop one-particle-irreducible triangle contributions to the NLO form factors. We obtain

$$\mathcal{A}_1^{(1,\triangle)} = 0 \tag{B.59}$$

$$\mathcal{A}_2^{(1,\triangle)} = \frac{p_T^2(\hat{t}-\hat{u})}{m_Z^2(p_T^2+m_Z^2)}\frac{\hat{s}}{\hat{s}-m_H^2}\left(C_F\mathcal{F}_{1/2}^{(2l)} + C_A\mathcal{G}_{1/2}^{(2l,CA)}\right) \tag{B.60}$$

$$\mathcal{A}_3^{(1,\triangle)} = 0 \tag{B.61}$$

$$\mathcal{A}_4^{(1,\triangle)} = 0 \tag{B.62}$$

$$\mathcal{A}_5^{(1,\triangle)} = -\frac{p_T^2(\hat{t}-\hat{u})}{m_Z^2(p_T^2+m_Z^2)}\frac{\hat{s}}{\hat{s}-m_H^2}\left(C_F\mathcal{F}_{1/2}^{(2l)} + C_A\mathcal{G}_{1/2}^{(2l,CA)}\right) \tag{B.63}$$

$$\mathcal{A}_6^{(1,\triangle)} = 0 \tag{B.64}$$

$$\mathcal{A}_7^{(1,\triangle)} = 0 \tag{B.65}$$

$$\mathcal{A}_8^{(1,\triangle)} = 0 \tag{B.66}$$

$$\mathcal{A}_9^{(1,\triangle)} = \frac{(\hat{s}(p_T^2-m_Z^2)+2m_Z^2(p_T^2+m_Z^2)}{2m_Z^4}\frac{\hat{s}}{\hat{s}-m_H^2}\left(C_F\mathcal{F}_{1/2}^{(2l)} + C_A\mathcal{G}_{1/2}^{(2l,CA)}\right) \tag{B.67}$$

$$\mathcal{A}_{10}^{(1,\triangle)} = \frac{2p_T^2(p_T^2\hat{s}+m_Z^4-p_T^4)}{(p_T^2+m_Z^2)(p_T^4+m_Z^4)}\frac{\hat{s}}{\hat{s}-m_H^2}\left(C_F\mathcal{F}_{1/2}^{(2l)} + C_A\mathcal{G}_{1/2}^{(2l,CA)}\right) \tag{B.68}$$

$$\mathcal{A}_{11}^{(1,\triangle)} = -\frac{(\hat{s}(p_T^2-m_Z^2)+2m_Z^2(p_T^2+m_Z^2)}{2m_Z^4}\frac{\hat{s}}{\hat{s}-m_H^2}\left(C_F\mathcal{F}_{1/2}^{(2l)} + C_A\mathcal{G}_{1/2}^{(2l,CA)}\right) \tag{B.69}$$

$$\mathcal{A}_{12}^{(1,\triangle)} = -\frac{2p_T^2(p_T^2\hat{s}+m_Z^4-p_T^4)}{(p_T^2+m_Z^2)(p_T^4+m_Z^4)}\frac{\hat{s}}{\hat{s}-m_H^2}\left(C_F\mathcal{F}_{1/2}^{(2l)} + C_A\mathcal{G}_{1/2}^{(2l,CA)}\right) \tag{B.70}$$

$$\mathcal{A}_{13}^{(1,\triangle)} = 0 \tag{B.71}$$

$$\mathcal{A}_{14}^{(1,\triangle)} = 0 \tag{B.72}$$

$$\mathcal{A}_{15}^{(1,\triangle)} = 0 \tag{B.73}$$

$$\mathcal{A}_{16}^{(1,\triangle)} = 0 \tag{B.74}$$

$$\mathcal{A}_{17}^{(1,\triangle)} = -\frac{2m_Z^2}{p_T^2+2m_Z^2}\frac{\hat{s}}{\hat{s}-m_H^2}\left(C_F\mathcal{F}_{1/2}^{(2l)} + C_A\mathcal{G}_{1/2}^{(2l,CA)}\right) \tag{B.75}$$

$$\mathcal{A}_{18}^{(1,\triangle)} = \frac{\hat{s}}{\hat{s}-m_H^2}\left(C_F\mathcal{F}_{1/2}^{(2l)} + C_A\mathcal{G}_{1/2}^{(2l,CA)}\right) \tag{B.76}$$

where the functions $\mathcal{F}_{1/2}^{(2l)}$ and $\mathcal{G}_{1/2}^{(2l,CA)}$ are defined in eqs. (2.11) and (3.8) in ref. [77].

B.3 Additional Plots

In chap. 3 we presented the results of the p_T expansion by discussing the form factor $\mathcal{A}_9$ in detail. In this section we summarize the results for all the other form factors contributing to the $gg \to ZZ$ amplitude. In fig. B.1 we show that $\mathcal{A}_9$ is indeed the form factor which gives the dominant contribution to the LO partonic cross section. While the contribution from $\mathcal{A}_9$ is significantly larger than the sum of the antisymmetric form factors for any value of M_{ZZ}, the other symmetric form factors are important in the region $M_{ZZ} < 400$ GeV.

In figs. B.2, B.3 and B.4 we show the absolute value of the relevant box form factors at LO for a partonic c.o.m. energy of 1600 GeV. We notice that the behavior of the form factors is very similar to the one of $\mathcal{A}_9^{(0,\Box)}$, discussed in Sec. 3.5, and to the behavior of the form factor contributing to $gg \to ZH$ (see app. A.4).

Finally, in figs. B.5, B.6 and B.7 we show the absolute value of all the relevant $\mathcal{A}_i^{(1,\Box)}$: as in the case of $gg \to ZH$, the $\mathcal{O}(p_T^2)$ and the $\mathcal{O}(p_T^4)$ results are always in agreement for $p_T \lesssim 200$ GeV, but begin to diverge for larger p_T. However, we expect that the $\mathcal{O}(p_T^4)$ result can still be accurate for $p_T \lesssim 300$ GeV.

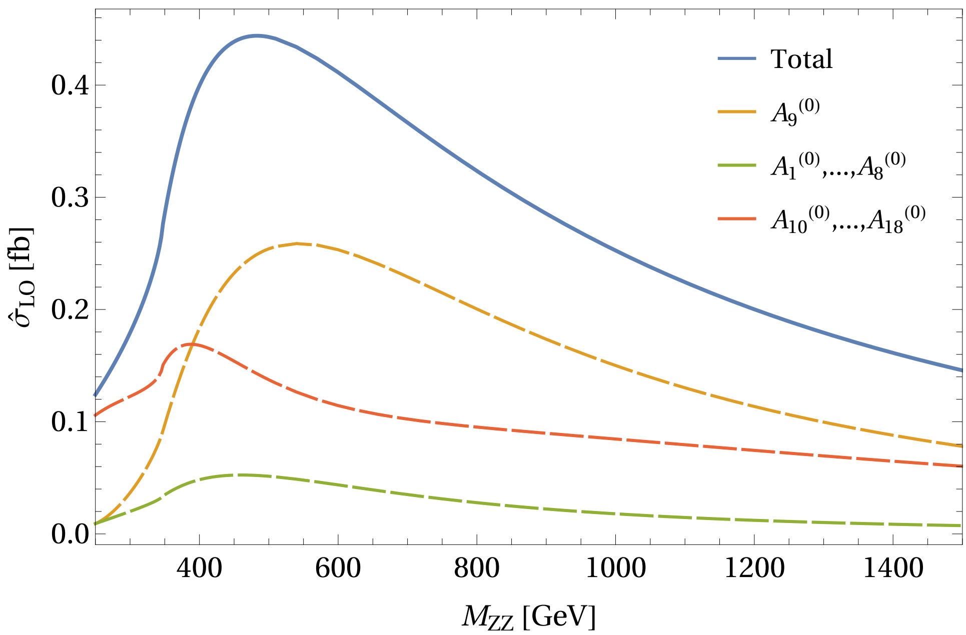

Figure B.1: Contributions to the LO partonic cross section from the various form factors $\mathcal{A}_i^{(0)}$, shown as dashed lines: the contributions from $\mathcal{A}_9^{(0)}$ (yellow) is shown separately, while the sum of the contributions from the antisymmetric form factors, $\mathcal{A}_i^{(0)}$ with $i = 1, \ldots, 8$ and from the remaining symmetric form factors $\mathcal{A}_i^{(0)}$ with $i = 10, \ldots, 18$ are shown as a green and red line, respectively. The solid line represents the sum of all contributions.

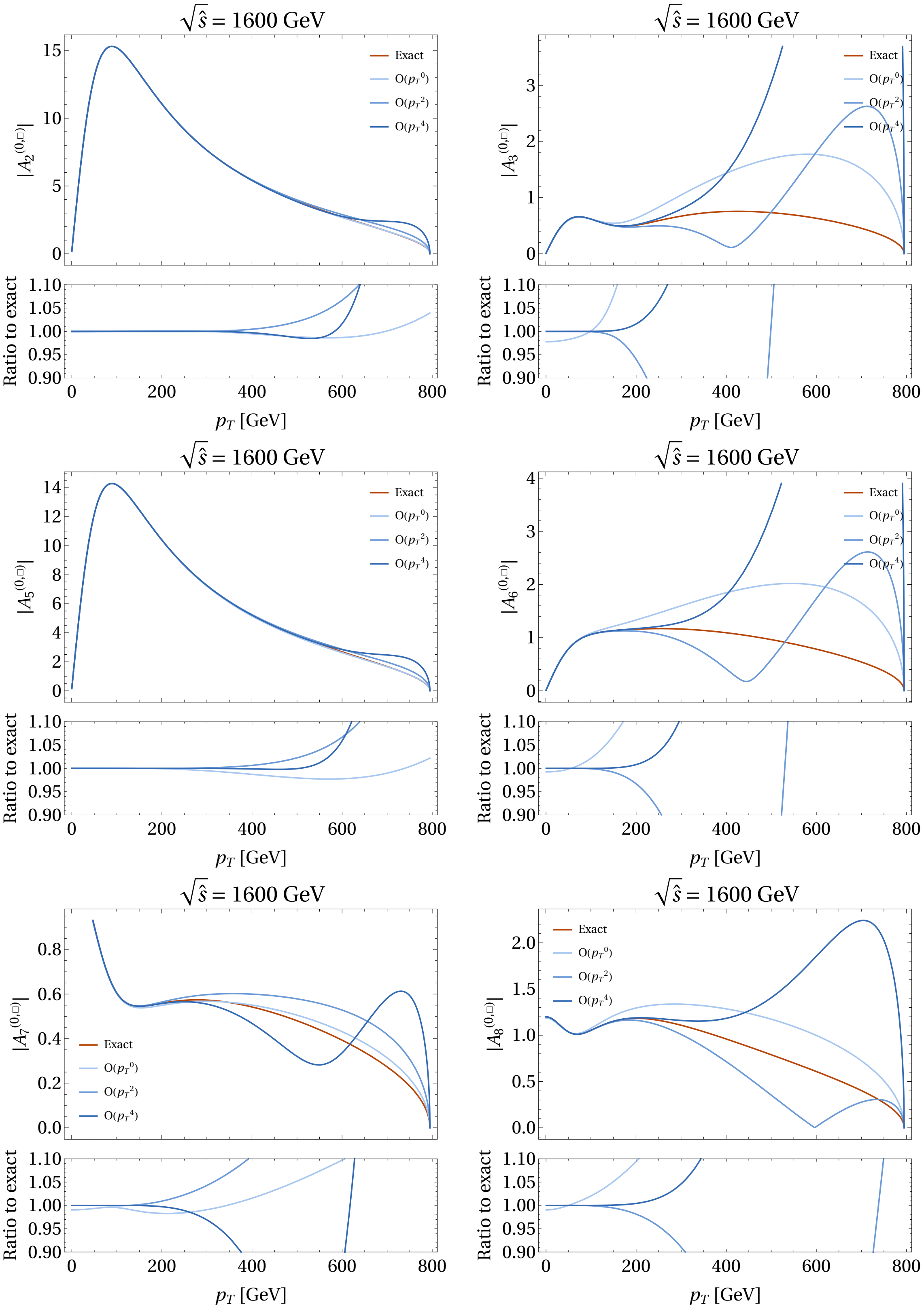

Figure B.2: Absolute value of the $\mathcal{A}_i^{(0,\square)}$ form factors for $i = 2, \ldots, 8$, for fixed $\sqrt{\hat{s}} = 1600$ GeV: the blue lines represent the first three orders of the expansion, while the brown line stands for the exact result. The bottom part of each graph shows the ratio of the various orders of the p_T expansion to the exact result.

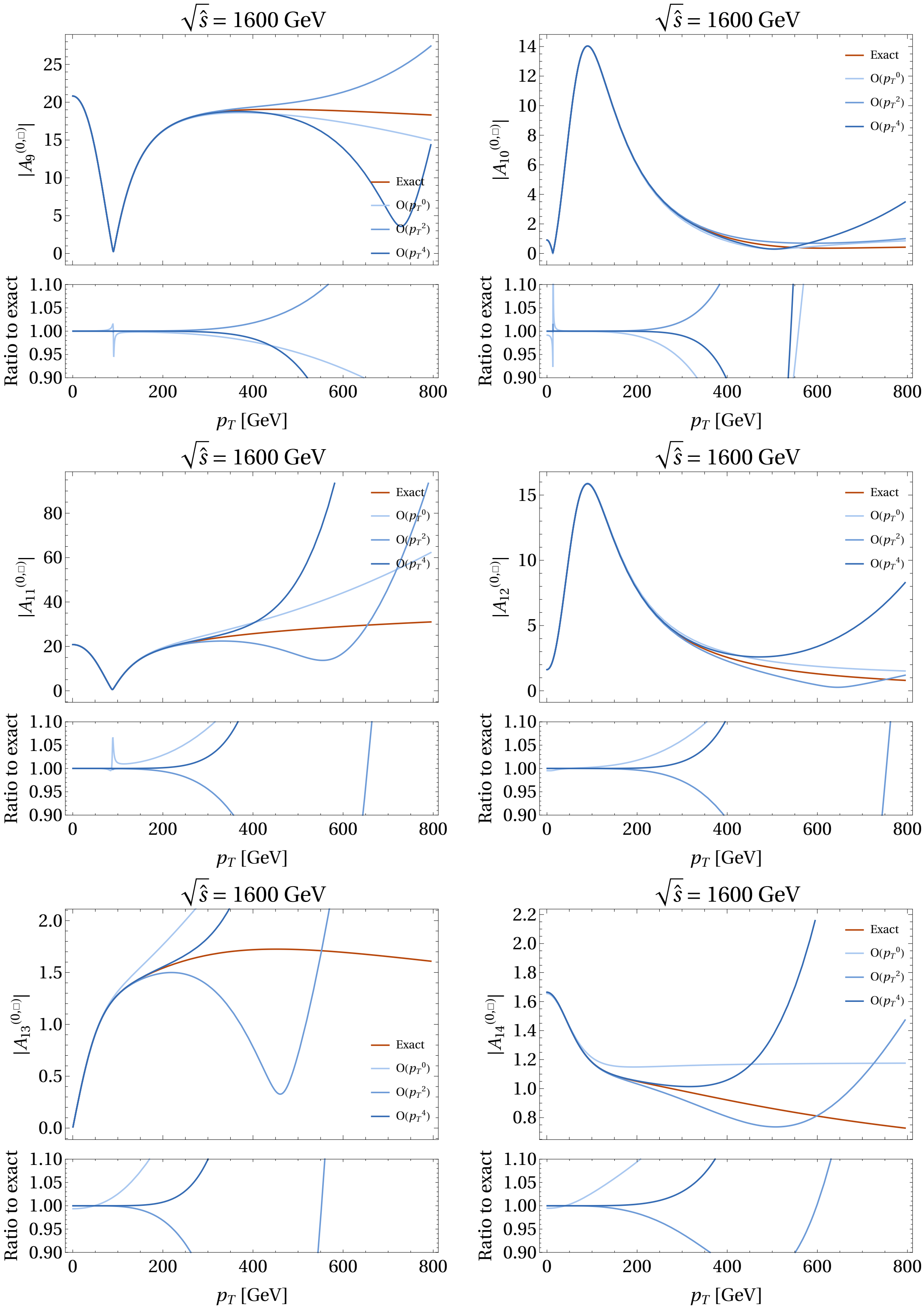

Figure B.3: Absolute value of the $\mathcal{A}_i^{(0,\Box)}$ form factors for $i = 9, \ldots, 14$, for fixed $\sqrt{\hat{s}} = 1600$ GeV: the blue lines represent the first three orders of the expansion, while the brown line stands for the exact result. The bottom part of each graph shows the ratio of the various orders of the p_T expansion to the exact result.

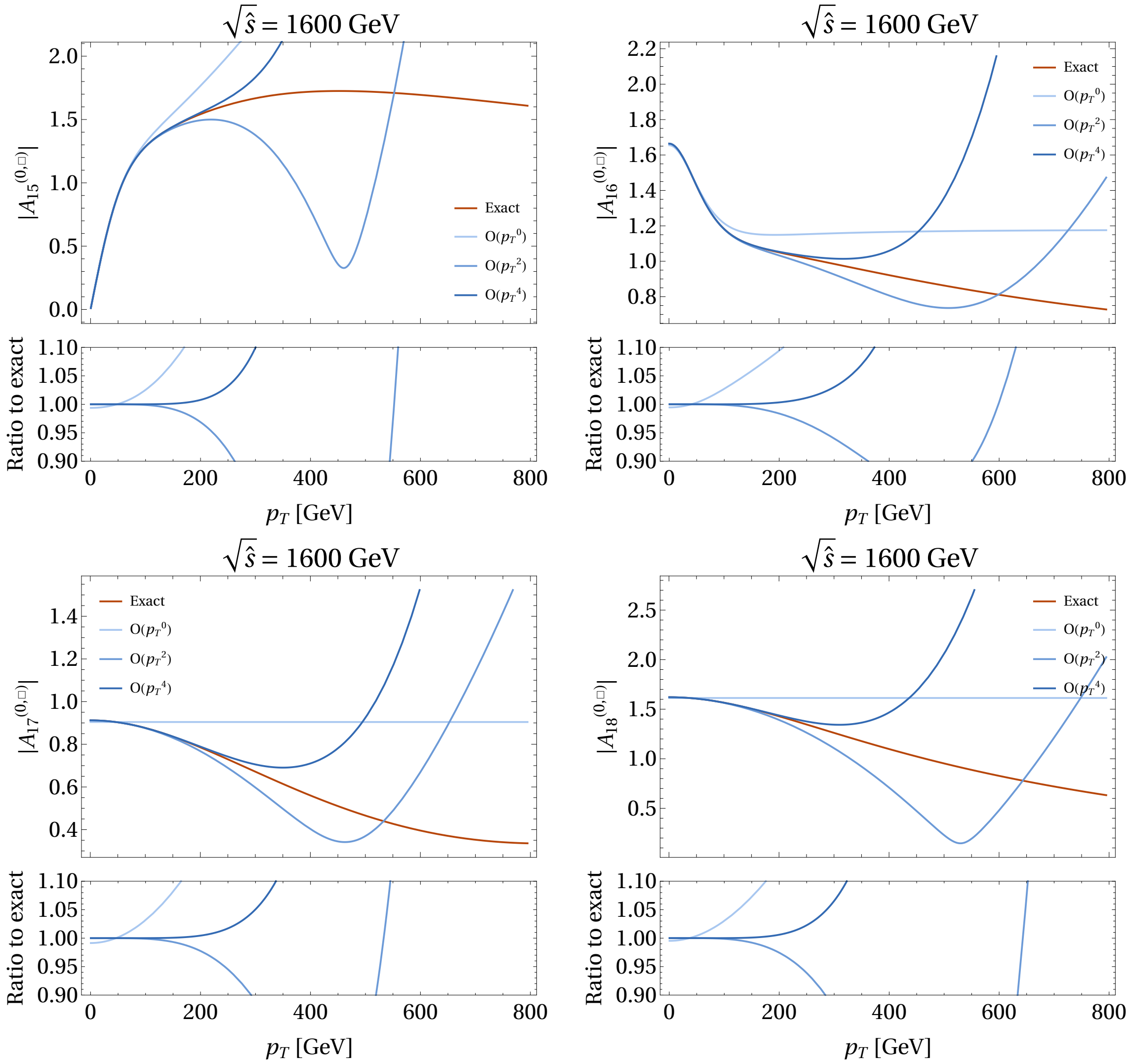

Figure B.4: Absolute value of the $\mathcal{A}_i^{(0,\square)}$ form factors for $i = 15, \ldots, 18$, for fixed $\sqrt{\hat{s}} = 1600$ GeV: the blue lines represent the first three orders of the expansion, while the brown line stands for the exact result. The bottom part of each graph shows the ratio of the various orders of the p_T expansion to the exact result.

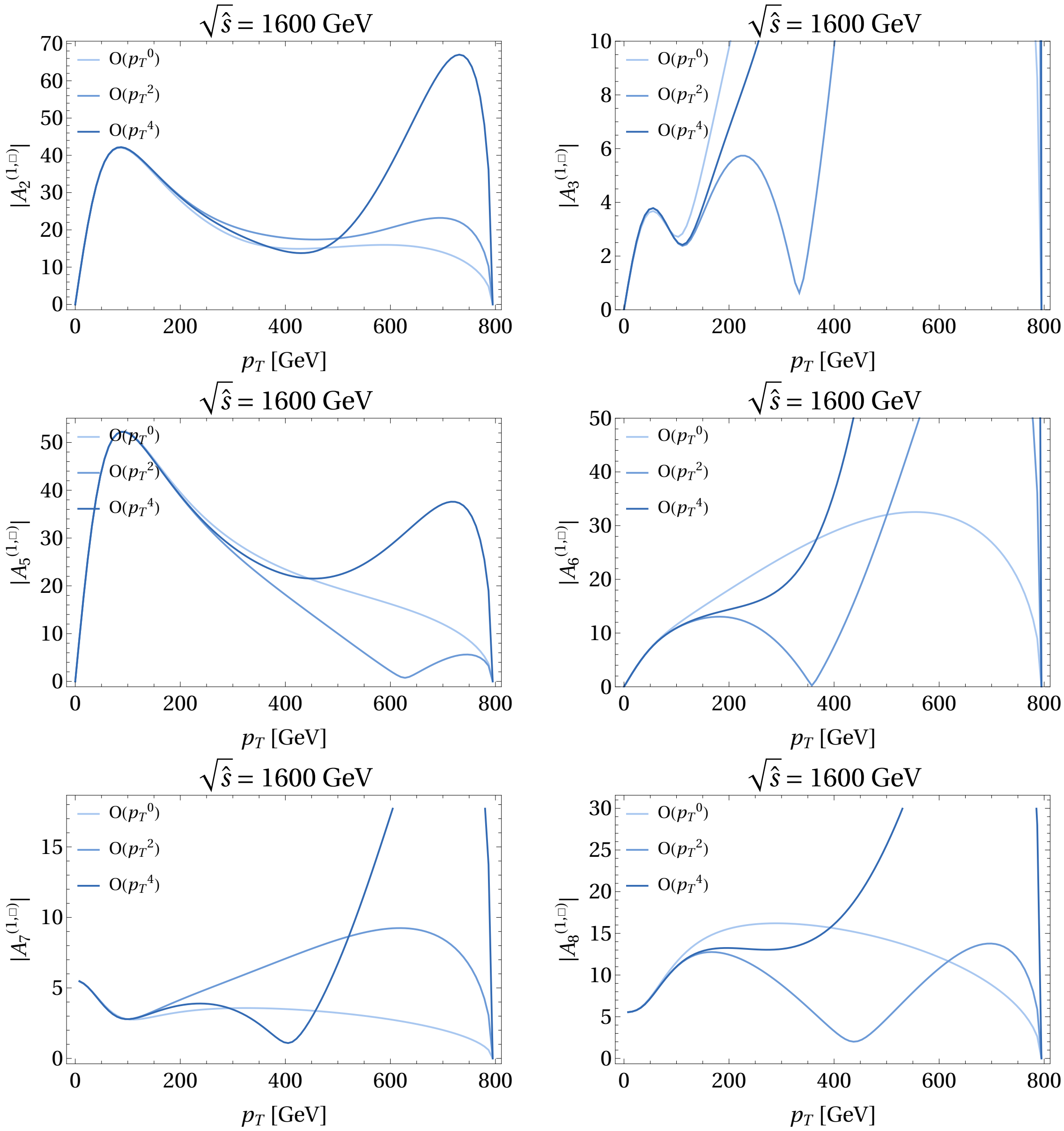

Figure B.5: Absolute value of the $\mathcal{A}_i^{(1,\square)}$ form factors with $i = 2, \ldots, 8$ for fixed $\sqrt{\hat{s}} = 1600$ GeV, shown as a function of p_T: the blue lines represent the first three orders of the p_T expansion.

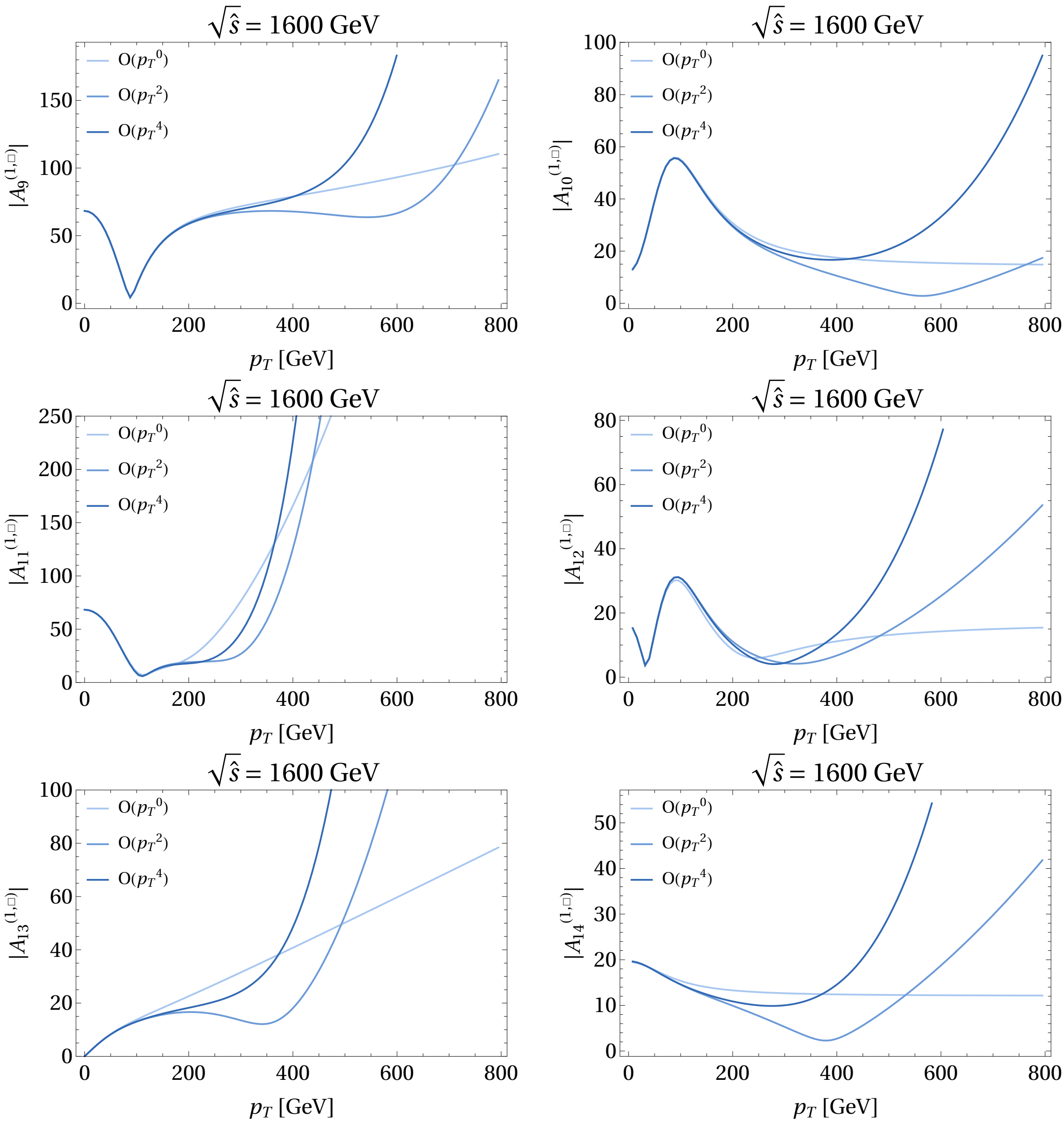

Figure B.6: Absolute value of the $\mathcal{A}_i^{(1,\Box)}$ form factors with $i = 9, \ldots, 14$ for fixed $\sqrt{\hat{s}} = 1600$ GeV, shown as a function of p_T: the blue lines represent the first three orders of the p_T expansion.

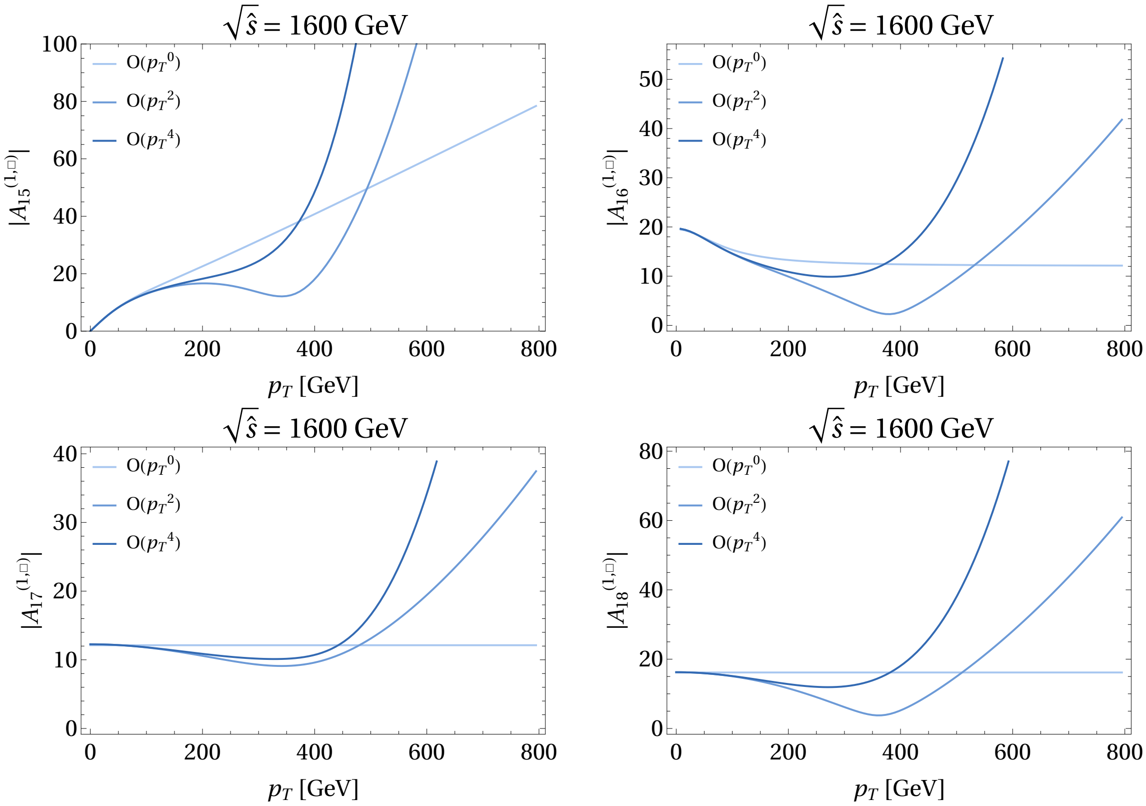

Figure B.7: Absolute value of the $\mathcal{A}_i^{(1,\square)}$ form factors with $i = 15, \ldots, 18$ for fixed $\sqrt{\hat{s}} = 1600$ GeV, shown as a function of p_T: the blue lines represent the first three orders of the p_T expansion.

Acknowledgments

First of all, I want to thank my supervisor, Giuseppe Degrassi, for giving me the opportunity to work on a very interesting project. I'm grateful that he could share his experience with me on many topics, from the vast realm of Higgs physics to all the subtleties involved in higher-order calculations.

I am thankful to Pier Paolo Giardino and Ramona Gröber, for their support and their patience in helping me to understand the many details of the calculations for the p_T expansion, as well as for the suggestions to improve the manuscript. I want to thank also Lina Alasfar and Luigi Bellafronte for their collaboration and discussions.

As the results presented in this thesis would not have been obtained without a device that could physically store the long intermediate expressions, I thank Roberto Franceschini for letting me use Uranio when my personal machine was running out of RAM.

I also want to thank all my Ph.D. colleagues from Roma Tre for contributing to the very friendly atmosphere in the department. In particular, I thank Davide Giusti, Simone Romiti and Massimo Guidi for interesting discussions about physics.

I wish to thank Alessandro and Livia, for all the (sometimes even physics-related) conversations, dinners and ice creams that alleviated the lockdown and the months afterwards. I'm glad that I could share these years in Rome with you. Special thanks also to Titi and Tari, for their unbounded madness.

Finally, I am grateful to my family for all their support and understanding throughout these years.

Bibliography

[1] **ATLAS** Collaboration, G. Aad *et al.*, "Observation of a new particle in the search for the Standard Model Higgs boson with the ATLAS detector at the LHC," *Phys. Lett. B* **716** (2012) 1–29, arXiv:1207.7214 [hep-ex].

[2] **CMS** Collaboration, S. Chatrchyan *et al.*, "Observation of a New Boson at a Mass of 125 GeV with the CMS Experiment at the LHC," *Phys. Lett. B* **716** (2012) 30–61, arXiv:1207.7235 [hep-ex].

[3] S. L. Glashow, "The renormalizability of vector meson interactions," *Nuclear Physics* **10** (1959) 107–117. https://www.sciencedirect.com/science/article/pii/0029558259901968.

[4] A. Salam and J. C. Ward, "Weak and electromagnetic interactions," *Nuovo Cim.* **11** (1959) 568–577.

[5] S. Weinberg, "A Model of Leptons," *Phys. Rev. Lett.* **19** (1967) 1264–1266.

[6] G. 't Hooft and M. J. G. Veltman, "Regularization and Renormalization of Gauge Fields," *Nucl. Phys. B* **44** (1972) 189–213.

[7] P. W. Higgs, "Broken symmetries and the masses of gauge bosons," *Phys. Rev. Lett.* **13** (Oct, 1964) 508–509. https://link.aps.org/doi/10.1103/PhysRevLett.13.508.

[8] P. W. Higgs, "Broken symmetries, massless particles and gauge fields," *Phys. Lett.* **12** (1964) 132–133.

[9] F. Englert and R. Brout, "Broken symmetry and the mass of gauge vector mesons," *Phys. Rev. Lett.* **13** (Aug, 1964) 321–323. https://link.aps.org/doi/10.1103/PhysRevLett.13.321.

[10] G. S. Guralnik, C. R. Hagen, and T. W. B. Kibble, "Global conservation laws and massless particles," *Phys. Rev. Lett.* **13** (Nov, 1964) 585–587. https://link.aps.org/doi/10.1103/PhysRevLett.13.585.

[11] T. W. B. Kibble, "Symmetry breaking in non-abelian gauge theories," *Phys. Rev.* **155** (Mar, 1967) 1554–1561. https://link.aps.org/doi/10.1103/PhysRev.155.1554.

[12] P. W. Anderson, "Plasmons, gauge invariance, and mass," *Phys. Rev.* **130** (Apr, 1963) 439–442. https://link.aps.org/doi/10.1103/PhysRev.130.439.

[13] "2020 Update of the European Strategy for Particle Physics (Brochure)," tech. rep., Geneva, 2020. http://cds.cern.ch/record/2721370.

[14] **ATLAS, CMS** Collaboration, G. Aad *et al.*, "Combined Measurement of the Higgs Boson Mass in pp Collisions at $\sqrt{s} = 7$ and 8 TeV with the ATLAS and CMS Experiments," *Phys. Rev. Lett.* **114** (2015) 191803, arXiv:1503.07589 [hep-ex].

[15] **ATLAS** Collaboration, G. Aad *et al.*, "Study of the spin and parity of the Higgs boson in diboson decays with the ATLAS detector," *Eur. Phys. J. C* **75** no. 10, (2015) 476, arXiv:1506.05669 [hep-ex]. [Erratum: Eur.Phys.J.C 76, 152 (2016)].

[16] **ATLAS Collaboration** Collaboration, "Projections for measurements of Higgs boson cross sections, branching ratios, coupling parameters and mass with the ATLAS detector at the HL-LHC," tech. rep., CERN, Geneva, Dec, 2018. http://cds.cern.ch/record/2652762.

[17] **ATLAS** Collaboration, G. Aad *et al.*, "Combined measurements of Higgs boson production and decay using up to 80 fb^{-1} of proton-proton collision data at $\sqrt{s} = 13$ TeV collected with the ATLAS experiment," *Phys. Rev. D* **101** no. 1, (2020) 012002, arXiv:1909.02845 [hep-ex].

[18] J. C. Collins, D. E. Soper, and G. F. Sterman, "Factorization of Hard Processes in QCD," *Adv. Ser. Direct. High Energy Phys.* **5** (1989) 1–91, arXiv:hep-ph/0409313.

[19] D. J. Gross and F. Wilczek, "Ultraviolet behavior of non-abelian gauge theories," *Phys. Rev. Lett.* **30** (Jun, 1973) 1343–1346. https://link.aps.org/doi/10.1103/PhysRevLett.30.1343.

[20] D. J. Gross and F. Wilczek, "Ultraviolet behavior of non-abelian gauge theories," *Phys. Rev. Lett.* **30** (Jun, 1973) 1343–1346. https://link.aps.org/doi/10.1103/PhysRevLett.30.1343.

[21] R. K. Ellis, W. J. Stirling, and B. R. Webber, *QCD and collider physics*, vol. 8. Cambridge University Press, 2, 2011.

[22] A. Denner and S. Dittmaier, "Electroweak Radiative Corrections for Collider Physics," *Phys. Rept.* **864** (2020) 1–163, arXiv:1912.06823 [hep-ph].

[23] L. Chen, "A prescription for projectors to compute helicity amplitudes in d dimensions," *The European Physical Journal C* **81** no. 5, (May, 2021) . http://dx.doi.org/10.1140/epjc/s10052-021-09210-9.

[24] T. Peraro and L. Tancredi, "Tensor decomposition for bosonic and fermionic scattering amplitudes," *Physical Review D* **103** no. 5, (Mar, 2021) . http://dx.doi.org/10.1103/PhysRevD.103.054042.

[25] K. G. Chetyrkin and F. V. Tkachov, "Integration by Parts: The Algorithm to Calculate beta Functions in 4 Loops," *Nucl. Phys. B* **192** (1981) 159–204.

[26] F. V. Tkachov, "A Theorem on Analytical Calculability of Four Loop Renormalization Group Functions," *Phys. Lett. B* **100** (1981) 65–68.

[27] S. Borowka, G. Heinrich, S. Jahn, S. P. Jones, M. Kerner, J. Schlenk, and T. Zirke, "pySecDec: a toolbox for the numerical evaluation of multi-scale integrals," *Comput. Phys. Commun.* **222** (2018) 313–326, arXiv:1703.09692 [hep-ph].

[28] L. Altenkamp, S. Dittmaier, R. V. Harlander, H. Rzehak, and T. J. Zirke, "Gluon-induced Higgs-strahlung at next-to-leading order QCD," *JHEP* **02** (2013) 078, arXiv:1211.5015 [hep-ph].

[29] K. Melnikov and M. Dowling, "Production of two Z-bosons in gluon fusion in the heavy top quark approximation," *Phys. Lett. B* **744** (2015) 43–47, arXiv:1503.01274 [hep-ph].

[30] J. Grigo, J. Hoff, and M. Steinhauser, "Higgs boson pair production: top quark mass effects at NLO and NNLO," *Nucl. Phys. B* **900** (2015) 412–430, arXiv:1508.00909 [hep-ph].

[31] G. Degrassi, P. P. Giardino, and R. Gröber, "On the two-loop virtual QCD corrections to Higgs boson pair production in the Standard Model," *Eur. Phys. J. C* **76** no. 7, (2016) 411, arXiv:1603.00385 [hep-ph].

[32] J. M. Campbell, R. K. Ellis, M. Czakon, and S. Kirchner, "Two loop correction to interference in $gg \to ZZ$," *JHEP* **08** (2016) 011, arXiv:1605.01380 [hep-ph].

[33] K. Kudashkin, K. Melnikov, and C. Wever, "Two-loop amplitudes for processes $gg \to Hg, qg \to Hq$ and $q\bar{q} \to Hg$ at large Higgs transverse momentum," *JHEP* **02** (2018) 135, arXiv:1712.06549 [hep-ph].

[34] J. Davies, G. Mishima, M. Steinhauser, and D. Wellmann, "Double-Higgs boson production in the high-energy limit: planar master integrals," *JHEP* **03** (2018) 048, arXiv:1801.09696 [hep-ph].

[35] J. Davies, G. Mishima, and M. Steinhauser, "Virtual corrections to $gg \to ZH$ in the high-energy and large-m_t limits," *JHEP* **03** (2021) 034, arXiv:2011.12314 [hep-ph].

[36] J. Davies, G. Mishima, M. Steinhauser, and D. Wellmann, "$gg \to ZZ$: analytic two-loop results for the low- and high-energy regions," *JHEP* **04** (2020) 024, arXiv:2002.05558 [hep-ph].

[37] X. Xu and L. L. Yang, "Towards a new approximation for pair-production and associated-production of the Higgs boson," *JHEP* **01** (2019) 211, arXiv:1810.12002 [hep-ph].

[38] G. Wang, X. Xu, Y. Xu, and L. L. Yang, "Next-to-leading order corrections for $gg \to ZH$ with top quark mass dependence," arXiv:2107.08206 [hep-ph].

[39] R. Bonciani, G. Degrassi, P. P. Giardino, and R. Gröber, "Analytical Method for Next-to-Leading-Order QCD Corrections to Double-Higgs Production," *Phys. Rev. Lett.* **121** no. 16, (2018) 162003, arXiv:1806.11564 [hep-ph].

[40] V. Ahrens, T. Becher, M. Neubert, and L. L. Yang, "Origin of the Large Perturbative Corrections to Higgs Production at Hadron Colliders," *Phys. Rev. D* **79** (2009) 033013, arXiv:0808.3008 [hep-ph].

[41] L. Alasfar, G. Degrassi, P. P. Giardino, R. Gröber, and M. Vitti, "Virtual corrections to $gg \to ZH$ via a transverse momentum expansion," *JHEP* **05** (2021) 168, arXiv:2103.06225 [hep-ph].

[42] J. M. Butterworth, A. R. Davison, M. Rubin, and G. P. Salam, "Jet substructure as a new Higgs search channel at the LHC," *Phys. Rev. Lett.* **100** (2008) 242001, arXiv:0802.2470 [hep-ph].

[43] **ATLAS** Collaboration, M. Aaboud *et al.*, "Observation of $H \to b\bar{b}$ decays and VH production with the ATLAS detector," *Phys. Lett. B* **786** (2018) 59–86, arXiv:1808.08238 [hep-ex].

[44] **CMS** Collaboration, A. M. Sirunyan *et al.*, "Observation of Higgs boson decay to bottom quarks," *Phys. Rev. Lett.* **121** no. 12, (2018) 121801, arXiv:1808.08242 [hep-ex].

[45] **ATLAS** Collaboration, G. Aad *et al.*, "Measurements of WH and ZH production in the $H \to b\bar{b}$ decay channel in pp collisions at 13 TeV with the ATLAS detector," *Eur. Phys. J. C* **81** no. 2, (2021) 178, arXiv:2007.02873 [hep-ex].

[46] T. Han and S. Willenbrock, "QCD correction to the p p —> W H and Z H total cross-sections," *Phys. Lett. B* **273** (1991) 167–172.

[47] O. Brein, A. Djouadi, and R. Harlander, "NNLO QCD corrections to the Higgs-strahlung processes at hadron colliders," *Phys. Lett. B* **579** (2004) 149–156, arXiv:hep-ph/0307206.

[48] G. Ferrera, M. Grazzini, and F. Tramontano, "Associated WH production at hadron colliders: a fully exclusive QCD calculation at NNLO," *Phys. Rev. Lett.* **107** (2011) 152003, arXiv:1107.1164 [hep-ph].

[49] M. C. Kumar, M. K. Mandal, and V. Ravindran, "Associated production of Higgs boson with vector boson at threshold N^{3}LO in QCD," *JHEP* **03** (2015) 037, arXiv:1412.3357 [hep-ph].

[50] M. L. Ciccolini, S. Dittmaier, and M. Kramer, "Electroweak radiative corrections to associated WH and ZH production at hadron colliders," *Phys. Rev. D* **68** (2003) 073003, arXiv:hep-ph/0306234.

[51] A. Denner, S. Dittmaier, S. Kallweit, and A. Muck, "Electroweak corrections to Higgs-strahlung off W/Z bosons at the Tevatron and the LHC with HAWK," *JHEP* **03** (2012) 075, arXiv:1112.5142 [hep-ph].

[52] C. Englert, M. McCullough, and M. Spannowsky, "Gluon-initiated associated production boosts Higgs physics," *Phys. Rev. D* **89** no. 1, (2014) 013013, arXiv:1310.4828 [hep-ph].

[53] S. Amoroso *et al.*, "Les Houches 2019: Physics at TeV Colliders: Standard Model Working Group Report," in *11th Les Houches Workshop on Physics at TeV Colliders: PhysTeV Les Houches*. 3, 2020. arXiv:2003.01700 [hep-ph].

[54] C. Englert, R. Rosenfeld, M. Spannowsky, and A. Tonero, "New physics and signal-background interference in associated $pp \to HZ$ production," *EPL* **114** no. 3, (2016) 31001, arXiv:1603.05304 [hep-ph].

[55] R. V. Harlander, S. Liebler, and T. Zirke, "Higgs Strahlung at the Large Hadron Collider in the 2-Higgs-Doublet Model," *JHEP* **02** (2014) 023, arXiv:1307.8122 [hep-ph].

[56] **LHC Higgs Cross Section Working Group** Collaboration, D. de Florian *et al.*, "Handbook of LHC Higgs Cross Sections: 4. Deciphering the Nature of the Higgs Sector," arXiv:1610.07922 [hep-ph].

[57] B. A. Kniehl, "Associated Production of Higgs and Z Bosons From Gluon Fusion in Hadron Collisions," *Phys. Rev. D* **42** (1990) 2253–2258.

[58] D. A. Dicus and C. Kao, "Higgs Boson - Z^0 Production From Gluon Fusion," *Phys. Rev. D* **38** (1988) 1008. [Erratum: Phys.Rev.D 42, 2412 (1990)].

[59] R. V. Harlander, A. Kulesza, V. Theeuwes, and T. Zirke, "Soft gluon resummation for gluon-induced Higgs Strahlung," *JHEP* **11** (2014) 082, arXiv:1410.0217 [hep-ph].

[60] A. Hasselhuhn, T. Luthe, and M. Steinhauser, "On top quark mass effects to $gg \to ZH$ at NLO," *JHEP* **01** (2017) 073, arXiv:1611.05881 [hep-ph].

[61] R. Harlander, J. Klappert, C. Pandini, and A. Papaefstathiou, "Exploiting the WH/ZH symmetry in the search for New Physics," *Eur. Phys. J. C* **78** no. 9, (2018) 760, arXiv:1804.02299 [hep-ph].

[62] B. Hespel, F. Maltoni, and E. Vryonidou, "Higgs and Z boson associated production via gluon fusion in the SM and the 2HDM," *JHEP* **06** (2015) 065, arXiv:1503.01656 [hep-ph].

[63] L. Chen, G. Heinrich, S. P. Jones, M. Kerner, J. Klappert, and J. Schlenk, "ZH production in gluon fusion: two-loop amplitudes with full top quark mass dependence," *JHEP* **03** (2021) 125, arXiv:2011.12325 [hep-ph].

[64] S. Laporta, "High precision calculation of multiloop Feynman integrals by difference equations," *Int. J. Mod. Phys. A* **15** (2000) 5087–5159, arXiv:hep-ph/0102033.

[65] R. N. Lee, "LiteRed 1.4: a powerful tool for reduction of multiloop integrals," *J. Phys. Conf. Ser.* **523** (2014) 012059, arXiv:1310.1145 [hep-ph].

[66] R. N. Lee, "Presenting LiteRed: a tool for the Loop InTEgrals REDuction," arXiv:1212.2685 [hep-ph].

[67] V. A. Smirnov, *Analytic tools for Feynman integrals*, vol. 250. 2012.

[68] A. V. Smirnov and A. V. Petukhov, "The Number of Master Integrals is Finite," *Lett. Math. Phys.* **97** (2011) 37–44, arXiv:1004.4199 [hep-th].

[69] T. Hahn, "Generating Feynman diagrams and amplitudes with FeynArts 3," *Comput. Phys. Commun.* **140** (2001) 418–431, arXiv:hep-ph/0012260.

[70] V. Shtabovenko, R. Mertig, and F. Orellana, "New Developments in FeynCalc 9.0," *Comput. Phys. Commun.* **207** (2016) 432–444, arXiv:1601.01167 [hep-ph].

[71] R. Mertig, M. Bohm, and A. Denner, "FEYN CALC: Computer algebraic calculation of Feynman amplitudes," *Comput. Phys. Commun.* **64** (1991) 345–359.

[72] L. D. Landau, "On the angular momentum of a system of two photons," *Dokl. Akad. Nauk SSSR* **60** no. 2, (1948) 207–209.

[73] C.-N. Yang, "Selection Rules for the Dematerialization of a Particle Into Two Photons," *Phys. Rev.* **77** (1950) 242–245.

[74] G. Passarino and M. J. G. Veltman, "One Loop corrections for e^+e^- annihilation into $\mu^+\mu^-$ in the Weinberg Model," *Nucl. Phys.* **B160** (1979) 151.

[75] T. Hahn and M. Perez-Victoria, "Automatized one loop calculations in four-dimensions and D-dimensions," *Comput. Phys. Commun.* **118** (1999) 153–165, arXiv:hep-ph/9807565.

[76] M. Spira, A. Djouadi, D. Graudenz, and P. M. Zerwas, "Higgs boson production at the LHC," *Nucl. Phys. B* **453** (1995) 17–82, arXiv:hep-ph/9504378.

[77] U. Aglietti, R. Bonciani, G. Degrassi, and A. Vicini, "Analytic Results for Virtual QCD Corrections to Higgs Production and Decay," *JHEP* **01** (2007) 021, arXiv:hep-ph/0611266.

[78] R. Bonciani, P. Mastrolia, and E. Remiddi, "Vertex diagrams for the QED form-factors at the two loop level," *Nucl. Phys. B* **661** (2003) 289–343, arXiv:hep-ph/0301170. [Erratum: Nucl.Phys.B 702, 359–363 (2004)].

[79] C. Anastasiou, S. Beerli, S. Bucherer, A. Daleo, and Z. Kunszt, "Two-loop amplitudes and master integrals for the production of a Higgs boson via a massive quark and a scalar-quark loop," *JHEP* **01** (2007) 082, arXiv:hep-ph/0611236.

[80] M. Becchetti and R. Bonciani, "Two-Loop Master Integrals for the Planar QCD Massive Corrections to Di-photon and Di-jet Hadro-production," *JHEP* **01** (2018) 048, arXiv:1712.02537 [hep-ph].

[81] S. Caron-Huot and J. M. Henn, "Iterative structure of finite loop integrals," *JHEP* **06** (2014) 114, arXiv:1404.2922 [hep-th].

[82] A. von Manteuffel and L. Tancredi, "A non-planar two-loop three-point function beyond multiple polylogarithms," *JHEP* **06** (2017) 127, arXiv:1701.05905 [hep-ph].

[83] A. B. Goncharov, "Multiple polylogarithms, cyclotomy and modular complexes," *Math. Res. Lett.* **5** (1998) 497–516, arXiv:1105.2076 [math.AG].

[84] C. Duhr, "Mathematical aspects of scattering amplitudes," in *Theoretical Advanced Study Institute in Elementary Particle Physics: Journeys Through the Precision Frontier: Amplitudes for Colliders*, pp. 419–476. 2015. arXiv:1411.7538 [hep-ph].

[85] L. Naterop, A. Signer, and Y. Ulrich, "handyG —Rapid numerical evaluation of generalised polylogarithms in Fortran," *Comput. Phys. Commun.* **253** (2020) 107165, arXiv:1909.01656 [hep-ph].

[86] R. Bonciani, G. Degrassi, P. P. Giardino, and R. Gröber, "A Numerical Routine for the Crossed Vertex Diagram with a Massive-Particle Loop," *Comput. Phys. Commun.* **241** (2019) 122–131, arXiv:1812.02698 [hep-ph].

[87] L. F. Abbott, "Introduction to the Background Field Method," *Acta Phys. Polon. B* **13** (1982) 33.

[88] T. Kinoshita, "Mass singularities of Feynman amplitudes," *J. Math. Phys.* **3** (1962) 650–677.

[89] T. D. Lee and M. Nauenberg, "Degenerate Systems and Mass Singularities," *Phys. Rev.* **133** (1964) B1549–B1562.

[90] S. Catani and M. H. Seymour, "A General algorithm for calculating jet cross-sections in NLO QCD," *Nucl. Phys. B* **485** (1997) 291–419, arXiv:hep-ph/9605323. [Erratum: Nucl.Phys.B 510, 503–504 (1998)].

[91] D. A. Akyeampong and R. Delbourgo, "Dimensional regularization, abnormal amplitudes and anomalies," *Nuovo Cim. A* **17** (1973) 578–586.

[92] P. Breitenlohner and D. Maison, "Dimensional Renormalization and the Action Principle," *Commun. Math. Phys.* **52** (1977) 11–38.

[93] S. Larin, "The Renormalization of the axial anomaly in dimensional regularization," *Phys. Lett. B* **303** (1993) 113–118, arXiv:hep-ph/9302240.

[94] **ATLAS** Collaboration, M. Aaboud *et al.*, "Measurement of ZZ production in the $\ell\ell\nu\nu$ final state with the ATLAS detector in pp collisions at $\sqrt{s} = 13$ TeV," *JHEP* **10** (2019) 127, arXiv:1905.07163 [hep-ex].

[95] **ATLAS** Collaboration, M. Aaboud *et al.*, "$ZZ \to \ell^+\ell^-\ell'^+\ell'^-$ cross-section measurements and search for anomalous triple gauge couplings in 13 TeV pp collisions with the ATLAS detector," *Phys. Rev. D* **97** no. 3, (2018) 032005, arXiv:1709.07703 [hep-ex].

[96] **CMS** Collaboration, A. M. Sirunyan *et al.*, "Measurements of the pp $\to$ ZZ production cross section and the Z $\to 4\ell$ branching fraction, and constraints on anomalous triple gauge couplings at $\sqrt{s} = 13\,\mathrm{TeV}$," *Eur. Phys. J. C* **78** (2018) 165, arXiv:1709.08601 [hep-ex]. [Erratum: Eur.Phys.J.C 78, 515 (2018)].

[97] R. W. Brown and K. O. Mikaelian, "W^+W^- and Z^0Z^0 pair production in e^+e^-, pp, and $\overline{p}p$ colliding beams," *Phys. Rev. D* **19** (Feb, 1979) 922–934. https://link.aps.org/doi/10.1103/PhysRevD.19.922.

[98] J. Ohnemus and J. F. Owens, "Order-α_s calculation of hadronic zz production," *Phys. Rev. D* **43** (Jun, 1991) 3626–3639. https://link.aps.org/doi/10.1103/PhysRevD.43.3626.

[99] B. Mele, P. Nason, and G. Ridolfi, "Qcd radiative corrections to z boson pair production in hadronic collisions," *Nuclear Physics B* **357** no. 2, (1991) 409–438. https://www.sciencedirect.com/science/article/pii/055032139190475D.

[100] F. Cascioli, T. Gehrmann, M. Grazzini, S. Kallweit, P. Maierhöfer, A. von Manteuffel, S. Pozzorini, D. Rathlev, L. Tancredi, and E. Weihs, "ZZ production at hadron colliders in NNLO QCD," *Phys. Lett. B* **735** (2014) 311–313, arXiv:1405.2219 [hep-ph].

[101] T. Gehrmann, A. von Manteuffel, L. Tancredi, and E. Weihs, "The two-loop master integrals for $q\bar{q} \to VV$," *JHEP* **06** (2014) 032, arXiv:1404.4853 [hep-ph].

[102] F. Caola, J. M. Henn, K. Melnikov, A. V. Smirnov, and V. A. Smirnov, "Two-loop helicity amplitudes for the production of two off-shell electroweak bosons in quark-antiquark collisions," *JHEP* **11** (2014) 041, arXiv:1408.6409 [hep-ph].

[103] T. Gehrmann, A. von Manteuffel, and L. Tancredi, "The two-loop helicity amplitudes for $q\bar{q}' \to V_1V_2 \to 4$ leptons," *JHEP* **09** (2015) 128, arXiv:1503.04812 [hep-ph].

[104] E. Accomando, A. Denner, and A. Kaiser, "Logarithmic electroweak corrections to gauge-boson pair production at the LHC," *Nucl. Phys. B* **706** (2005) 325–371, arXiv:hep-ph/0409247.

[105] A. Bierweiler, T. Kasprzik, and J. H. Kühn, "Vector-boson pair production at the LHC to $\mathcal{O}(\alpha^3)$ accuracy," *JHEP* **12** (2013) 071, arXiv:1305.5402 [hep-ph].

[106] J. Baglio, L. D. Ninh, and M. M. Weber, "Massive gauge boson pair production at the LHC: a next-to-leading order story," *Phys. Rev. D* **88** (2013) 113005, arXiv:1307.4331 [hep-ph]. [Erratum: Phys.Rev.D 94, 099902 (2016)].

[107] M. Grazzini, S. Kallweit, M. Wiesemann, and J. Y. Yook, "ZZ production at the LHC: NLO QCD corrections to the loop-induced gluon fusion channel," *JHEP* **03** (2019) 070, arXiv:1811.09593 [hep-ph].

[108] D. A. Dicus, C. Kao, and W. W. Repko, "Gluon production of gauge bosons," *Phys. Rev. D* **36** (Sep, 1987) 1570–1572. https://link.aps.org/doi/10.1103/PhysRevD.36.1570.

[109] E. Glover and J. Van der Bij, "Z-boson pair production via gluon fusion," *Nuclear Physics B* **321** no. 3, (1989) 561–590. https://www.sciencedirect.com/science/article/pii/0550321389902629.

[110] **ATLAS** Collaboration, M. Aaboud *et al.*, "Constraints on off-shell Higgs boson production and the Higgs boson total width in $ZZ \to 4\ell$ and $ZZ \to 2\ell 2\nu$ final states with the ATLAS detector," *Phys. Lett. B* **786** (2018) 223–244, arXiv:1808.01191 [hep-ex].

[111] **CMS** Collaboration, A. M. Sirunyan *et al.*, "Measurements of the Higgs boson width and anomalous HVV couplings from on-shell and off-shell production in the four-lepton final state," *Phys. Rev. D* **99** no. 11, (2019) 112003, arXiv:1901.00174 [hep-ex].

[112] F. Caola and K. Melnikov, "Constraining the Higgs boson width with ZZ production at the LHC," *Phys. Rev. D* **88** (2013) 054024, arXiv:1307.4935 [hep-ph].

[113] J. M. Campbell, R. K. Ellis, and C. Williams, "Bounding the Higgs Width at the LHC Using Full Analytic Results for $gg- > e^- e^+ \mu^- \mu^+$," *JHEP* **04** (2014) 060, arXiv:1311.3589 [hep-ph].

[114] N. Kauer and G. Passarino, "Inadequacy of zero-width approximation for a light Higgs boson signal," *JHEP* **08** (2012) 116, arXiv:1206.4803 [hep-ph].

[115] R. Harlander and P. Kant, "Higgs production and decay: Analytic results at next-to-leading order QCD," *JHEP* **12** (2005) 015, arXiv:hep-ph/0509189.

[116] A. von Manteuffel and L. Tancredi, "The two-loop helicity amplitudes for $gg \to V_1 V_2 \to 4$ leptons," *JHEP* **06** (2015) 197, arXiv:1503.08835 [hep-ph].

[117] F. Caola, K. Melnikov, R. Röntsch, and L. Tancredi, "QCD corrections to ZZ production in gluon fusion at the LHC," *Phys. Rev. D* **92** no. 9, (2015) 094028, arXiv:1509.06734 [hep-ph].

[118] F. Caola, M. Dowling, K. Melnikov, R. Röntsch, and L. Tancredi, "QCD corrections to vector boson pair production in gluon fusion including interference effects with off-shell Higgs at the LHC," *JHEP* **07** (2016) 087, arXiv:1605.04610 [hep-ph].

[119] R. Gröber, A. Maier, and T. Rauh, "Top quark mass effects in $gg \to ZZ$ at two loops and off-shell Higgs boson interference," *Phys. Rev. D* **100** no. 11, (2019) 114013, arXiv:1908.04061 [hep-ph].

[120] B. Agarwal, S. P. Jones, and A. von Manteuffel, "Two-loop helicity amplitudes for $gg \to ZZ$ with full top-quark mass effects," *JHEP* **05** (2021) 256, arXiv:2011.15113 [hep-ph].

[121] C. Brønnum-Hansen and C.-Y. Wang, "Top quark contribution to two-loop helicity amplitudes for Z boson pair production in gluon fusion," *JHEP* **05** (2021) 244, arXiv:2101.12095 [hep-ph].

[122] F. Caola, J. M. Henn, K. Melnikov, A. V. Smirnov, and V. A. Smirnov, "Two-loop helicity amplitudes for the production of two off-shell electroweak bosons in gluon fusion," *JHEP* **06** (2015) 129, arXiv:1503.08759 [hep-ph].

[123] J. Davies, G. Mishima, M. Steinhauser, and D. Wellmann, "Double Higgs boson production at NLO in the high-energy limit: complete analytic results," *JHEP* **01** (2019) 176, arXiv:1811.05489 [hep-ph].

[124] https://www.ttp.kit.edu/preprints/2020/ttp20-041/.

[125] A. V. Smirnov and F. S. Chuharev, "FIRE6: Feynman Integral REduction with Modular Arithmetic," *Comput. Phys. Commun.* **247** (2020) 106877, arXiv:1901.07808 [hep-ph].

[126] G. A. Baker and P. Graves-Morris, *Padé Approximants*. Cambridge University Press, 1996.

[127] K. Melnikov and T. v. Ritbergen, "The Three loop relation between the MS-bar and the pole quark masses," *Phys. Lett. B* **482** (2000) 99–108, arXiv:hep-ph/9912391.